Experimental and Numerical Investigation of Part Fabrication by Incremental Sheet Forming

by

Ankush Bansal

A dissertation submitted in partial fulfillment
of the requirements for the degree of
Doctor of Philosophy
(Mechanical Engineering)
in the University of Michigan
2021

Doctoral Committee:

Professor Jun Ni, Co-Chair
Professor Alan Taub, Co-Chair
Assistant Professor Daniel Cooper
Professor Pingsha Dong

Ankush A. Bansal

ankb@umich.edu

ORCID iD: 0000-0002-5605-8944

Acknowledgements

After an intense period of five years, today is the day I get an opportunity to write a note of acknowledgement as a finishing touch on my thesis. It has been a journey of learning and hard work, not just academically, but also on a personal level. At the end of my doctorate, I can't imagine reaching my goals without the constant help and support from everyone around me.

Foremost, it is with deep gratitude that I acknowledge the perpetual support from both my advisors, Prof. Jun Ni and Prof. Alan Taub, throughout my stay at University of Michigan. Prof. Ni provided me with an opportunity to pursue a career in the doctorate program when I was still a masters student back in India. Prof. Taub never gave up on me even when I was occasionally lost and always made himself available for advice despite a busy schedule. Not only are they an excellent mentor for upcoming researchers, but also a great force to do something good for the society. They definitely provided me with the tools that I needed to achieve a doctorate and be successful in my career.

I would also like to express appreciation to my dissertation committee members, Prof. Pingsha Dong and Prof. Daniel Cooper, for spending their valuable time on reading my work and providing constructive feedback. Their expert opinions helped me understand the fine technical details and improve the writeup quality.

Research work presented here was partially funded by DOD-ONR N00014-14-20002-LIFT 0007A-4 through the American Lightweight Materials Manufacturing Innovation Institute

(LIFT). Our collaborators at LIFT, John Keogh and Alessandro Posteraro, consistently helped me explore innovative ideas and test them in industrial settings. Dr. Ravi Verma from Boeing brought a unique perspective from industry side that helped me make breakthroughs in my research.

During my time at University of Michigan, I got a chance to work alongside the best and brightest researchers, the fellow PhD scholars, who I get to call close friends of mine. A big thank you to Baoyang Jiang, Xingjian Lai, Yossi Cohen, Zhiyi Chen and Tianxing Ma. Our weekly pursuit of Indian food made me feel like home – away from home. I cannot forget the long technical/non-technical conversations I had with my teammates from incremental forming project – Randy Cheng, Jaekwang Shin and Maya Nath. They provided with me with meaningful feedback, something brutal but honest, about all my ideas and results. My research wouldn't be as good as it is without their inputs.

I thank my friends I made in Ann Arbor – Aman, Arun, Subarno, Aadiya, Mani, Jana and Vivek for their constant motivation and emotional support through this entire journey. In fact, I am indebted to all of them for making my stay here a joyful experience that I will always remember with great fondness.

Finally, I must express my deepest gratitude to my parents, Mr. Anjanikumar Bansal and Mrs. Sushila Bansal, for their unfailing support and encouragement throughout my studies. I am grateful for their tireless work that brought me here and proud to be their son. My accomplishments would not have been possible without them.

Table of Contents

List of Tables

List of Figures

Abstract

In recent years, the demand for personalized products have significantly increased in biomedical, automotive and aerospace industries. However, traditional sheet metal forming processes such as stamping, deep drawing and hydroforming are only suitable for high-volume production due to high initial setup costs and long production lead time. In this research, a relatively new fabrication technique named incremental sheet forming (ISF) process is comprehensively investigated to address the emerging need for customized parts. Major advantages of ISF process are lower forming forces, increased material formability and energy efficiency compared to traditional forming processes. However, it produces complex and non-linear strain history that makes it difficult to control sheet springback and produce parts with industry standard geometric accuracy.

There are multiple variants of ISF process such as single-point incremental forming (SPIF), two-point incremental forming (TPIF) and double-sided incremental forming (DSIF). In SPIF, forming tool induces deformation on the top surface of a flat sheet without any support from the bottom side. In TPIF, a partial or a half-die is present underneath the flat sheet to provide support and reduce any unwanted deformations. DSIF is a relatively new variant that contains two independently controlled tool – one on each side of the sheet. It requires a custom-built CNC machine with two independent milling heads.

In this thesis, incremental micro-forming (μSPIF) process is investigated to improve part accuracy and understand deformation mechanics for its applications in biomedical and micro-

electronics industries. An experimental setup is developed in-house that mimics a table-top CNC machine and provides synchronous tool motion in x, y and z directions. Truncated cones and pyramids are experimentally produced on 50 μm thin AL 1100 and AL 5052 foils to quantify the process performance. The parametric analysis showed significant influence of step size and tool diameter on both forming forces and material formability. When the cross-sectional profiles of produced parts are compared with its designed geometry, it showed a deviation of 80-120 μm that could be attributed to the combination of machine compliance and sheet springback.

The capabilities of macro-TPIF process are also explored to investigate and improve its process performance in the production of aerospace parts. Besides inferior geometric accuracy, the correct estimation of material squeeze factor is identified as a major research gap in TPIF process. Previous studies have reported material squeeze values of anywhere between 10% to 50% in TPIF/DSIF experiments. However, effective material squeeze obtained in the experiments can be considerably different than its programmed value due to tool deflection and machine compliance. Therefore, a mathematic model is proposed and experimentally validated to calculate an effective squeeze factor based on its programmed value, forming forces and pre-recorded machine compliance. For cone 67° part, programmed squeeze factor of 40% results in only 2.3% of effective squeeze in experiments. This effect must be appropriately considered while developing a FE model to obtain accurate results. Further analysis of squeeze factor on heart shape parts showed that increase in material squeeze helped improve geometric accuracy but also accumulated an unwanted bulge at the part bottom. Therefore, a new multi-stage toolpath strategy is proposed that flattens any asperities and redistributes the surface material resulting in better geometry accuracy compared to the hydro-formed part.

Finally, it is important to develop a cost-efficient and accurate prediction model to understand the underlying process mechanics and avoid part failure. A finite element model for μISF is developed that can provide predictive results with good accuracy in minimum computation time. Tensile tests are performed on AL 1100 material to obtain constitutive models that are required as input for FE simulations. Holloman's strain hardening law with isotropic hardening provided the best prediction results when benchmarked against experimental data. The techniques of mass and velocity scaling are successfully utilized to artificially accelerate the simulation speed without compromising on prediction results. Forming forces for both cone 45° and cone 60° are predicted with less than 10% error. It is also demonstrated that using numerical techniques such as Rayleigh mass damping and hourglass control can lead to massive numerical artifacts. So, they must be utilized with utmost care.

Chapter 1
Introduction

1.1 Background and Motivation

The fabrication of sheet metal products plays a crucial role in today's manufacturing industries for making machinery, transportation vehicles and daily use products such as electronic devices and home appliances. In automotive and aerospace industries, it is also critical to make lightweight components and achieve high fuel efficiency standards and reduced cost of operation. Therefore, the use of aluminum alloys as a substitute for steel has been widely accepted in the current manufacturing community. Once parts are designed in the automotive industry, most of them use a large-scale production approach using conventional processes such as stamping, deep – drawing and hydroforming, which are best suited for high volume production and achieving acceptable cost – efficiency. However, these processes tend to have high lead time and initial setup cost making them unsuitable for low volume production required in aerospace or perhaps rapid prototyping industry.

A global trend towards compact and integrated systems is rapidly accelerating, therefore efforts must be directed towards the development of miniaturization technology to match up this trend in manufacturing. Conventional fabrication processes such as stamping and deep drawing are well established for macroscale part production as mentioned above. Despite that, numerous challenges remain, such as reduced formability, reduced tool life and process instabilities, when these processes are scaled down to make microscale parts.

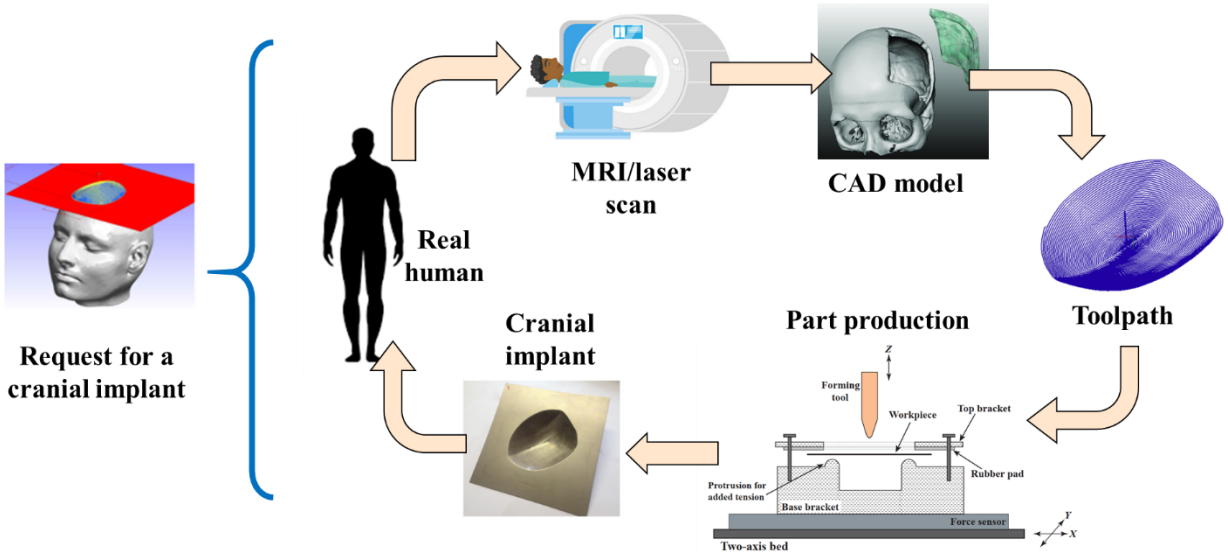

Figure 1.1: Process flow of the part fabrication by incremental forming process from part request to MRI/laser scanning on human skull, to toolpath generation, to finally part production (Ambrogio et al. [3])

In the medical industry, many implants such as dental, cranial and ankle support are required frequently with the shape and size personalized to the individual patient. Cranioplasty is a surgical procedure to repair defects or deformities of a skull. The implant may be categorized based on the type of flaps used: autografting (implant from patient), allografting (implant from a donor body), and alloplastic (non-biologic implant). The selection of its materials is based on both objective requirements, such as biocompatibility and physical properties, and the subjective decisions from surgeon's experience and preferences. Alloplastic cranioplasty has become attractive with the advancement in technical readiness for clinal applications, that brings benefits of short lead time, lost cost, and good customizability. Metals have good structural strength and customizability, and thus are often a better choice for larger implants. It has been reported that a wide range of metals have been used for cranial implants, including aluminum, platinum, titanium, tantalum, gold, and silver. Titanium is the most frequently used metal that features no inflammatory reaction and low infection rate. Carr et al. [1] and Schebesch et al. [2] developed a system for milling any prosthetics from titanium alloys and that continue to be the most used

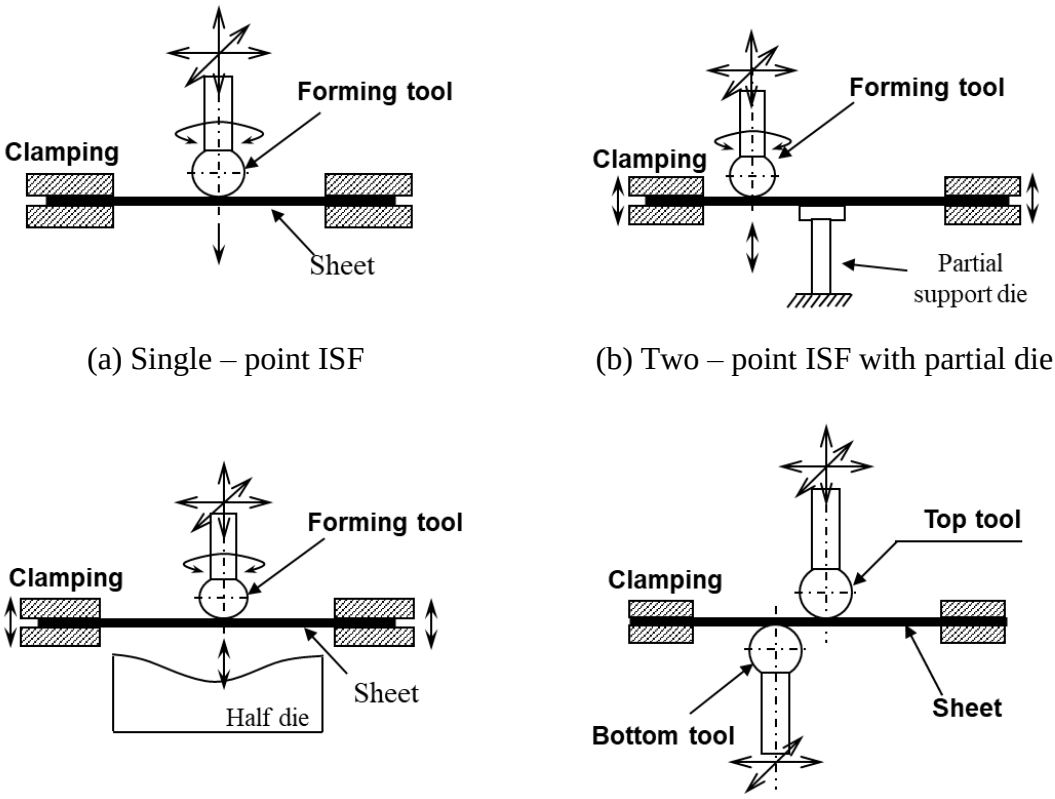

(a) Single – point ISF

(b) Two – point ISF with partial die

(c) Two – point ISF with half die

(d) Double – sided ISF

Figure 1.2: Schematic of incremental sheet metal forming process (Cao et al. [4], Reddy et al. [5])

practice today that results in lot of material removal. However, upon request for an implant, the process flow to produce a personalized part using ISF process is ideally expected to appear as illustrated in **Figure 1.1** [3].

In the electronics industry, micro-electro-mechanical systems (MEMS) technology has advanced significantly in microscale manufacturing and proved its potential in last few decades. However, it is mainly focused on sensor and electronics systems restricted to silicon-based materials. Its application in making metal-based structural components is still challenging.

It could be argued that recent advancements in 3D printing through laser deposition and selective laser sintering are also a viable alternative for rapid prototyping and manufacturing of metallic products. That being said, it would require a lot of support material and structure to print

a thin sheet metal part. The achievable precision for producing micro sheet metal parts using 3D printing methods is also of concerns. This can increase the production time and cost making it unsuitable for sheet metal products.

1.2 Introduction to ISF Process

Incremental sheet forming (ISF) is a relatively new die-less manufacturing technology that can produce complex 3D shapes on a metal sheet without using any part specific tooling. It has gained much attention in last decade due to its ability to provide a cost-efficient alternative for mass customized production compared to traditional processes such as stamping, hydroforming and deep drawing. In this process, a stylus type tool moves in a pre-defined toolpath over a metal sheet introducing a collection of tiny deformations. No part specific tooling is required to form any complex 3D shape on a thin metal sheet. It offers cost savings for small volume production often required in aerospace industry and prototyping for automobile and prosthetics industries. Higher material formability, along with reduced forming forces, and high process flexibility compared to traditional processes are some of the major advantages of the ISF process.

There are multiple configurations of ISF process introduced over the same time in an effort to address some shortcomings of process capabilities and part accuracy, including (a) Single-point ISF (SPIF), (b) Two-point ISF (TPIF) and (c) Double-sided ISF (DSIF) as schematically shown in **Figure 1.2** ([4],[5]). It has demonstrated significant potential for economically fabricating sheet metal parts required in low volume. Incremental sheet micro-forming (μISF) process possesses the potential to cost effectively manufacture miniaturized structural parts and fulfills the need for part personalization in a wide range of industries from medical field to small scale power generation.

In SPIF, a flat metal sheet is clamped in a CNC machine using a set of top and bottom frames. A hemispherical-ended tool moves in a predefined toolpath over the sheet surface making tiny indentation without any support from the bottom of the sheet as shown in **Figure 1.2**(a). It provides high process flexibility to change part design and fabricate the part without much of a lead time. However, the part accuracy obtained through this variant is inferior to the other ones

due to absence of any bottom support. Also, some complex geometries involving upside down or convex type features cannot be formed using SPIF.

TPIF is another variant of ISF process with a partial or a half – die present underneath the sheet for local support as shown in **Figure 1.2**(b) and (c). This enables the fabrication of intricate features on a designed part geometry with good accuracy. The presence of a support die helps significantly reduce any unwanted bending or deformations on the sheet. Once the process is established, toolpath and parametric optimization could prove it to be an ideal alternative for hydro-forming process. However, it also makes the process less flexible due to added part specific die support making it more appropriate for only low volume production rather than prototyping and personalized production.

DSIF is the newest variant of the ISF process that involves two independently controlled tools (sometimes also referred as “master” and “slave” tools [6]) on both top and bottom side of the sheet as shown in **Figure 1.2**(d) . It provides the most process flexibility when compared to the other two variants as it does not require any part specific tooling and can still fabricate parts with intricately designed features. At any moment in DSIF, one tool acts as a forming tool that induces the indentation and the other one acts as a dynamic local support. One of the major drawbacks of this process is that it requires a custom-made machine with two independently controlled 3-axis CNC heads.

Consequently, only SPIF and TPIF processes are extensively studied in this thesis for both micro and macro-scale part production. The required experimental setups are developed in-house as per the details present in forthcoming experimental analysis chapters. And though not comprehensively, DSIF process is also briefly studied to develop process optimizations through a collaboration with Prof. Jian Cao’s research group at Northwestern University.

1.3 Research Objectives

There are many challenges involved in the analysis of sheet metal deformation that are essential to the ISF process. First, a significant difference between micro and macro scale forming is the size effect, where material properties are no longer scalable to its size as it reaches a smaller dimension. Characterizing the size effect in incremental sheet forming process can help build comprehensive understanding of the mechanics behind it. Second, the geometric accuracy in incremental forming cannot reach a desirable level due to the large spring back effect. Also, due to the complex deformation nature of this process, it is important to develop a numerical finite element-based prediction model for incremental sheet forming to understand the aforementioned mechanics and sheet springback effects. Based on these challenges, the fundamental aim of the presented research is divided into two classes:

- Understanding the deformation mechanics of ISF process:
    1. To improve the process performance, it is important to know the underlying deformation mechanics by developing an accurate and cost-efficient numerical prediction model.
    2. By developing the prediction model, complex 3D shapes can be accurately fabricated on a thin metal sheet and part failure can be prevented prior to fabrication.
- Improvement of the process performance:
    1. The quantification of process performance based on part accuracy, formability and surface finish is required for the process application in current manufacturing industries.
    2. Geometric accuracy through ISF is inferior to that of stamping or hydro-forming processes. Therefore, a corrective toolpath generation strategy based on error compensations and optimization is needed to produce the parts with acceptable accuracy.

1.4 Thesis Outline

This dissertation contains three main chapters, #2 to #4. The outline of each of these chapters are as follow:

- Chapter 2: Experimental investigation of micro/meso-scale part fabrication using single – point incremental micro-forming process

  The primary goal of this chapter is to develop an experimental setup to fabricate micro/meso-scale parts of thin metal foils using incremental micro-forming process. Additionally, major objective from this part of the work is to characterize the miniature material behavior in the incremental sheet micro-forming process in terms of part accuracy and formability and to enable die-less forming of defect-free and cost-effective sub-millimeter sized sheet metal components. Thus far, limited studies are available in literature that quantifies its process performance in these terms. Also, there hasn't been a robust data set available on which set of process parameters yield the most optimum part forming conditions.

- Chapter 3: Rapid prototyping and manufacturing of aerospace parts using two-point incremental forming process

  In this chapter, an experimental setup for the fabrication of macro-scale parts for automotive and aerospace industries through two – point incremental forming process is developed. After some process benchmarking with axisymmetric truncated cone geometries, process performance in a complex heart shaped part is investigated. It is seen that, toolpath optimization for material squeeze factor significantly influences its geometric accuracy. In addition, material squeeze factor programmed in the predesigned toolpath deviates significantly from effective material squeeze obtained during the experiments. Therefore, a mathematical framework is proposed and validated to estimate the effective material squeeze

during experiments based on machine compliance, forming tool deflection and reactionary forces on the tool.

Generally, all the parts in TPIF are produced in one single stage. But in this chapter, a multi-stage TPIF forming strategy is proposed to improve geometric accuracy and even, in some cases, better than hydroformed part. A test case of an aerospace fuel cover part is successfully fabricated and tested to demonstrate the capabilities and the robustness provided by this process.

- Chapter 4: Constitutive material model and high – fidelity finite element analysis of incremental micro-forming process

The main objective of this chapter is to develop a finite element – based numerical prediction model to represent μISF process so that the unknown complex stress states, material movement, excessive thinning and part failure can be successfully predicted for any given part geometry. With its clear understanding, process performance quantifiers such as geometric accuracy and mechanical strength can be significantly improved in conjunction with failure prevention. Firstly, material testing is performed to understand AL 1100 material behavior under uniaxial loading condition and a constitutive material model is proposed that would be best suited for this particular process.

Secondly, the developed model is benchmarked using a truncated cone 45° geometry and validated against experimental results obtained in Chapter 2 to achieve prediction results with acceptable accuracy and least computation cost. The same FE model is also tested and validated on a high wall angled cone 60° part to show the model robustness. Concepts of artificial acceleration via mass/velocity scaling, element hourglass control and Rayleigh mass damping techniques are utilized to meet the aforementioned goals.

Chapter 2
Experimental Investigation of Micro/Meso-scale Part Fabrication Using Single – Point Incremental Micro-Forming Process

2.1 Introduction

Micro-incremental sheet forming (μISF) is a die-less micro-forming process that demonstrates significant potential for economically fabricating sheet metal parts required in low-volume. Conventionally, micro-scale sheet metal parts are produced using various forming processes such as rigid stamping, soft stamping, hydroforming and micro-rolling [7]. These operations require component specific tooling, and the design and fabrication of such tooling increases the lead time and becomes expensive for low volume production. However, μISF provides an alternative for cost-efficient and low-volume production of thin sheet metal products ([8], [9]). This forming technology, in macro-scale, proved to have localized deformation which helps to avoid sheet necking that normally occurs in conventional forming processes and therefore proved to exhibit higher formability [10].

The primary goal of the research in this chapter was to develop an experimental setup and conduct experimental study of fabricating micro/meso-scale parts of thin metal foils using an incremental micro-forming process. Additionally, a major objective from this part of work is to characterize the material behavior in the incremental sheet micro-forming process in terms of part accuracy and formability and enable die-less forming of defect-free and cost-effective sub-millimeter sized sheet metal components. Thus far, few studies are reported in the literature that

quantify the process performance in these terms. Also, there has not been a robust data set available on which set of process parameters yield the most optimum part forming conditions.

2.2 Literature Review

Incremental sheet metal forming was first invented by Edward Leszak in 1964 [11]. He used a lathe machine to demonstrate the advantages of this process by forming axisymmetric shapes without the use of any special die or mandrel. As this process gained more importance in automotive, aerospace and biomedical industries, researchers around the world started improving its performance by making complex 3D shapes [12], enhancing part accuracy [13] and material formability [14]. Formability in ISF process is better than that of conventional stamping processes but attaining good dimensional accuracy has always been a conundrum for researchers.

Incremental forming of miniaturized three-dimensional shell structures was first proposed by Saotome and Okamoto in 2001 [15]. Using an in-house developed system, authors formed a 600 µm long car shaped part as shown in **Figure 2.1** by the process of continuous hammering. A tool head of 10 µm diameter was used to repeatedly hammer a 10 µm thick aluminum foil in small increments to plastically deform it. However, it was very difficult to control the amplitude of tool

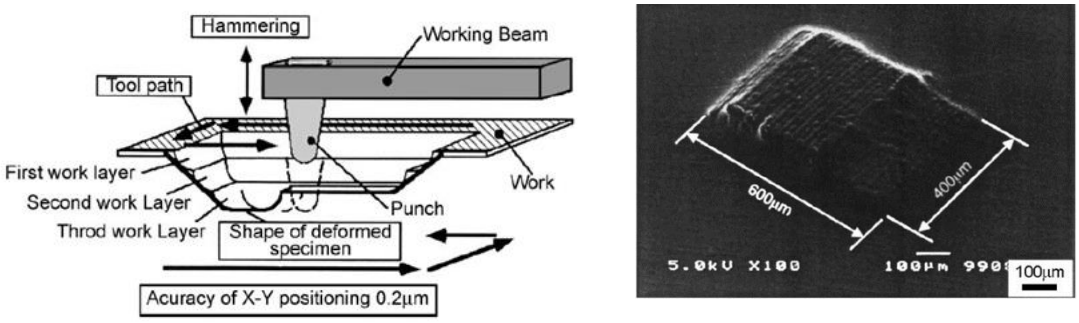

(a) (b)

Figure 2.1: Schematic of die-less micro-forming by hammering and (b) SEM micrograph of a formed car shaped part (Saotome et al. [15])

vibration and its motion. Therefore, they had to use a single crystal silicon die manufactured through the silicon chip process.

To overcome this issue, Obikawa et al. [8] developed a table-top incremental forming machine as shown in **Figure 2.2**(a), which did not require any die and any backing plate to form the desired geometry. They formed nine pyramids with a carbide tool at arbitrary locations as shown in **Figure 2.2**(b). Process parameters used to form these parts were: step size Δz = 12 µm, half apex angle θ = 31.5º, feed rate f = 0.1 - 1.0 mm/s and spindle speed ω = 10,000 – 20,000 rpm. Authors also studied the effect of tool rotational speed and step size on material formability using two different materials AL – 1 and AL – 2. It was observed that forming limit did not show a visible correlation with tool rotation for both the materials as displayed in **Figure 2.3**(a) and (b). However, the increase in step size after a threshold value led to the decrease in forming limit of both AL – 1 and AL – 2 materials as compared in **Figure 2.3**(c) and (d) respectively. Highest material formability is obtained approximately at the step size to sheet thickness ratio of 1. Therefore, this is labeled as the optimum parametric value with the constraint of achieved maximum material formability. It can be assumed from this result that the similar optimization of

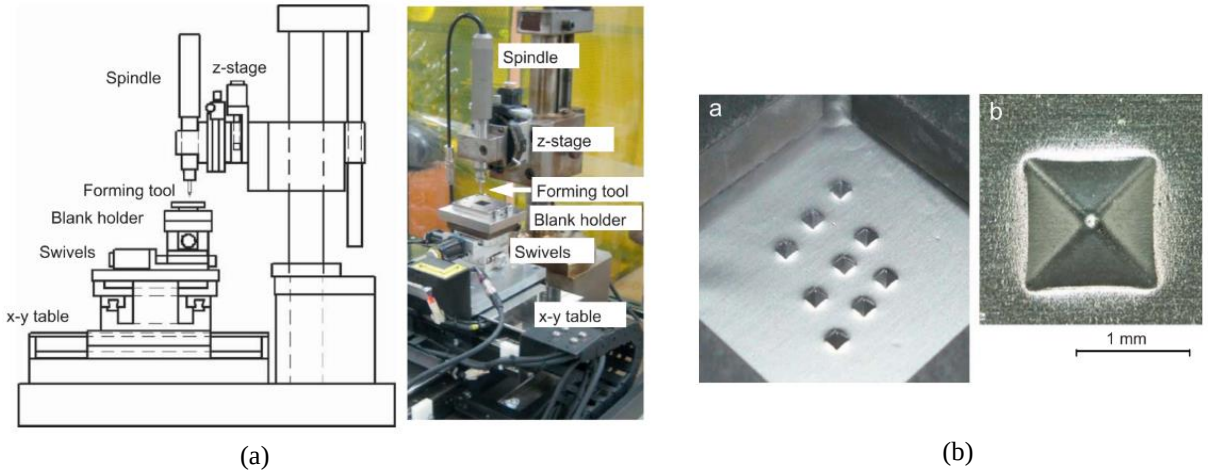

(a) (b)

Figure 2.2: (a) A desktop type of milling machine used for incremental forming and (b) Nine miniature pyramids formed at arbitrary positions on an AL – 2 blank and a CCD micrograph of the top view of a pyramid with θ = 31.5º (Obikawa et al. [8])

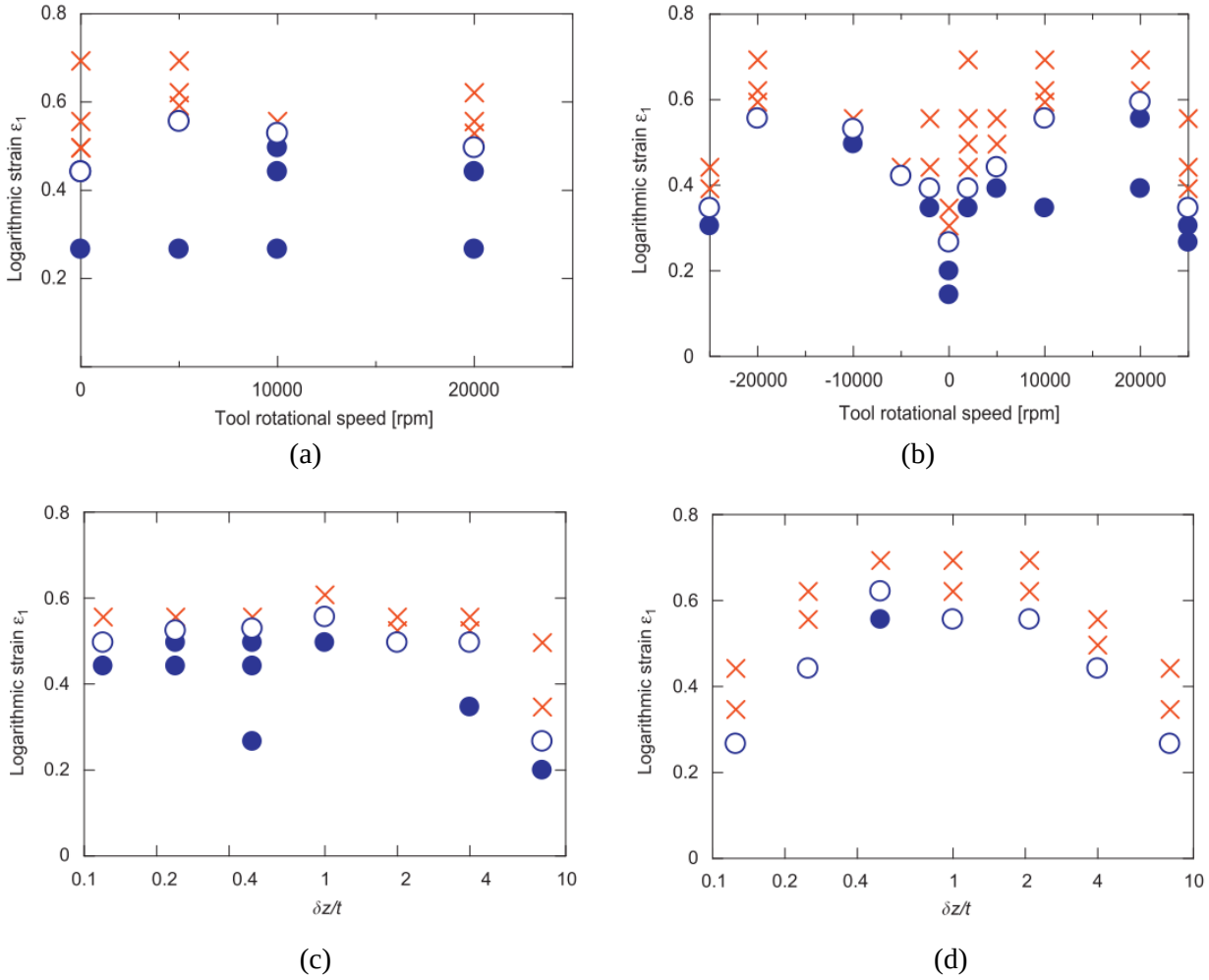

Figure 2.3:Change in forming limit with tool rotational speed for (a) AL-1 foil and (b) AL-2 foil. Change in forming limit with stepwise axial feed for (c) AL-1 foil and (d) AL-2 foil (Obikawa et al. [8])

other process parameters such as tool diameter, tool rotation speed and feed rate is needed to attain maximum part formability.

After the parametric optimization for making pyramids with a 1 mm square base, Obiwaka et al. [9] investigated this process to form pyramids, letters and numbers of 100 µm to 500 µm dimensions as free form products. Pyramids of length 50 µm and 100 µm were formed using optimized process parameters and half apex angle of 45º as shown in **Figure 2.4**(a) and (b). Also, letters "T" and "U" of 100 µm dimensions were formed using same tool tip radius of 10 µm as shown in **Figure 2.4**(c) and (d), respectively. From these results, it can be concluded that

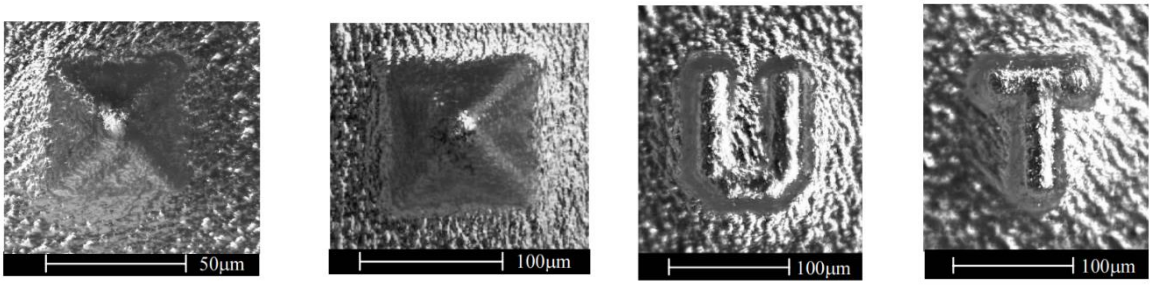

(a) (b) (c) (d)

Figure 2.4: (a) Pyramid of length 50 μm, (b) Pyramid of length 100 μm, (c) Letter "T" of size 150 μm, (d) Letter "U" of size 150 μm (Obikawa et al. [9])

incremental micro-forming is capable of manufacturing miniaturized products of the order of 100 μm in size. Although, it should be noted that the geometric accuracy of the part was said to be significantly decreased with decreasing product size and the surface roughness became noticeable. Grain size has significant influence on both part accuracy and surface finish as the grain size for raw material used in this process was in the range of 5 – 10 μm, which was only one-fifth or one-tenth of the final part size and same as initial sheet thickness. Hence, constraint to the deformation in thickness direction was very weak and therefore promoted heterogeneous deformation depending on the crystal anisotropy.

To enhance geometric accuracy and surface quality of parts, Obikawa et al. [16] implemented an ultrasonic spindle with axial vibration and formed microshell structures of aluminum, stainless steel and titanium foils. The effect of ultrasonic vibration assistance on part accuracy was investigated by forming a twisted pyramidal shape with aluminum foil. It can be observed from the figures that part accuracy can be significantly enhanced by using ultrasonic vibrations. A truncated micro-pyramid of D = 283 μm formed with ultrasonic vibration is shown in **Figure 2.5**. Although the tool rotational speed, table speed and axial feed were used at optimized values, its shape accuracy was not good, and partially distorted. It was observed that the radius of lateral edges was much larger than that of the forming tool and the feed marks of the tool on the

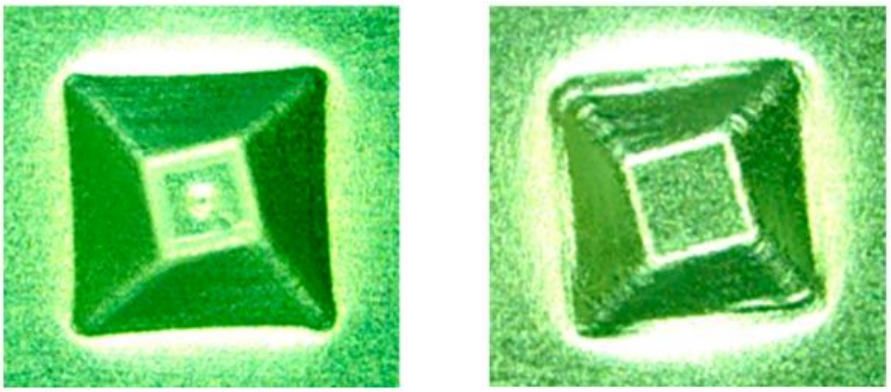

(a) (b)

Figure 2.5: Top view of twisted pyramids formed: (a) using ultrasonic vibration and (b) without ultrasonic vibration (Obikawa et al. [16])

back surface of the pyramid were disturbed. Overall, the part accuracy and geometry were not formed up to required standards.

2.3 Experimental Setup

Experimental setup required for µISF works on similar principles as conventional ISF: a stylus type tool navigates on the surface of a metal sheet and forms any 3D geometry in series of small incremental deformations. However, the µISF setup is not simply a scaled-down version of conventional ISF. Some major concerns, which are unique to micro-scale forming, need to be resolved to achieve effective µISF processes.

First, the blank holder needs to be redesigned. A classic holder assembly typically consists of two brackets, where the sheet metal workpiece is placed between these brackets and clamped by bolts on its periphery. The classic design does not apply additional tension and therefore makes it difficult for workpieces to recover from unwanted distortions. Bending is generally not an issue for thick macro-scale blanks because of their higher bending stiffness. Thinner metal foils, however, are vulnerable to bending under their own weight. Even if these thin metal foils are originally flat, the installation process will inevitably cause distortion. A distorted workpiece not

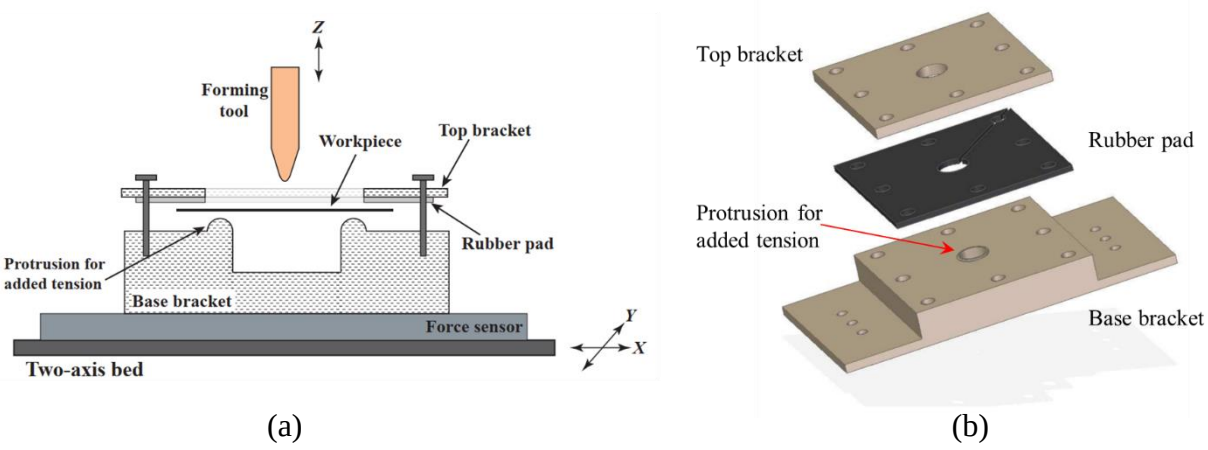

Figure 2.6: (a) Schematic of the experimental setup designed for incremental micro-forming process including forming tool, specimen fixture and force sensor (b) detailed design of the specimen fixture

only affects the geometric accuracy by superposing a non-flat datum, but also creates a loose contact between the tool and the metal surface that prevents effective local deformation, and eventually forms a "buckled" geometry as previously reported by Beltran et al. [17].

Second, it requires precise motion control. The depth increment can be as small as 10 µm, and such increment has to be uniformly distributed through a full cycle of planar motion. If the motion resolution is not high enough, the tool trajectory can contain stepwise increments in depth rather than a smooth depth evolution, resulting in inconsistency in forming. In fact, it is empirically found that non-smooth trajectory results in higher friction and twists the formed part in the direction of tool motion [18].

Besides, tool deflection is much more noticeable with thinner tools. The tool stiffness diminishes drastically - the bending stiffness is proportional to the fourth power of its diameter. Micro forming usually requires long-reach tools to form deeper parts. Tapered tools have higher overall stiffness, but the thinned section is still flexible. As an example, a 10 mm long steel tool with 1 mm stem diameter can have approximately 34 µm deflection under 1 N lateral load – and the actual tool can be much smaller than 1 mm.

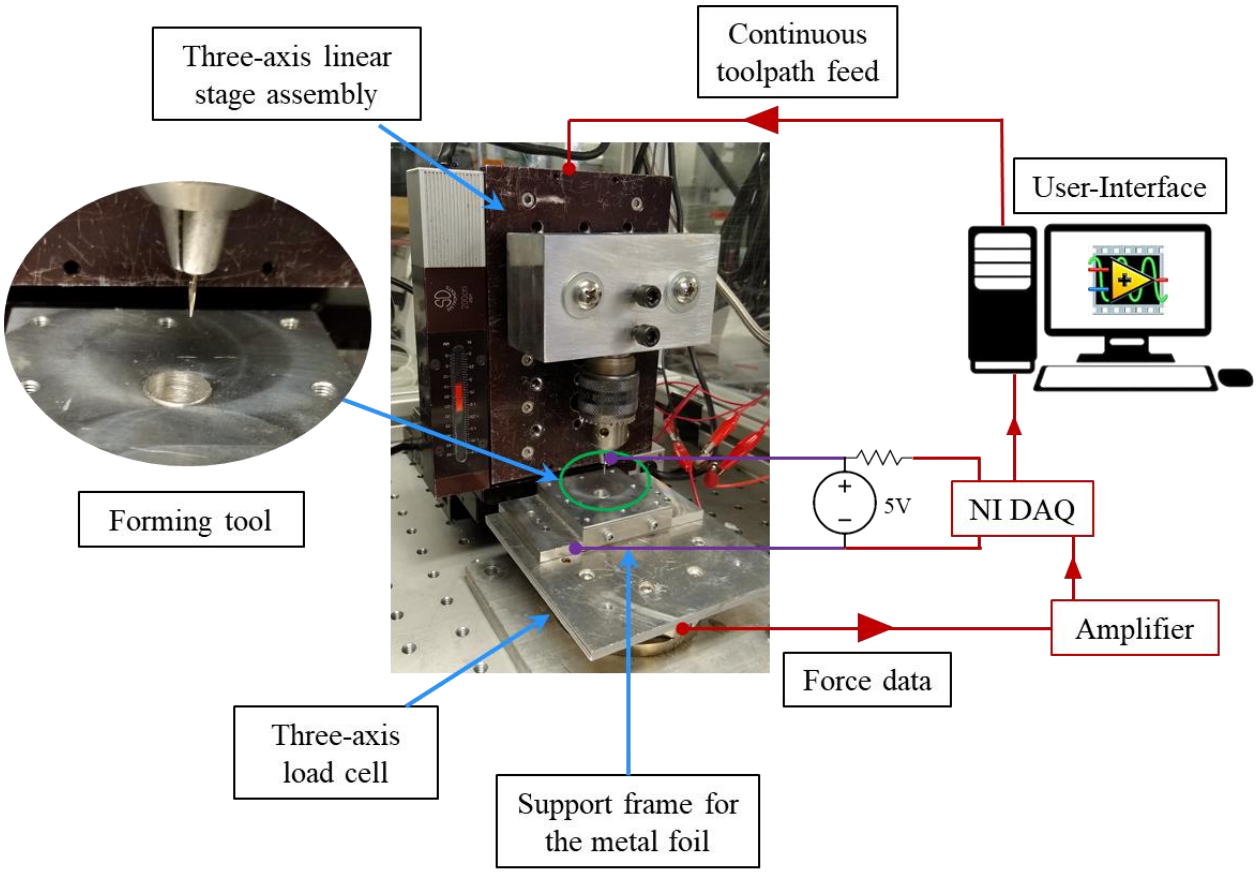

Figure 2.7: Experimental setup developed at Wu Manufacturing Research Center, University of Michigan for analysis of incremental micro-forming process

In order to address the shortcoming of distorted workpiece, a new blank holder shown in **Figure 2.6** is designed to not only hold the metal workpiece firmly, but also apply tension to eliminate potential bending. The assembly has a two-bracket design that can be clamped by bolts. There is an 8 mm diameter hole in the center to perform forming operations. The lower bracket includes a protruded feature (marked in **Figure 2.6**(b)) around the hole to apply isotropic tension. When the brackets are being tightened, friction from top bracket will slide the metal piece along its protrusion and create a small tension in it. Applying a rubber pad underneath the top bracket can help build up a much higher tension, but it can result in the metal piece being adhered to the rubber pad, and there is no effective way of peeling the specimen off without visible distortion. In

practice, rubber pads are applied in some benchmark tests, where formed parts are analyzed without being peeled off, and the results indicate better surface flatness.

A three-axis CNC system is setup to provide precise three-dimensional motion as shown in **Figure 2.7**. Three linear stages (Siskiyou – 200cri), with point-to-point motion accuracy of 2 μm and maximum range of 50 mm, are assembled in perpendicular directions to conduct the experiments. The maximum load capacity is 10 lbs., which is much higher than the forming force plus inertia of micro-forming. The assembled three-axis motion system is calibrated using a cubic motion with 25 mm side length, and the errors are digitally compensated for by incorporating the calibration results into a motion control software. The linear stages are driven by NAI MC-4SA motion controller. The controller is interfaced in LabView and enables blended three-axis motion with a maximum velocity of 2 mm/s. A force transducer (ATI gamma F/T sensor) is mounted underneath the lower bracket to track force history during forming operation. The transducer provides six-axis force readings with a resolution of 1/160 N and 1/80 N in in-plane and axial direction, respectively.

2.4 Toolpath Generation

In incremental micro-forming, forming tool moves in a predefined contour or helical-type path over a flat surface to introduce collection of tiny indentations and produce a part with designed 3D complex shape. In contour-type toolpath, tool moves at a constant depth (in XY – plane, always perpendicular to the part axis) to complete one revolution and then steps down by the designed amount of step-size to start a new revolution as shown in **Figure 2.8**(a). In helical-type toolpath, tool gradually moves in the downward direction as well as in XY – plane direction to avoid any sudden jumps as shown in **Figure 2.8(**b). Co-ordinate points are finally generated on these curves, be in contour or helical, to feed in the CNC machine or LabVIEW program.

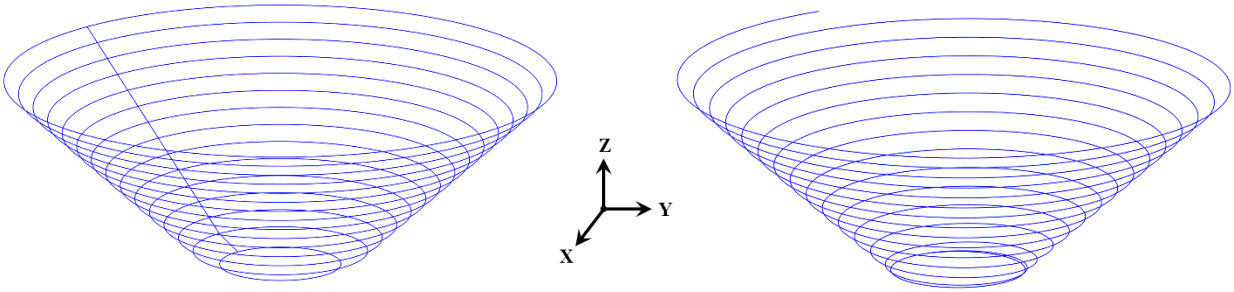

(a) Contour – type toolpath (b) Helical – type toolpath

Figure 2.8: Contour and helical-type toolpaths designed for incremental forming process

For a part geometry with truncated cone or pyramid shape, contact points on a cross section in Y-Z plane are first generated at pre-selected step size as shown in **Figure 2.9**. These points are later revolved about Z – axis (center of part axis) at a constant angle interval to generate axisymmetric geometry. Similarly, the same cross-sectional contact-points are translated on a rectangular path to generate toolpath for pyramidal geometry. Part geometries are designed to have an opening radius R with upper and lower fillet radii of R_1& R_1 so that any indentations are gradually introduced on the part rather than a quick plunge.

The coordinates of points A and B in **Figure 2.9** are given as:

$$z_A = 0 \; and \; x_A = x_B + PO_1 \tag{2.1}$$

$$z_B = (AO_1 - BP) \; where \; AO_1 = -R_1 \; and \; BP = -R_1 \cos\alpha$$
$$\text{i.e., } z_B = -R_1 \, (1 - \cos\alpha) \tag{2.2}$$

Now, by using the linear interpolation between points B and C, the x – coordinate for point B can be calculated as:

$$x_B = \frac{R_1(1 - cos\ \alpha)}{tan\ \alpha} - R \tag{2.3}$$

From Equations (2.1) and (2.3), x_A is calculated as:

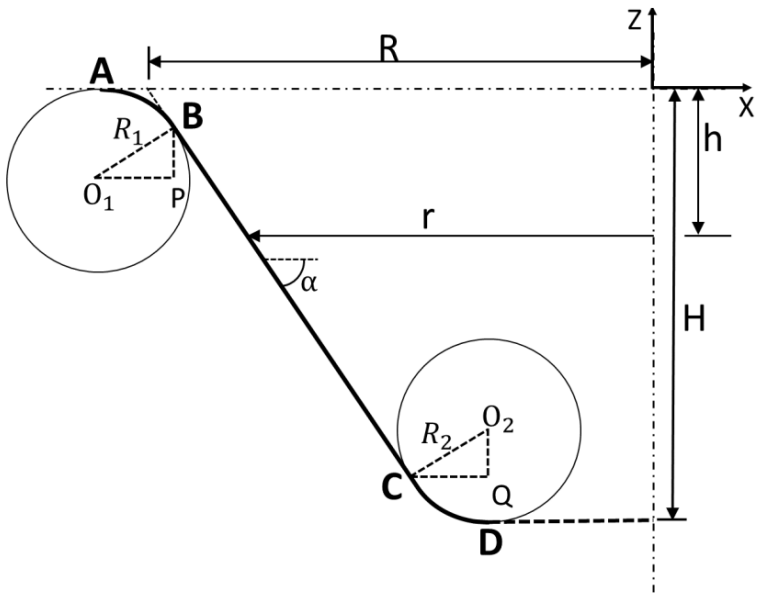

Figure 2.9: Cross sectional profile of an axisymmetric geometry used for toolpath generation

$$x_A = \frac{R_1(1 - cos\ \alpha)}{tan\ \alpha} - R - R_1 sin\ \alpha \tag{2.4}$$

Similar to points A & B, coordinates for points C & D can be given as:

$$x_C = \frac{H - R_2(1 - cos\ \alpha)}{tan\ \alpha} - R \qquad and \qquad z_C\ = -H + R_2\ (1 - \cos\alpha) \tag{2.5}$$

$$x_D = \frac{H - R_2(1 - cos\ \alpha)}{tan\ \alpha} - R + R_2 sin\ \alpha \qquad and \qquad z_D\ = -H \tag{2.6}$$

After calculating the above coordinates, individual points at a given step size (Δz) between A-B and C-D are calculated using the equation of a circle whereas, points between B-C are calculated using the linear interpolation method. Now that the complete set of points are available on the cross section designed in **Figure 2.9**, contour points for the full geometry are generated by revolving these points along the X – axis. Assuming that N number of points are needed on a single contour, individual points (x_i) are multiplied by the rotation matrix as shown below for a set of

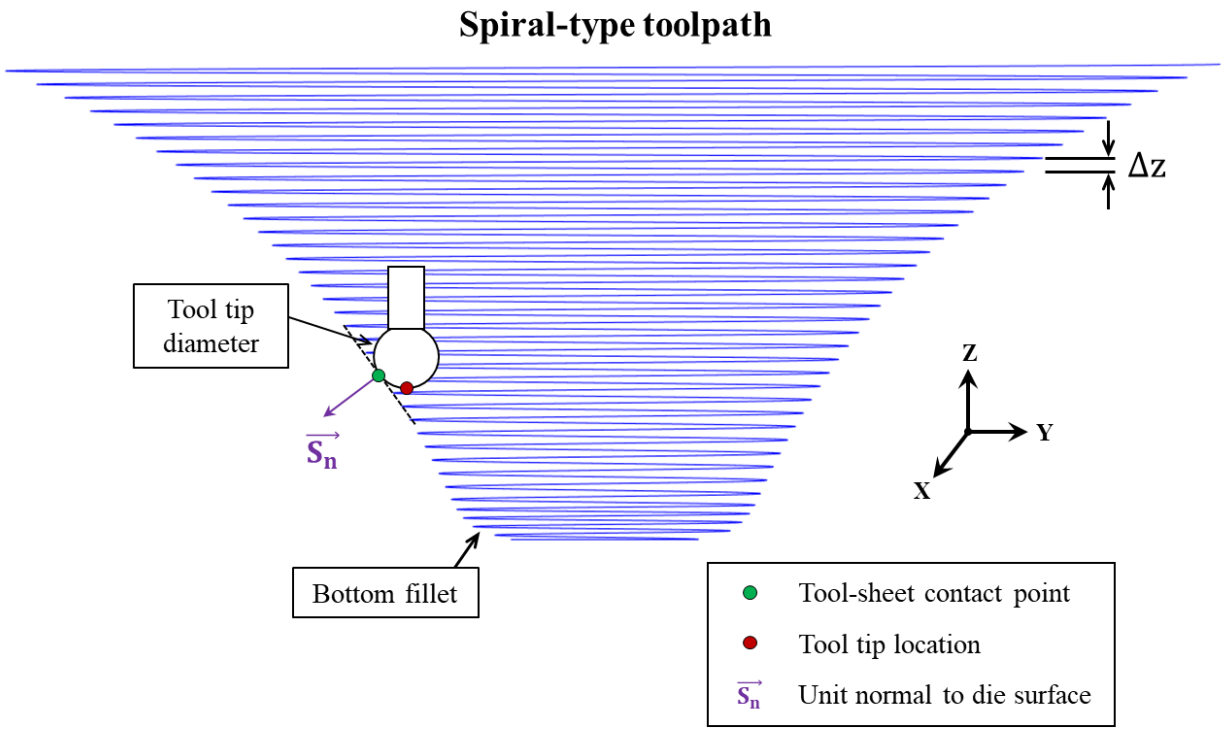

Figure 2.10: Spiral-type toolpath generated for incremental micro-forming of thin metal foils with input parameters of part geometry, tool diameter and step size (Δz)

angular values in $\theta = \frac{2\pi}{N} n$ where n = 1 to N. MATLAB script is created to systematically perform the required calculations.

$$[X'] = \begin{bmatrix} \cos\theta & -\sin\theta & 0 \\ \sin\theta & \cos\theta & 0 \\ 0 & 0 & 1 \end{bmatrix} [X] \tag{2.7}$$

From the above presented calculations, tool contact points of the designed geometry are successfully generated. However, for the experimental setup, tool-tip points need to be loaded on the machine for better consistency as tool contact point location keeps changing on the tool surface. Therefore, the relationship between tool-tip and tool-contact points is defined by Equation (2.8).

$$\vec{T} = \vec{S} - TR * (\overrightarrow{S_n} + \hat{k}) \tag{2.8}$$

Here, $\vec{T}$ is the tool-tip point, $\vec{S}$ is the tool-contact point, TR is forming tool radial, $\overrightarrow{S_n}$ is the surface normal at tool-contact point and $\hat{k}$ is the unit normal along Z – axis as shown in **Figure 2.10.**

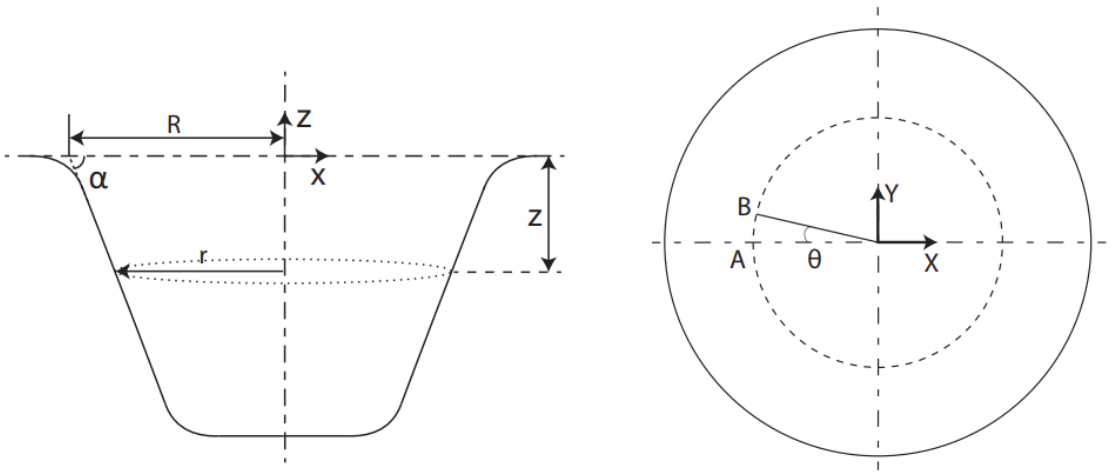

(a) Front view (b) Top view

Figure 2.11: Schematic to generate tool contact points throughout the geometry based on cross sectional points

Contour-type toolpath creates a rim on part geometry and results in a peak in axial force during tool step down, which is also demonstrated previously by Skjoedt et al. [19]. To minimize this effect, spiral-type toolpath is generated by interpolating a curve between two consecutive contours. Consider two contours are located at depth Z and $Z + \Delta z$ respectively and on these contours the coordinates of N number of points are already determined by above-described methods. Hence the points on the helical path between these contours can be interpolated as:

$$X''_n = \frac{X'_1 L_{1n} + X'_2 (L_t - L_{1n})}{L_t} \tag{2.9}$$

Here, $[X'']$ is the coordinates of the nth point of the helical path, $[X'_1]$ and $[X'_2]$ are the coordinates of the first and second points on the contour at height Z respectively, L_{1n} is the length between first and nth point and L_t is the total length of the contour located at height $Z + \Delta z$.

2.5 Results and Discussion

Miniaturized parts such as truncated cones, funnels and pyramids were produced using AL 5052-H19 and AL 1100 foils to demonstrate the capabilities of single-point incremental micro-forming (μSPIF) process. Aluminum foils were 50 μm thick and manually cut using shearing machine into approximately 25 mm × 25 mm pieces with minimum visible distortion. Two different micro-indenters (forming tools) with hemispherical ended tip of 150 μm and 200 μm diameter are employed to carry out the experiments. With 50 μm thick foils, the ratio of tool diameter over sheet thickness ranges from 2 to 3, which is significantly lower than that for conventional ISF. In this section, the comprehensive review of our results of μSPIF on aluminum alloys are presented to highlight the process limitations and scope for future improvement. In particular, the evolution of forming forces, level of geometric accuracy and part formability in μSPIF based on experimental analysis are presented below.

2.5.1 Geometric deviation and thickness distribution of μSPIFed parts

Industrial application of any sheet metal part fabricated using ISF process requires acceptable geometric and dimensional accuracy. Two truncated conical geometries are designed as shown in **Figure 2.12** and fabricated using two different aluminum alloys (AL 1100 and AL 5052-H19) to investigate the extent of geometric accuracy achieved in μSPIF. Process parameters and blank material used to perform these experiments are listed in **Table 2.1**. It is generally observed throughout the experiments that large geometric deviation is observed near the part opening region due to missing support on the non-tool side of the specimen. This drawback is addressed in the literature by either adding a support plate or a numeric controlled support tool to its back side.

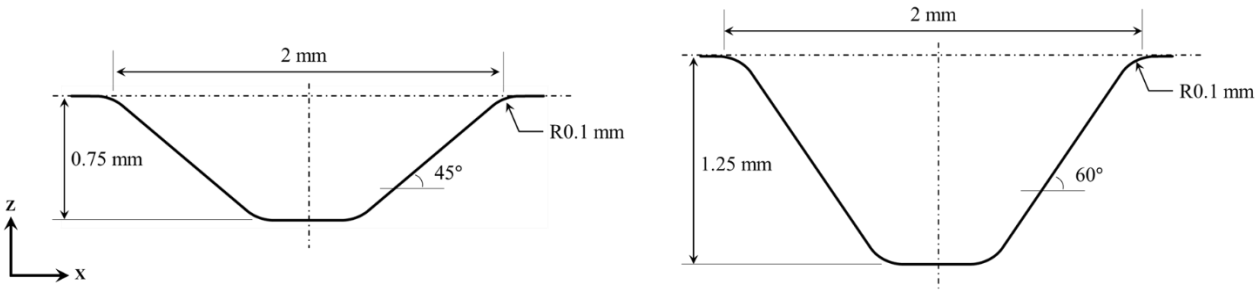

(a) Baseline geometry: Cone 45º (b) Baseline geometry: Cone 60º

Figure 2.12: Baseline geometries with truncated conical shaped designed for comprehensive investigation of µSPIF process

After fabrication, µSPIFed parts are removed from the clamps to allow global springback. They are later mounted in a transparent epoxy which is grinded and polished as shown in **Figure 2.13**(a) to optically measure their cross-section profiles using an Olympus DXS – 510 profilometer. These experimentally measured profiles, cross-sectioned along X-Z plane, are compared against the designed part cross-sections shown in **Figure 2.12** to calculate geometric deviation. Geometric deviation between experimentally obtained and designed part profile is defined as the distance between these profiles along the surface normal vector originating from designed profile.

Table 2.1: Process parameters and material used for the study of geometric deviations in µSPIFed parts

Part	Material	Opening diameter (mm)	Wall angle (degree)	Tool diameter (µm)	Step size (µm)	Height (mm)
Cone A	AL 1100	2	60	250	10	1.25
Cone B	AL 5052	2	45	150	10	0.75
Cone C	AL 5052	4	45	150	10	1.50

In case of cone A, formed using AL 1100 foil and tool diameter of 200 µm, maximum deviation between designed and experimentally measured profile is close to 150 µm in the bending

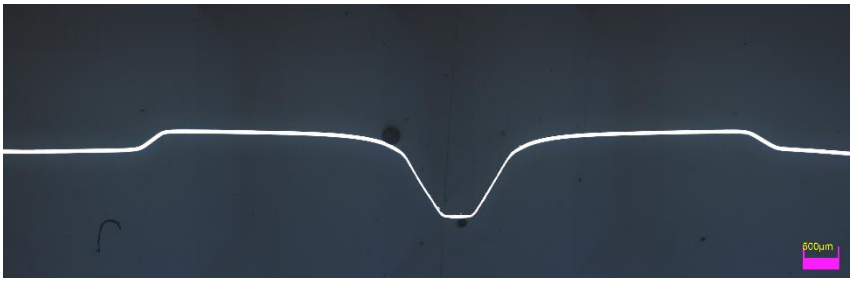

(a) Cross sectional geometry mounted and polished in epoxy

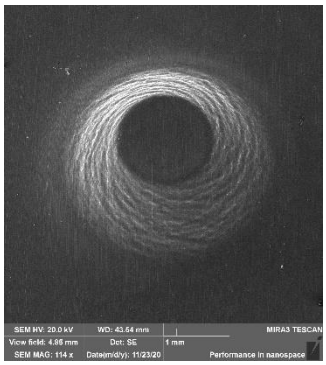

(c) SEM image: non-tool side

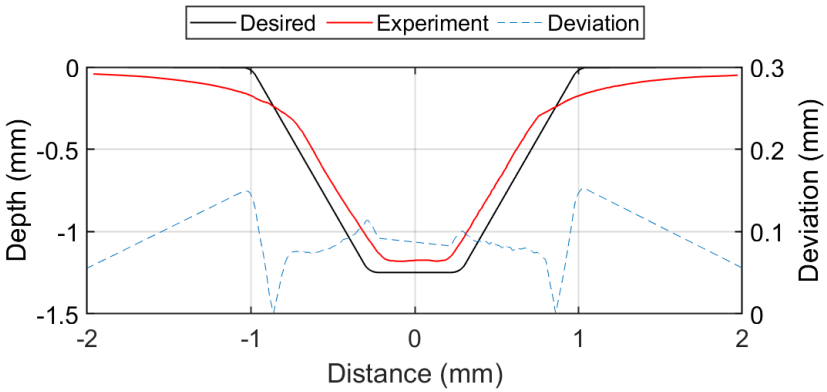

(b) Cross sectional comparison with designed profile

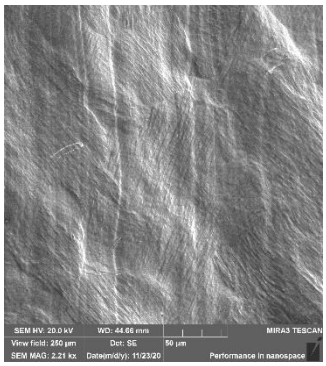

(d) Enlarged view of (c)

Figure 2.13: Experimentally formed cone 60º part using AL 1100 material and its comparison with the designed part geometry

region (**Figure 2.13** (a)) due to the absence of any local support at the bottom of the sheet. However, the deviation is less than 100 µm in constant wall angle region as plotted in **Figure 2.13**(b). This deviation can be attributed to the combination of sheet springback, elastic deflection of the forming tool and machine compliance under the influence of radial forces. When inspected under the SEM, cone A shows a subtle twist in the geometry along circumferential direction as observed in **Figure 2.13**(c) and (d). Based on FE analysis, it is determined in a later chapter that µISF tends to have much higher level of friction coefficient between tool-sheet interface compared to macro-scale ISF. Therefore, forming tool induces higher circumferential strain leading to a twist

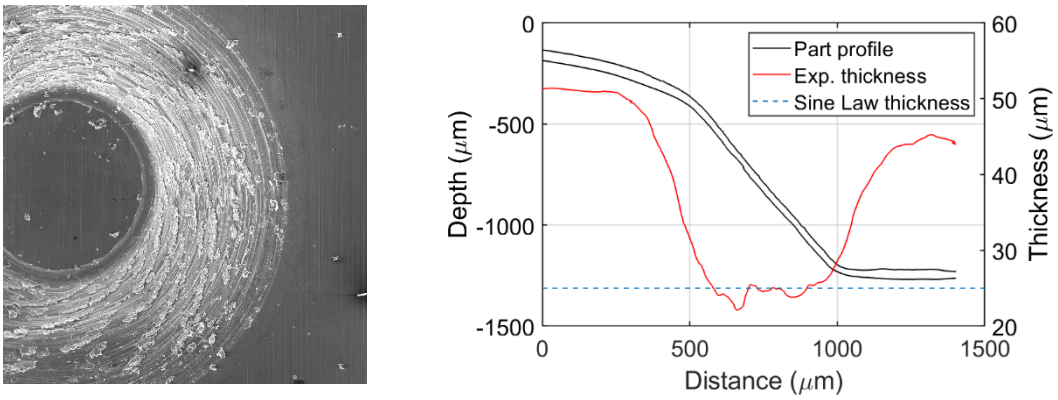

(a) SEM image: Tool-side surface (b) Final thickness distribution

Figure 2.14: SEM image of the tool-side surface and final sheet thickness distribution of cone 60º part formed using AL 1100 material

like feature along the tool motion direction. The SEM image of tool-side surface shows significant chipping or wear of the top surface shown in **Figure 2.14**(a) due to tool movement. This explains a few sharp dips in the part's thickness distribution plotted in **Figure 2.14**(b). Otherwise, the overall part thickness shows even distribution and can be successfully explained by the Sine law ([20], [21]) based on the assumptions of shear deformation and plain – strain condition in plane perpendicular to the tool motion direction (X-Z or Y-Z plain).

$$\underline{\text{Sine law}}: \; t_f \; [\text{Final thickness}] = t_0 \; [initial \; thickness] * \sin\left(\frac{\pi}{2} - \alpha\right) \qquad (2.10)$$

Similarly, the other two tests for cone 45º are performed on AL 5052 material in H19 condition (pre-strain hardened). Here, cone B is designed with an opening diameter of 2 mm whereas cone C is designed with an opening diameter of 4 mm. The geometric deviation obtained in these cases are approximately 91 µm and 120 µm respectively after constant wall region is attained as shown in **Figure 2.15**(b) and (d). Though the magnitude of geometric deviation in these cases is fairly similar to that obtained in case A, the thickness distribution in cones B and C cannot be explained by the Sine law. It is hypothesized that dominant shear deformation condition can be easily assumed for parts formed using AL 1100 due to its high ductility with lower flow stress.

However, same cannot be said about the parts formed using AL 5052 – H19 material. It has much higher flow stress and could induce stretching mode of deformation. If true, this violates the

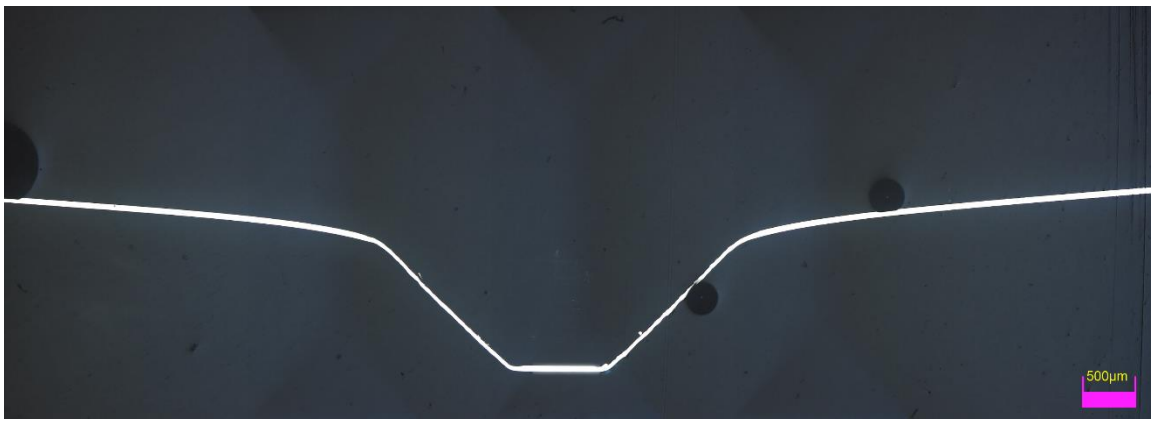

(a) Cross sectional geometry mounted and polished in epoxy

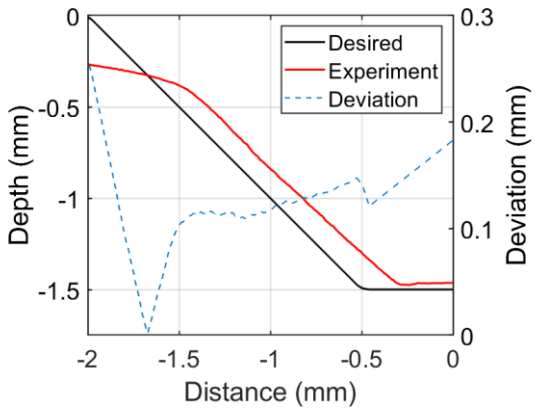

(b) Profile comparison: Cone C

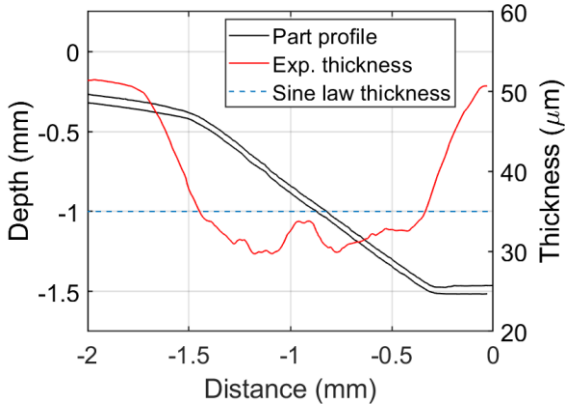

(c) Thickness: Cone C

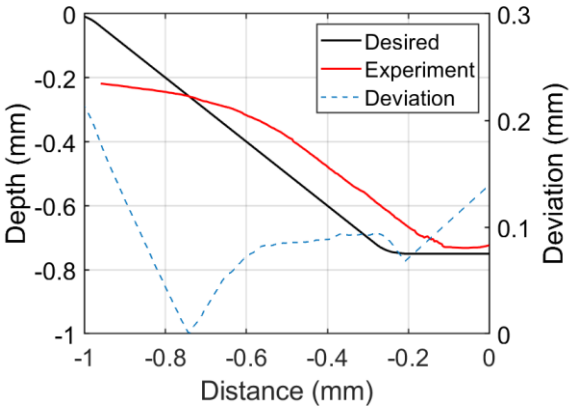

(d) Profile comparison: Cone B

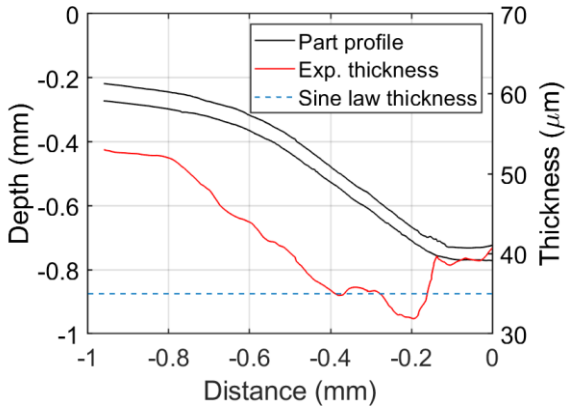

(e) Thickness: Cone B

Figure 2.15: Comparison of experimental and designed cross sectional profiles of cone 60º geometries with their corresponding thickness distribution

previous assumptions and therefore the Sine law cannot explain the thickness distribution in case of cones B and C as shown in **Figure 2.15**(c) and (e) respectively.

2.5.2 Variation of forming forces with process parameters

Variation in forming forces is recorded in x, y and z directions throughout the fabrication of cone B (**Table 2.1**) and plotted as shown in **Figure 2.16**. Force in z-direction coincides with axial (out-of-plane) direction of the part and forces in x and y-direction are in-plane forces along rolling and transverse material directions respectively. It can be observed from the plot that force trend can be divided into two different zones: (a) initial bending and (b) constant wall angle. Similar observation is previously presented by Hmida et al. [22]. Bending near the opening region in SPIF is extensively reported in literature (Ambrogio et al. [23], [24]) and occurs because of missing support on non-tool side of the specimen. Similar behavior is also noticed during the study presented in the previous subsection 2.5.1. Axial force increases from zero to F_{peak} in initial bending zone and then either stabilizes or gradually drops from F_{peak} to F_{end} in constant wall angle zone as depicted in **Figure 2.16**(a). F_{peak} is reached at a depth of 0.28 mm which implies that bending zone is transitioning to constant wall angle zone at this point. This phenomenon can be cross validated by comparing experimentally measured and designed cross-sectional profiles presented in **Figure 2.15**(d).

Enlarged view of these forces in constant wall angle zone from depth 0.35 mm to 0.4 mm is exhibited in **Figure 2.16**(b). A cyclic nature in axial force can be clearly observed with its fluctuation from 1.69 N to 1.91 N (region between red dotted-lines). In other words, a force variation of 13% can be seen in axial direction when tool moves from positions A to B and similarly from B to D. Similar cyclic effect is also evident along forces in x and y-directions. This variation in axial force can be attributed to various reasons such as:

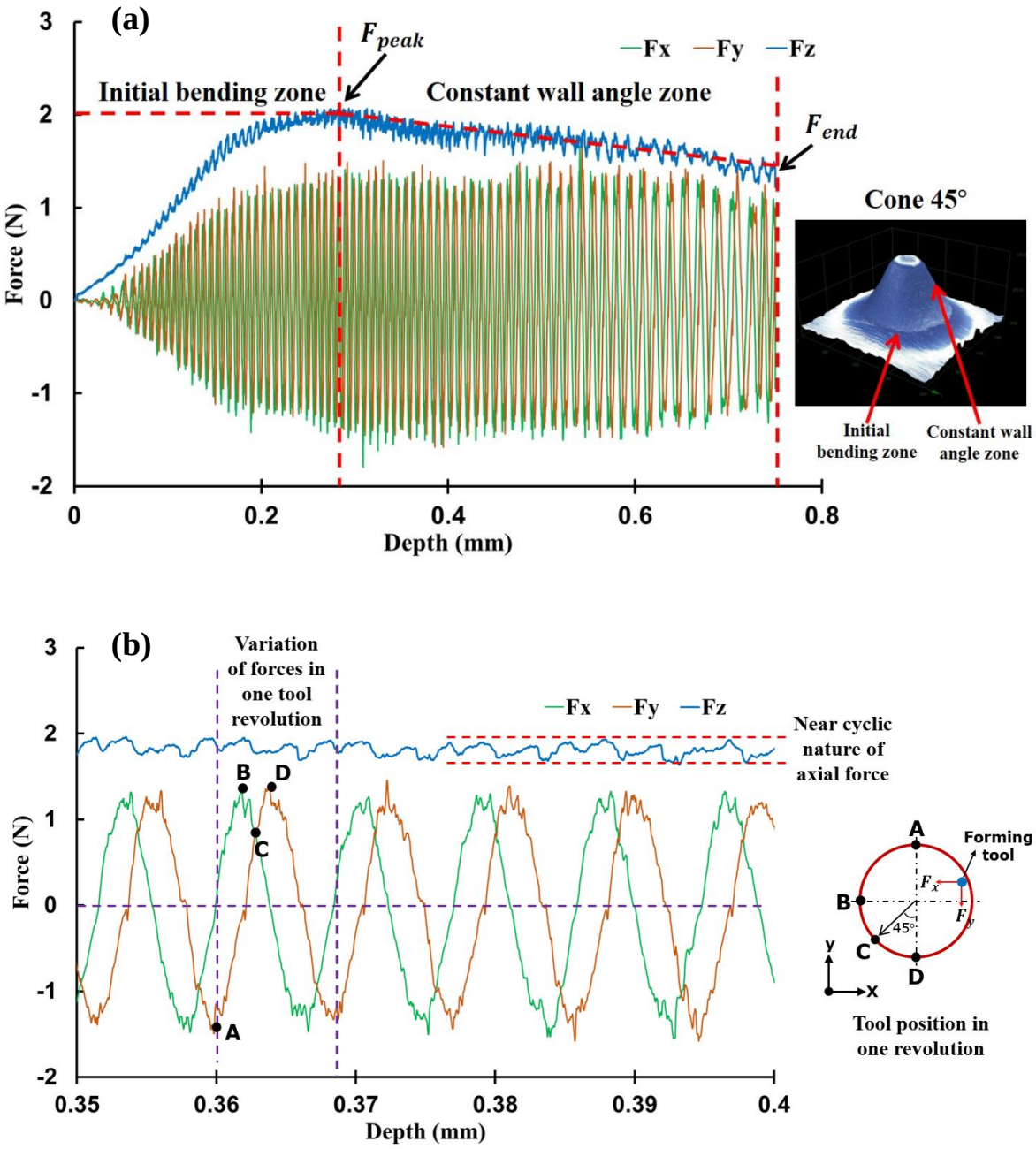

Figure 2.16: Experimentally measured: (a) reactionary forces recorded in x, y and z directions with respect to the part depth and (b) enlarged view of the forces between depth 0.35 mm and 0.4 mm in constant wall angle zone.

- Experimental setup has different compliance in x and y – directions. Therefore, the amount of deformation along these directions are slightly different leading to cyclic nature in forming forces.

- Strain hardened material like AL 5052 – H19 has material anisotropy in rolling and transverse directions that requires different forces to induce same displacement-controlled deformation.
- The raw material foil used for experiments does not have a constant thickness value but tends to fluctuate over the surface between 53 ± 1 µm as shown in **Figure 2.17**. And forming forces are directly proportional to the sheet thickness leading to fluctuation in force values as well.

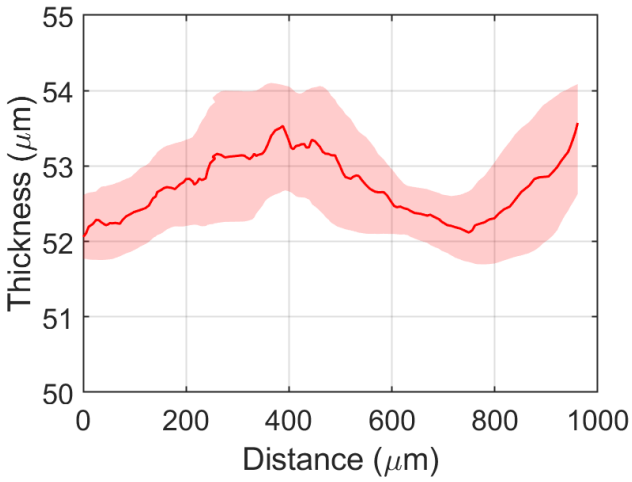

Figure 2.17: Initial sheet thickness of AL 5052-H19 sheet used for the experiments

Similar to the above case, another truncated cone with 45º wall angle is formed with same process parameters but with different virgin material, AL 1100. Forming forces during fabrication are recorded along x, y and z-directions as shown in **Figure 2.18.** The moving average of the force values is plotting in the figure to better understand the subtle trends with moving data range plotted in the background as faded color band. Contrary to that of cone B, forming forces in this case saturate at the F_{peak} value and do not gradually dip after the initial bending zone. Axial and in-plane force values saturate at approximately 0.51 N and 0.44 N respectively. Generally, in macro-scale ISF processes, in-plane forces are much lower compared to axial forces [25]. However, they are relatively higher in micro-scale ISF due to higher friction coefficient between tool-sheet interface. Further analysis using FEA better explains this phenomenon in chapter 4.

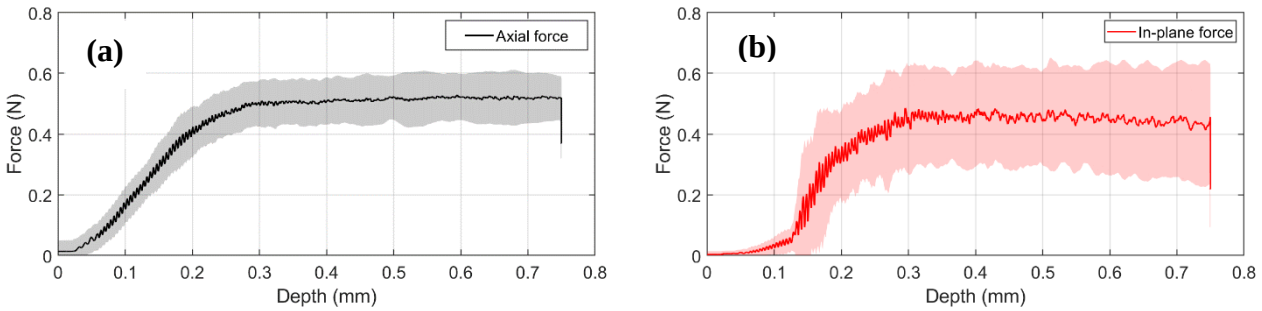

Figure 2.18: Variation in forming forces along (a) Axial direction and (b) in-plane direction during the fabrication of cone 45º part using AL1100 material

To study the effect of process parameters such as tool diameter and step size on forming forces, cone 45º part designed in **Figure 2.12**(a) and funnel part designed in **Figure 2.20** are formed using AL 5052 – H19 material. Baseline process parameters for these tests are kept constant at: step size Δz = 10 µm, tool diameter = 150 µm, feed rate = 9.6 mm/min and sheet thickness = 50 µm. Average value of forming forces in stable wall region are compared. In case of cone 45º, four different step sizes between 5 and 20 µm are used in experiments and the corresponding forces are plotted in **Figure 2.19**(a). It can be observed from the figure that both axial and radial force values linearly increase with the increase in step size. For the increase in step size from 10 µm to 15µm (change of 50%), axial force increased by 19.9% whereas radial force increased by 28.9%. Similar behavior is observed with funnel part geometry when experiments are performed using step size values of 5, 10 and 15 µm as shown in **Figure 2.19**(b). For the increase in step size from 10 µm to 15µm (jump of 50%), axial force increased by 21.0% whereas radial force increased by 23.3%. However, such increase in radial force value is not observed with increase in tool diameter. When it is increased from 0.15 mm to 0.25 mm, radial force values only increase my 5.8% and 2.1% in case of cone 45º and funnel part respectively, whereas these values in axial direction increases by 8.1% and 20.0% respectively.

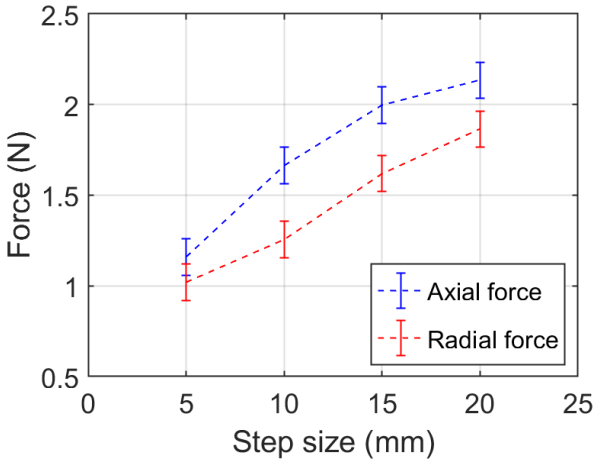

(a) Effect of step size in cone 45º

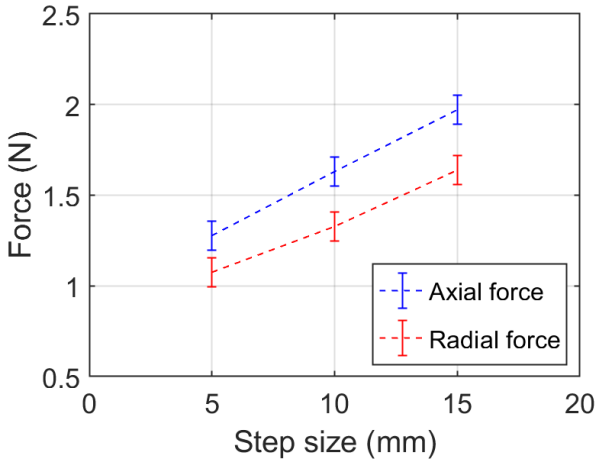

(b) Effect of step size in funnel part

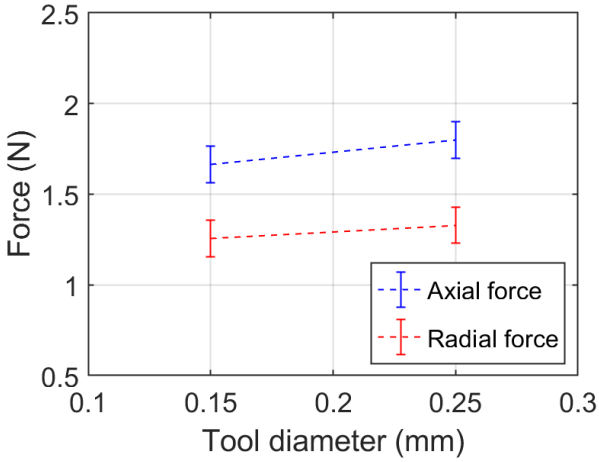

(c) Effect of tool diameter in cone 45º

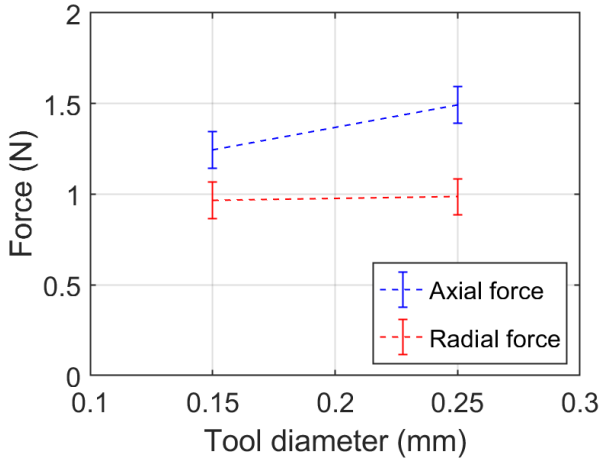

(d) Effect of tool diameter in funnel part

Figure 2.19: Effect of different step sizes and wall angles of variation of axial and in-plane force values when a cone 45º geometry is formed on AL 5052 – H19 material using 150 µm tool diameter

2.5.3 Material formability test in µSPIFed parts

Similar to geometric accuracy, having good material formability is also desired for industrial application of aluminum alloys. In traditional manufacturing techniques, material formability is described through a forming limit diagram (FLD) with major and minor strains along its axes. By contrast in ISF, it is reported in terms of maximum wall angle that can be successfully

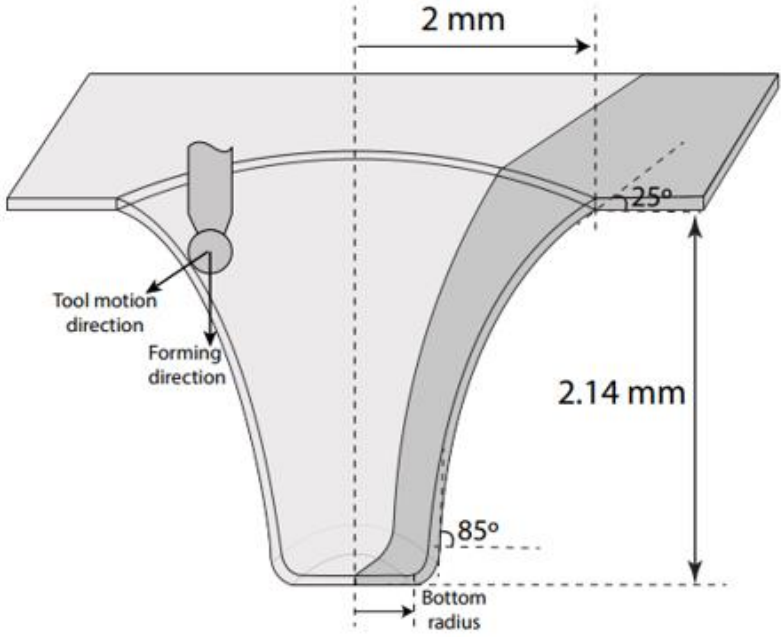

Figure 2.20: Geometry of a funnel shape part designed to study the material formability in µSPIF process

formed. A funnel shaped geometry with wall angle ranging 25º to 85º and opening diameter 4 mm is designed as shown in **Figure 2.20**, and fabricated to identify the forming limit of AL 5052-H19 material in µSPIF process.

Due to the small part size, it is difficult to visually identify the location of crack opening. Therefore, force variation along x, y and z directions is monitored throughout the experiment to determine the accurate location of crack initiation by sudden drop in axial and in-place forces. Different set of process parameters used to analyze the parametric effect on material formability is listed in **Table 2.2**. The moving average of the forces with their corresponding standard deviations is plotting in **Figure 2.21**. It can be clearly observed from the plots that as soon as a crack on the part surface is initiated, force values start dropping and the standard deviation band starts to widen due to high force fluctuations between cracked and uncracked regions.

Table 2.2: Process parameters used for the formability tests of AL 5052 - H19 material in µSPIF process and the obtained fracture depth.

Part no.	Material	Opening diameter (mm)	Tool diameter (µm)	Step size (µm)	Height (mm)	Fracture depth (mm)
1	AL 5052	4	150	5	2.14	0.38
2	AL 5052	4	150	10	2.14	0.49
3	AL 5052	4	150	15	2.14	0.53
4	AL 5052	4	250	5	2.14	0.58
5	AL 5052	4	250	15	2.14	0.63

When a smaller step size is used in the experiments, the tool overlap of material under deformation between prior and current toolpath contours increases as previously explained for thickness prediction by Bansal et al. [26]. Each section of material under deformation goes through higher number of loading and unloading cycles leading to high strain hardening. This phenomenon initiates crack in the part much earlier and leads to failure in the part. Therefore, it can be seen from the **Figure 2.21**(a) and (b) that forming depth of the funnel part linearly increases with the increase in step size. This means, higher strain at failure is obtained with bigger step size. Keeping the assumptions of volume constancy and plain strain deformation condition intact, equivalent strain near fracture can be calculated using the Sine law and the Equation 2.11:

$$\begin{aligned} &\text{[Volume constancy]} && \varepsilon_1 + \varepsilon_2 + \varepsilon_3 = 0 \\ &\text{[Plane – strain condition]} && \varepsilon_2(circumferencial\ dir.) = 0 \\ &\text{[Thickness direction strain]} && \varepsilon_3 = \log\left(\frac{t_f}{t_0}\right) \\ &\text{[Equivalent strain]} && \varepsilon_{eq} = \frac{2}{\sqrt{3}} * \varepsilon_3 \end{aligned} \tag{2.11}$$

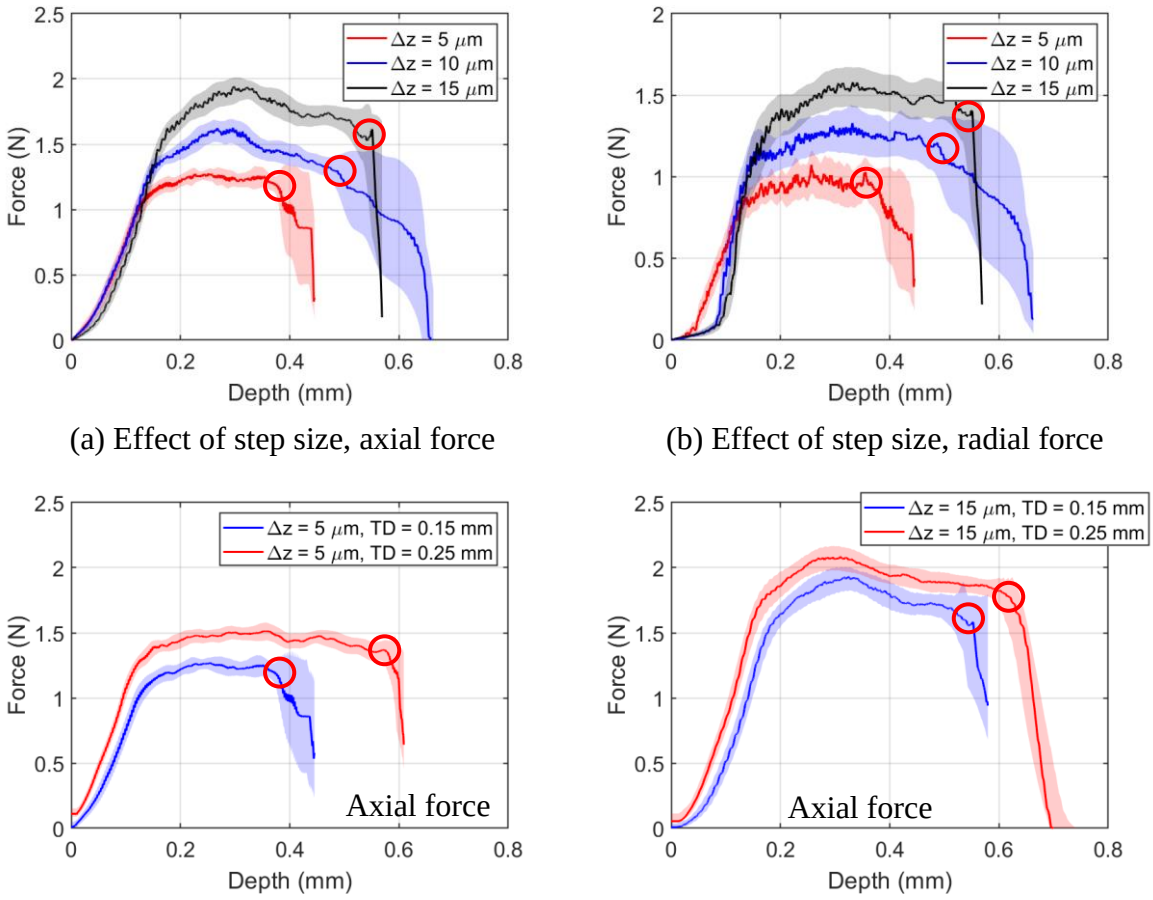

(a) Effect of step size, axial force

(b) Effect of step size, radial force

(c) Effect of tool diameter, Δz = 5 µm

(d) Effect of tool diameter, Δz = 15 µm

Figure 2.21: Effect of step size and tool diameter on forming forces and material formability of AL 5052 - H19 in µSPIF process. Red circles on the plot represent the point of fracture initiation.

Similarly, two different tool diameters of 150 µm and 250 µm tip are used to study its effect on material formability. Based on the previous argument for the effect of step size, smaller tool size should be able to provide better formability. However, using Silva's [27] analytical model to demonstrate the failure mechanism in incremental forming of metals, larger tool size provides a stabilizing effect of dynamic bending under tension in the material deformation zone. This effect is capable of raising the material formability in ISF process compared to that found in conventional stamping or deep drawing. Compounding this effect, thin metal foils used in this study has only three to five grains in the thickness direction. Larger tool size helps induce an even strain gradient

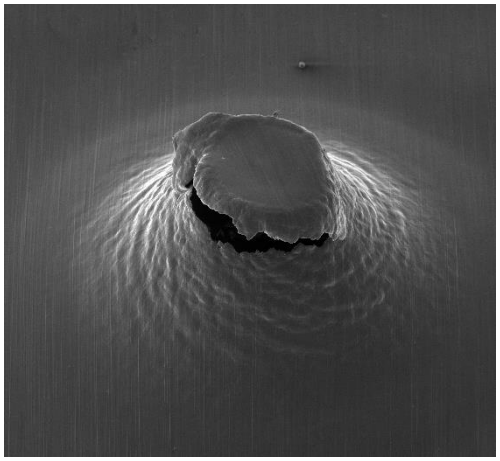

(a) SEM image of a fractured funnel

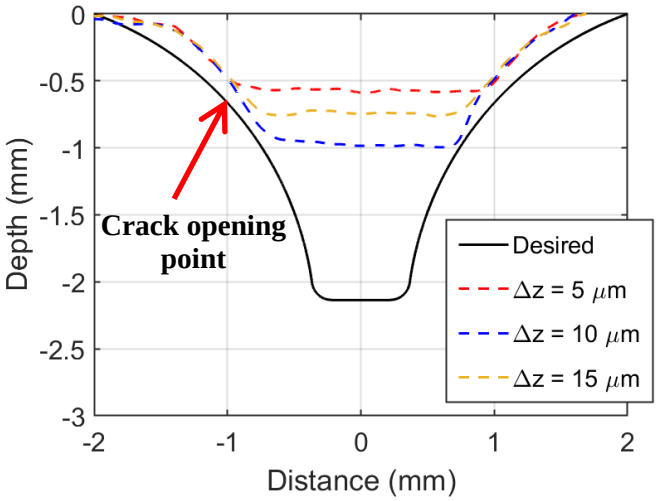

(b) Comparison of cross-sectional profiles

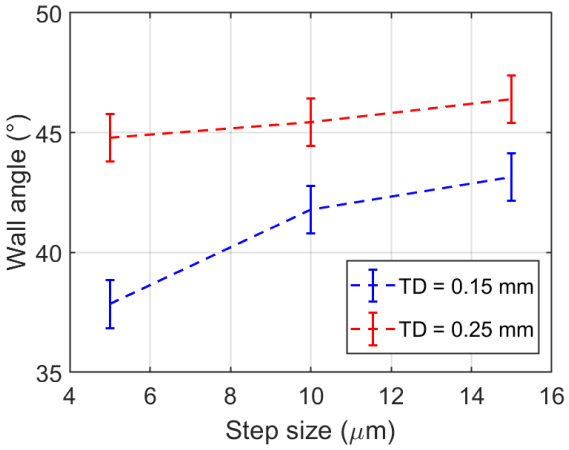

(c) Effect of process parameters on wall angle at failure

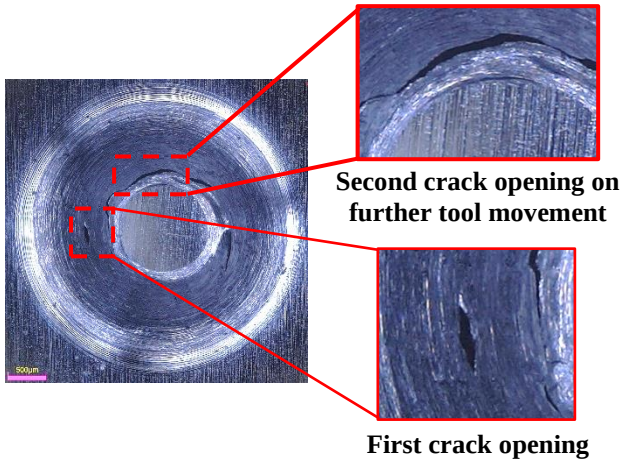

(d) Cracks opening on part surface

Figure 2.22: Truncated funnel shape designed with wall angle from 25º to 85º and formed using AL 5052-H19 foil to understand material formability

among neighboring grains. Therefore, it also provides better material formability as confirmed in case of AL 5052 – H19 material as shown in **Figure 2.21**(c) and (d) for two different step sizes of 5 µm and 15 µm respectively.

Other than sheet spring-back and tool deflection, material twist also contributes to geometric inaccuracy in incremental forming process (Jeswiet et al. [28] and Duflou et al. [29]).

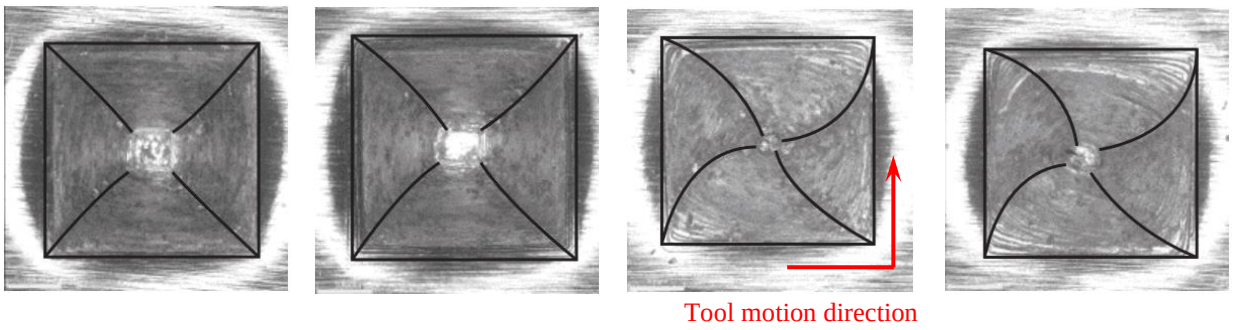

(a) $\Delta z = 5$ µm (b) $\Delta z = 10$ µm (c) $\Delta z = 15$ µm (d) $\Delta z = 20$ µm

Figure 2.23: Effect of step size on twist observed by under optical microscope with the increase in step size from 5 µm to 20 µm then formed on AL 5052 - H19 material using tool diameter of 200 µm.

But these two phenomena are considered independent to each other. Although, in µISF, material twist appears to be dependent on tool deflection induced due to in-plane forces. An experimental investigation is conducted to strengthen this hypothesis by fabricating four truncated pyramids using AL 5052 – H19 foil, varying step size from 5 µm to 20 µm and keeping other process parameters constant. A relationship can be inferred between step size and material twist from optically imaged pyramids shown in **Figure 2.23**. Corner ribs of formed pyramids are highlighted in black color for better representation of material twist. It tends to increase with increase in step size based on qualitative observations. It must be noted that the part geometry is twisting in clockwise direction whereas the tool motion is designed in anti-clockwise direction. Therefore, this twist cannot be attributed to the shear strain in circumferential direction. Due to increase in in-plane forces caused by increasing step size, forming tool starts elastically deflecting in the direction opposite to tool motion and creates a twisted feature on the part. That being the case, this problem can be mitigated by making the tool length shorter and stiffer. But a toolpath correction strategy would be needed for further improvements. Further analysis of the part twisting needs to be performed using finite element analysis of pyramid geometry.

2.6 Summary and Conclusions

The study presented in this chapter investigates various elements of incremental micro-forming process such as evolution of forming forces, extent of part accuracy and material formability. A linear three – axis stage is custom designed and assembled with force sensor to perform the required experiments. The setup is further calibrated and tested in multiple scenarios to obtain repeatable and reliable results. Some of the conclusions that are drawn based on observations and results presented in this chapter are as follow:

- Cross sectional profiles of two different conical shaped parts with 45º and 60º wall angle are compared with their designed geometries to quantify the extend of geometric accuracy obtained in µISF process. Geometric deviation of 90 – 110 µm is obtained in all the presented cases and can be ascribed to sheet spring-back, tool deflection and machine compliance induced during fabrication process.
- While the nature of forming forces in incremental forming of both macro-scale and microscale parts resemble each other, 13% fluctuation in axial force is much higher in micro-scale parts compared to that obtained in macro-scale parts. This fluctuation could be contributed by planar anisotropy of AL 5052-H19 material. Also, the presence of only few grains along sheet thickness in conjunction with fluctuating initial sheet thickness in micro-scale parts can generate uneven material deformation and therefore bring these forming force fluctuations.
- Parametric analysis of forming forces shows that increase in step size linearly increase the forming forces in both axial and radial directions. Similar effect is also observed with the increase in tool diameter though at a smaller extent.
- Material formability of AL 5052-H19 foil is quantified in terms of maximum wall angle that can be successfully formed using µISF process. A truncated funnel shaped geometry is

designed to analyze it. Crack initiation is monitored by sudden drop in axial force value to accurately find the tool position at fracture. Parametric analysis of formability shows that decrease in step size leads to higher strain hardening and therefore results in fracture at lower strain values. Whereas larger tool diameter induces stabilizing effect of dynamic bending to get even deformation leading to better material formability.

- A novel feature twist is detected in experiments of pyramid shaped parts due to increase in step size and tool deflection in opposite to tool motion direction. It can be eliminated by either making the forming tools more rigid or improving toolpath planning strategy.

Chapter 3
Rapid Prototyping and Manufacturing of Aerospace Parts Using Two-point Incremental Forming Process

3.1 Introduction

Incremental sheet forming (ISF) has gained a lot of attention over the last two decades for rapid prototyping and manufacturing of sheet metal products with remarkably reduced setup cost and lead time. In contrast with other forming processes, ISF was developed as a cost efficient alternative suitable for fabricating parts with personalized geometric and mechanical properties. It has demonstrated widespread application in various industries such as automobile, aerospace and medical implants. Some of the major advantages of ISF are reduced forming forces and higher material formability due to its localized nature of deformation.

3.2 Literature Review

In a review article, Jeswiet at al. [28] reported that most sheet metal forming applications impose a dimensional accuracy of 1 mm. Some categories of parts would even require this value under 0.5 mm. These requested limits are typically exceeded when employing the ISF process. Therefore, attempts have been made to analyze its process mechanics and bring the dimensional accuracy under acceptable limits. Despite that, unwanted bending around the local deformation zone due to large unconstrained sheet reduces the part precision and consequently limit its ability to produce complex parts.

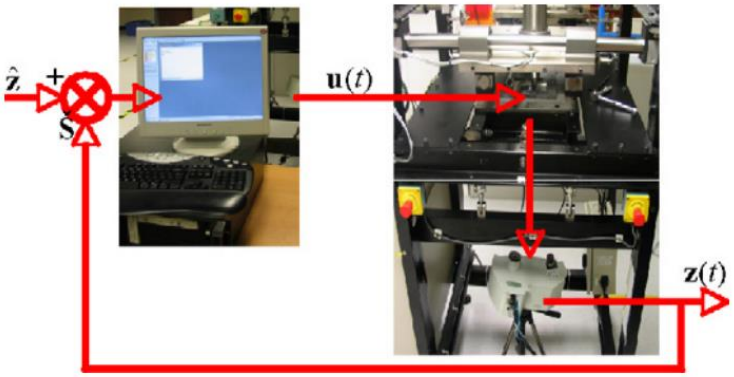

Figure 3.1: Single-point incremental forming process setup with feedback control (Allwood et al. [30])

3.2.1 Geometric accuracy

In SPIF process, Ambrogio et al. [23] studied the influence of process parameters on geometric accuracy using statistical analysis. They developed statistical model using ANOVA to predict geometric errors and proposed to compensate them in forming toolpath. Major drawback of this technique is that several experimental data points need to be generated priori and toolpath correction is performed offline. Allwood et al. [30] developed a closed-loop feedback control strategy illustrated in **Figure 3.1** by integrating stereovision camera to improve part accuracy in SPIF process. Though they obtained ±0.2 mm accuracy in targeted geometry, the presented strategy requires iterative experimental processing which made incremental forming less flexible.

Verbert et al. [31] conducted robot supported ISF experiments to fabricate large size products. Due to its low stiffness, they computed tool deflection from the compliance of each joint based on robot kinematics and compensated it in toolpath. Behera et al. [32] implemented a different toolpath correction technique based on error prediction using Multivariate Adaptive Regression Splines (MARS). It used a set of experimentally measured part accuracy data to train the regression model and generated continuous error response surfaces for toolpath correction.

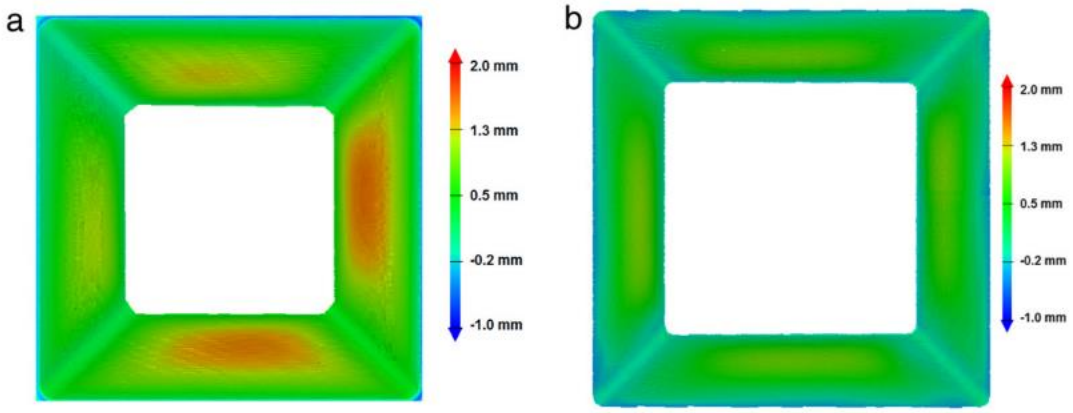

Figure 3.2: Top - view of accuracy color plots showing results of (a) uncompensated tool path test and (b) compensated tool path test using MARS predictions for ordinary non-horizontal planar features (Behera et al. [32])

When validated for trained geometries, it provided significant improvement in part geometry as compared in **Figure 3.2**.

Asghar et al. [13] observed that sheet and tool deflection were two major contributors of geometric deviation and proposed a new toolpath compensation strategy based on the estimation of part's elastic recovery. They experimentally demonstrated that part accuracy could be significantly improved by this strategy in both axisymmetric and freeform part geometries as compared in **Figure 3.3**. In case of cone 60º, part accuracy was shown to improve from 1.2 mm deviation to 0.3 mm deviation after toolpath compensation. Similarly, in case of funnel shaped part

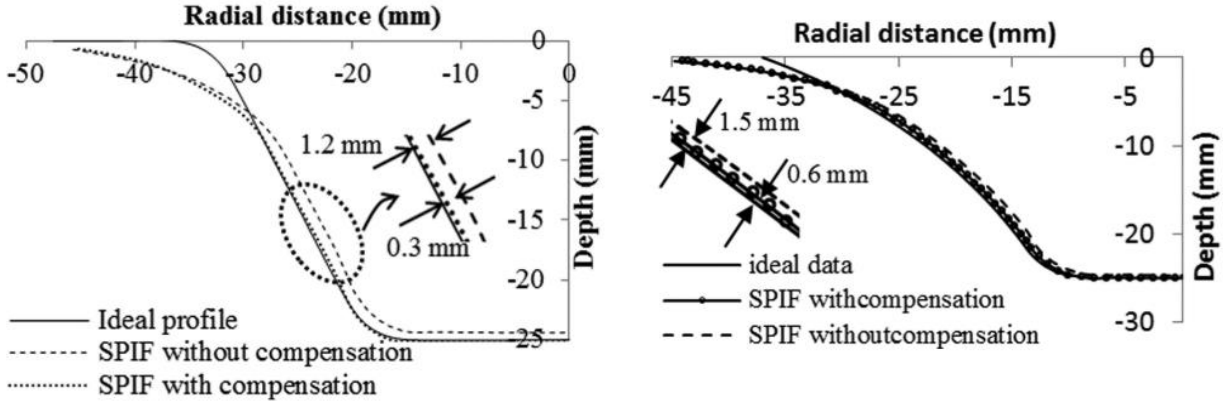

(a) Truncated cone of 60º wall angle

(b) Funnel shaped part with wall angle varying from 25º to 60º

Figure 3.3: Comparison of designed and experimentally measured part profiles for compensated and un-compensated SPIF toolpaths (Asghar et al. [13])

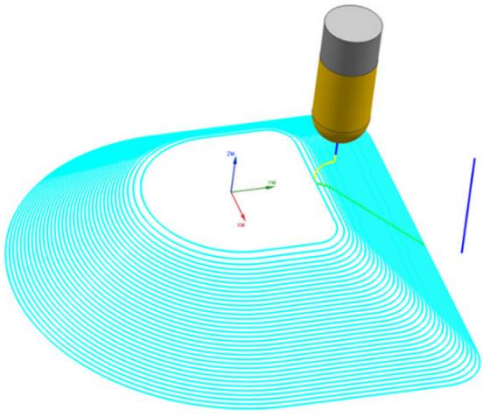

(a) Initial toolpath from CAD

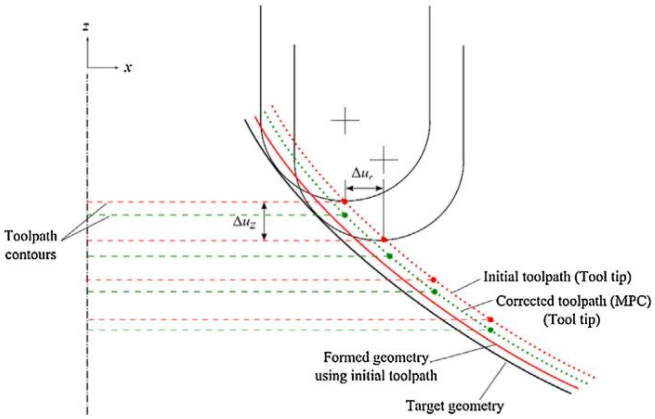

(b) Corrected toolpath by using MPC control algorithm

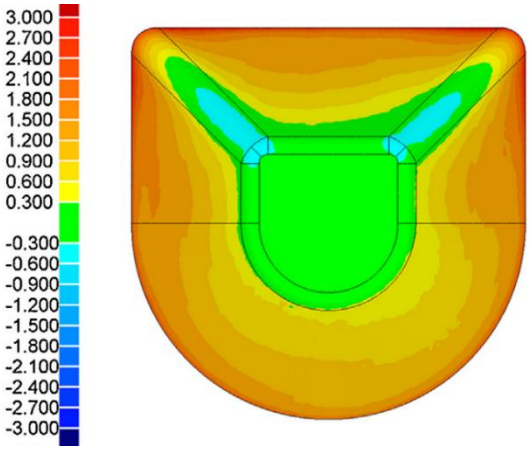

(c) Geometric accuracy with no toolpath correction software

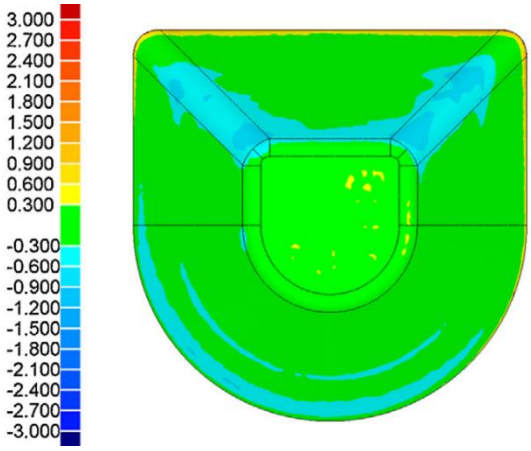

(d) Geometric accuracy with MPC toolpath correction software

Figure 3.4: Toolpath correction MPC algorithm proposed by Lu et al. [38] to improve part accuracy.

with wall angle varying between 25º and 60º, deviation improved from 1.5 mm to 0.6 mm. However, the proposed analytical equations for sheet springback assume that sheet deflection must be smaller compared to its thickness and therefore required modeler's judgement on its appropriate usage. Recently, Fiorentino et al. [33] integrated toolpath generation with an iterative learning algorithm based on artificial cognitive system for error estimation. The algorithm was experimentally tested using two different materials and shown to considerably improve part precision.

Two-point incremental forming (TPIF) process is the center of investigation in this chapter. In this process, a partial or a half-die is attached underneath the metal sheet for added local support to avoid any unwanted bending. It can be argued that adding a part-specific die reduces the process flexibility, but it enables the process to successfully form intricate non-axisymmetric features on the final product [34]. When TPIF technique is implemented, unlike conventional processes, it does not require a high strength die made of steel but can be made of cheaper materials such as aluminum, wood or epoxy resin. This makes TPIF more attractive than SPIF for industrial applications in the rapid manufacturing of complex parts in a low volume batch. However, limited studies are available for the improvement of part accuracy and formability through TPIF process.

Attanasio et al. [35], [36] experimentally studied the effect of process parameters on part accuracy and surface finish in TPIF. By parametric optimization, they were able to reduce geometric deviation of an asymmetric automotive component made of Fe P04 steel material from 1.8 mm to 0.5 mm. Gottmann et al. [37] showed that TPIF process could also be used for the production of cranial implants for human skull with acceptable accuracy. Lu et al. [38] developed a model predictive control (MPC) algorithm for in-process toolpath compensation in TPIF with a partial die and successfully improved the part accuracy of their test case from 3 mm to 0.3 mm. That said, MPC algorithm simply adjusts the toolpath in horizontal and vertical directions for error correction. Such corrections cannot be implemented in TPIF process with a half-die as the tool motion is greatly constrained by its definite shape.

3.2.2 Deformation mechanics and formability analysis

Similar to the studies on part accuracy, most research articles on material formability are more concerned with SPIF process than TPIF. Initially, Filice et al. [39] performed several tests to achieve different straining conditions and determined a forming limit curve (FLC) for SPIF process

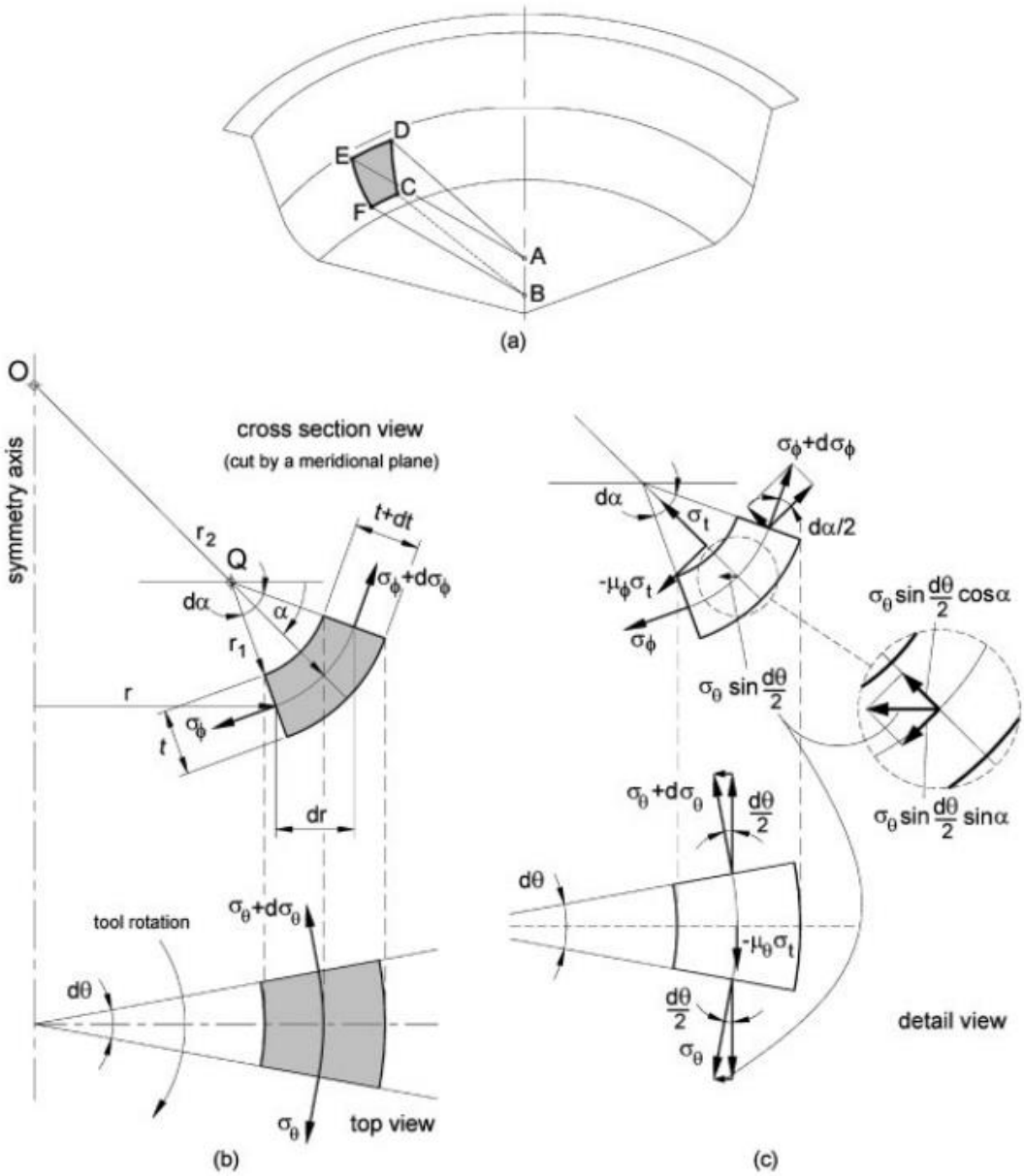

Figure 3.5: Membrane analysis of SPIF process performed by Silva et al. to study its deformation mechanics: (a) schematic of a shell element under the tool; (b) schematic of the shell element in a meridional 2D plane and (c) details of the (b) plot with corresponding stresses in three principle directions (Silva et al. [44], [45])

that looked quite different from the one obtained for traditional processes. Bhattacharya et al. [40] conducted a parametric analysis for the same and noted that the maximum wall angle formed through SPIF increased with the decrease in step size, decrease in tool diameter and increase in initial sheet thickness. Emmens and van den Boogaard [41] performed a comprehensive analysis

on failure mechanism and remarked that excessive through-thickness shear and cyclic strain hardening leads to high material formability. After combining similar studies ([42], [43]), a consensus could be formed that traditional FLC is incapable of describing failure in any ISF process and it must be replaced by fracture forming limit (FFL) diagrams.

Silva et al. [44], [45] presented a closed-form theoretical model to explain fundamentals of SPIF process based on membrane analysis. The proposed model was based on the assumptions that plane strain deformation condition was followed in the forming process and the parts were rotationally symmetric. They developed a failure prediction model using a fracture forming limit diagram instead of FLC and concluded that higher forming limit could be obtained in ISF due to the suppression of necking. Based on the simplified shell element shown in **Figure 3.5**, force equilibrium in three principal directions i.e., meridional, circumferential and tangential were calculated as below equations:

1. Circumferential direction:

$$\sigma_\theta r_1 d\alpha \left(t + \frac{dt}{2}\right) - \mu_\theta \sigma_t r_1 d\alpha \left(r + \frac{dr}{2}\right) d\theta \;=\; (\sigma_\theta + d\sigma_\theta) r_1 d\alpha \left(t + \frac{dt}{2}\right)$$

Neglecting higher order terms: $d\sigma_\theta = -\mu_\theta \sigma_t \frac{r d\theta}{t} \approx -\mu_\theta \sigma_t$ (3.1)

2. Thickness direction:

$$\sigma_t \left(\frac{1}{t} - \frac{\mu_\theta}{2r_2}\right) + \frac{\sigma_\emptyset}{r_1} + \frac{\sigma_\theta}{r_2} = 0 \quad (3.2)$$

Assuming the term $\frac{\mu_\theta}{2r_2}$ is much smaller compared to 1/t ratio, it can be neglected as:

$$\frac{\sigma_t}{t} + \frac{\sigma_\emptyset}{r_1} + \frac{\sigma_\theta}{r_2} = 0 \quad (3.3)$$

3. Meridional direction:

$$\frac{d\sigma_{\emptyset}}{dr} + \frac{\sigma_{\emptyset} - \sigma_{\theta}}{r} + \sigma_t \left(\frac{\mu_{\emptyset}}{t\ sin\alpha} + \frac{\mu_{\theta}}{2r}\right) + \frac{\sigma_{\emptyset}}{t}\frac{dt}{dr} = 0 \tag{3.4}$$

Assuming that r >> t sinα, the equation above can be rewritten as:

$$\frac{d\sigma_{\emptyset}}{dr} + \frac{\sigma_{\emptyset} - \sigma_{\theta}}{r} + \frac{\mu_{\emptyset}\sigma_t}{t\ sin\alpha} + \frac{\sigma_{\emptyset}}{t}\frac{dt}{dr} = 0 \tag{3.5}$$

Later, Silva et al. [46] extended their theoretical framework from SPIF to TPIF process with a partial die to explain the difference between their material formability. According to the performed grid analysis on back of the specimen and observation of crack opening, it was revealed that fracture in TPIF process did not happen after any localized necking and the crack propagated under tensile meridional stresses acting in stretching modes of deformation. Also, experimental analysis of strain loading paths validated the previous assumption that plane strain deformation condition was followed, and FFL must be employed to model material formability in the ISF process as shown in **Figure 3.6** for two different tool diameter settings.

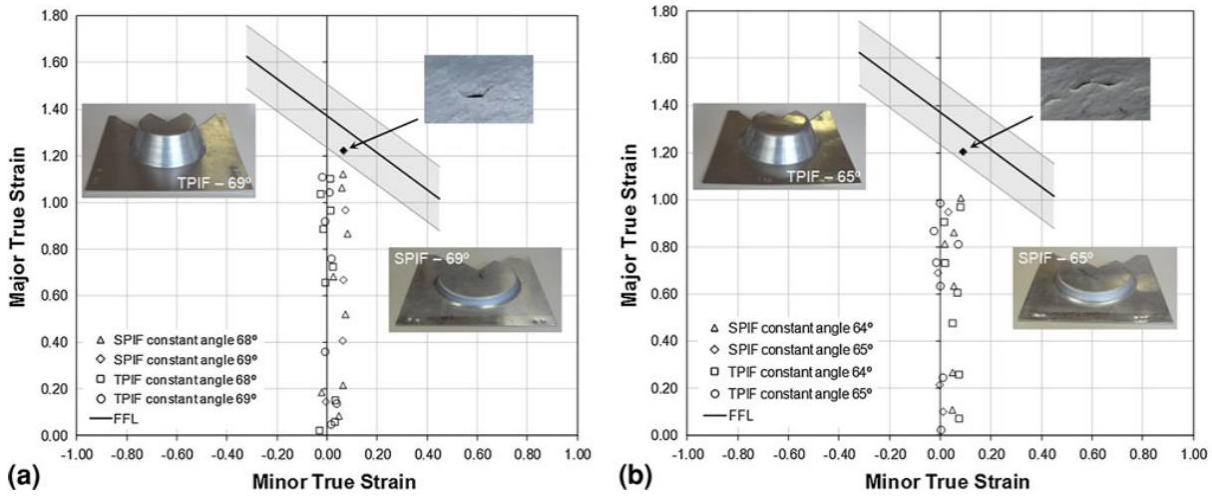

Figure 3.6: Experimentally obtained major and minor strain values for truncated cone parts produced by both SPIF and TPIF process: (a) with a tool diameter of 8 mm and (b) with a tool diameter of 12 mm. Solid marks correspond to the fracture points and hollow marks represent successfully formed points. (Silva et al. [46])

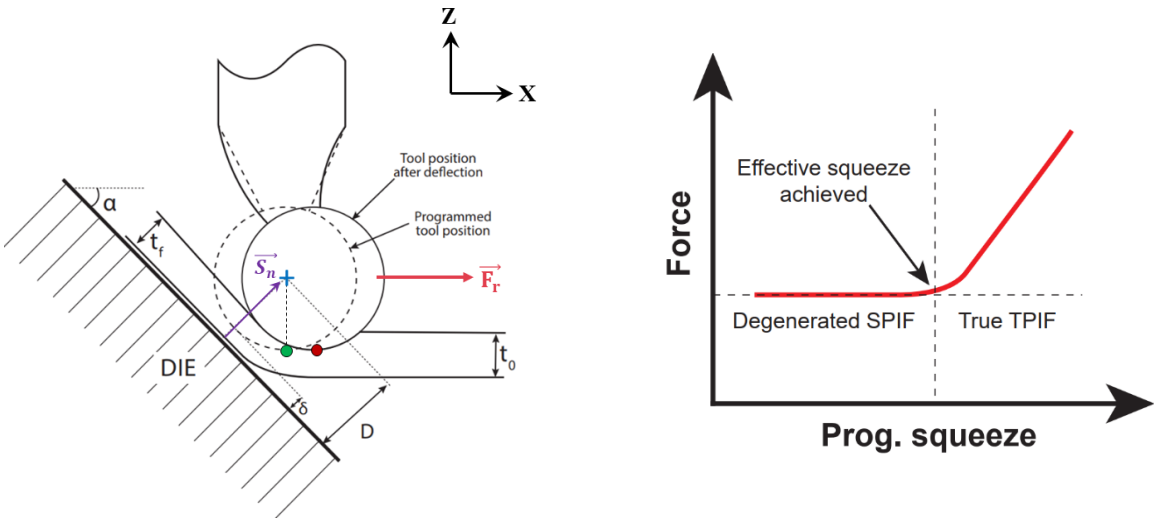

(a) (b)

Figure 3.7: Schematic of (a) squeeze factor in TPIF process. Green and red circles are programmed and actually tool-tip locations; (b) effect of squeeze factor on radial forces

3.3 Toolpath Generation for TPIF Process

While generating toolpath for the ISF process, process parameters required as input other than part geometry are sheet thickness, step size and tool diameter as presented in the section 2.4. But in case of DSIF and TPIF process, an addition parameter called 'material squeeze factor' is also required as an input. It is defined as the amount of sheet thickness locally squeezed between forming tool and the support die. There are two different ways available in literature to describe its value (SF_p) as below:

a. The ratio of distance between the tool and die surface (δ) to that of the Sine law estimated final sheet thickness (t_f) as shown in **Figure 3.7**(a). SF_p value must be in 0 to 1 range to avoid losing contact between die with the sheet [47].

$$SF_p = \delta / t_f \tag{3.6}$$

b. The percent amount of the Sine law estimated final sheet thickness squeezed between the tool and the die surface. Ideally, this value can be anywhere between 0 to 100%. If $SF_p = 0\%$, no

sheet material will be squeezed between the tool and die surface whereas if $SF_p = 100\%$, the tool surface is programmed to touch the die and leave no space for the sheet material [48].

$$SF_p = \left(1 - \frac{\delta}{t_f}\right) * 100 \tag{3.7}$$

The second description of squeeze factor as percent amount presented in Equation (3.7) is used in this thesis to present all the results. For simplicity, final sheet thickness is estimated using Sine law ($t_f = t_0 * \sin(90 - \alpha)$ where t_0 is the initial sheet thickness and α is local wall angle). In toolpath generation process for TPIF, Equation (2.8) from the SPIF toolpath generation is modified as Equation (3.8) to accommodate for the material squeeze:

$$\vec{T} = \vec{S} + \left(TR + t_f * \left[1 - \frac{SF_p}{100}\right]\right) * \overrightarrow{S_n} - TR * \hat{k} \tag{3.8}$$

Initially, Cao et al. [4] introduced the concept of material squeeze factor through DSIF process to consistently maintain the support tool contact with the sheet. They observed that when SF_p value was changed from 0 to 40%, geometric deviation significantly reduced from 46.6% to 28.4%. Later, Malhotra et al. [47] explained this effect using FE analysis concluding that material squeeze stabilized the localized deformation under the tool which led to significant improvement in part geometry.

However, material squeeze that is effectively achieved in experiments is significantly lower than it is programmed in the toolpath due to machine compliance and tool deflection. Radial and tangential forces acting on the tool deviates its tool-tip position from the desired place as shown in **Figure 3.7**(a). As a result, much lower material squeeze is achieved in the experiments that even leads to loss in contact between the sheet and the support die. Loss in sheet – die contact

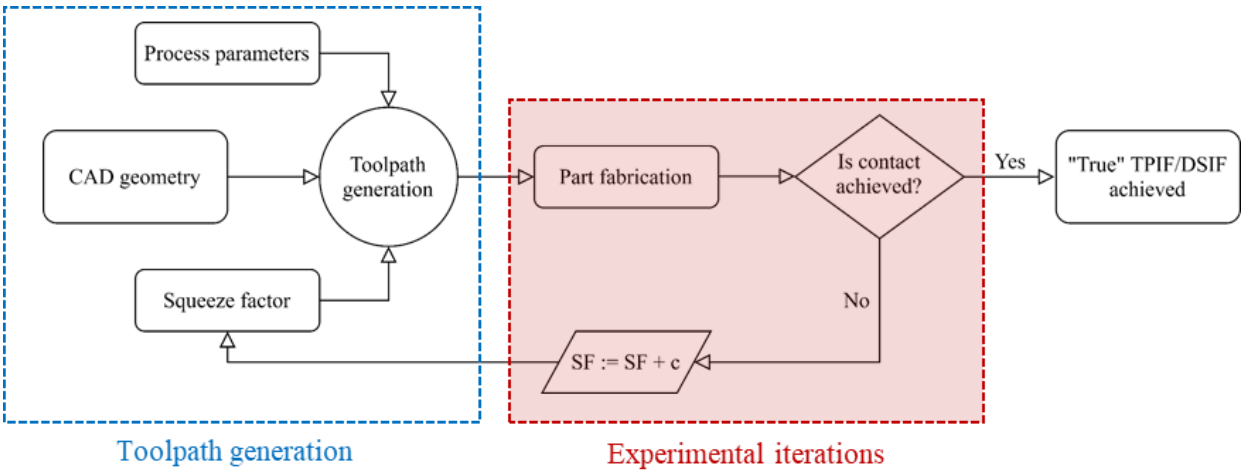

Figure 3.8: Process flow for toolpath generation in TPIF process considering material squeeze factor

implies that the part is not truly formed using TPIF process but rather it is formed using "degenerated SPIF" process. Degenerated SPIF is defined as the ISF process where part fabrication begins with a uniform contact between the sheet and the die surface as intended but later losses this contact where the forming process starts to look more like SPIF with no back support rather than TPIF. This can be easily observed using two different ways: (a) Orange peel effect on die – side part surface implies that no contact between sheet and die is achieved; (b) Axial and radial force value will only increase if the sheet material is getting squeezed between the tool and die surface as shown in **Figure 3.7**(b). No increase in force values implies degenerated SPIF forming process too.

In literature, SF_p value is initially chosen based on experimenter's past experience to generate a part specific TPIF/DSIF toolpath. Once the corresponding part is fabricated, it is determined if the part is formed using "True TPIF" or not. If not, SF_p value is incrementally increased in the toolpath and the above process is repeated until a consistent contact between support tool/die and the metal sheet is achieved. Process flow of this heuristic toolpath generation scheme is presented as a flowchart in **Figure 3.8**.

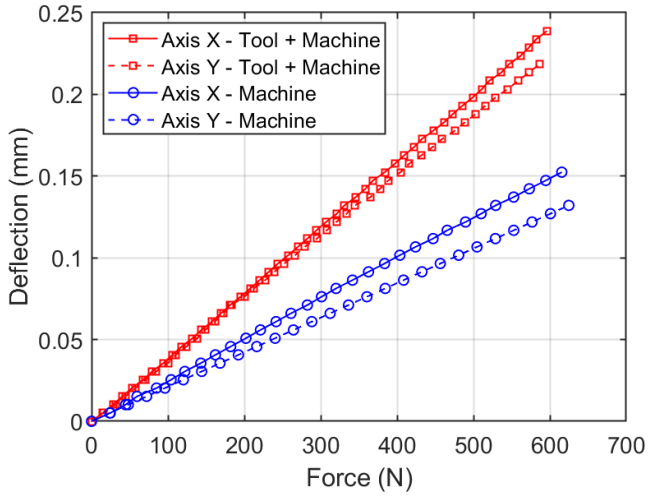

Direction	Compliance coefficient (κ)
Tool + Machine (X – Axis)	4.016E-4
Tool + Machine (Y – Axis)	3.758E-4
Machine (X – Axis)	2.494E-4
Machine (Y – Axis)	2.114E-4

Figure 3.9: Machine and tool compliance measured for the CNC machine used in this study and the compliance coefficient in units = mm/N

Let's take an example of cone 67° part formed using 0% squeeze. The radial force during this experiment is recorded close to 567 N as shown in **Figure 3.16**(a). This will lead to the deflection at tool tip location of approximately 227 microns (567N * 4.06E-4 mm/N, based on compliance measured in **Figure 3.9**). Now based on the Sine law, the final part thickness will be 640 microns (1.64mm * cos 67°). And 30% of this final thickness is under 200 microns which is less than the total deflection. Therefore, even if a material squeeze factor of 30% is applied during experiments, the tool + machine deflection will result in loss of contact between the sheet and the die surface showing that effectively no material squeeze is achieved.

3.4 Programmed vs Effective Material Squeeze Factor

The iterative behavior of toolpath generation scheme results in increased cost and lead time for any part production. These are the two main aspects of a rapid manufacturing process that need to be minimized to make it more viable in automotive or aerospace industries. Therefore, a new modified approach for toolpath generation with minimum to zero experimental iteration is proposed in this section as shown in **Figure 3.10**.

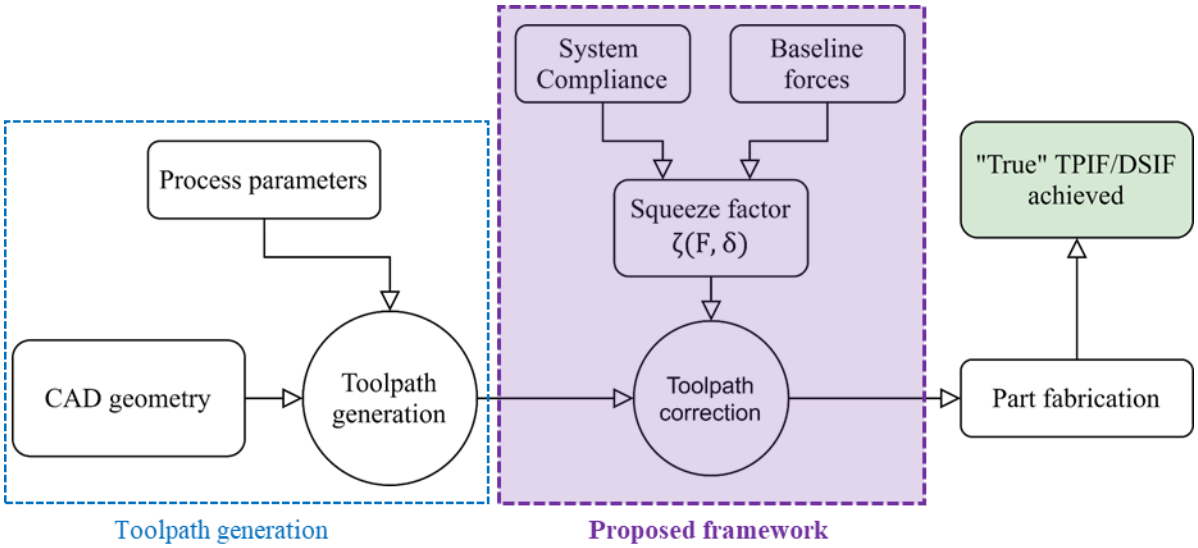

Figure 3.10: Flowchart of proposed toolpath generation strategy for TPIF/DSIF process.

In the modified approach, two new inputs of machine compliance and baseline forming force values are needed to generate a toolpath. Here, machine compliance represents the total deflection of machine axes and tool shank (at the tool – tip location) with respect to a given load vector. For the experimental setup presented in section 3.5, machine compliance is obtained by pressing the tool tip in x and y directions against a solid metal block. At the same time, machine travel is recorded from the CNC controller and the reactionary forces on the tool are measured from the spindle mounted force sensor. It is found to be linearly dependent on the reactionary force values as shown in **Figure 3.9** and Equation 3.9:

$$[\kappa] = \begin{bmatrix} \kappa_1 \\ \kappa_2 \\ 0 \end{bmatrix} \qquad (\kappa_1 = 4.016 * 10^{-4}\ \text{mm/N}\ \text{ and }\ \kappa_2 = 3.749 * 10^{-4}\ mm/N) \quad \text{for the CNC machine used in this study} \tag{3.9}$$

κ_1 and κ_2 are the compliance coefficients in x and y – directions respectively. Compliance obtained along z – direction can be neglected compared to the other two as $\kappa_3 << \kappa_1, \kappa_2$

Baseline forming force is defined as the force required to form the same part geometry using SPIF process. Though these force values can be easily obtained by running the first iteration

of the part, it is more suitable to get them either through finite element model or analytical prediction models readily available in the literature. For example, Aerens et al. [25] performed a comprehensive regression analysis on a wide range of material properties and processing conditions to produce the force prediction in SPIF as Equation (3.10). Bansal et al. [26] proposed a physics based model for the same and validated it for a variety of aluminum alloys and process parameters.

$$F_z = 0.0716\, R_m\, t^{1.57}\, {d_t}^{0.41}\, \Delta h^{0.09}\, \alpha\, \cos\alpha$$
$$F_r = F_z\, \tan\left[\frac{\alpha + \beta - 17.2\, (d_t/10)^{-c}}{2}\right] \tag{3.10}$$

where, F_r and F_z are radial and axial forces in SPIF respectively, R_m is tensile strength, t is sheet thickness, d_t is forming tool diameter, Δh is the scallop height calculated based on step size, α is the part wall angle, β is the scallop groove angle and c is a material dependent parameter.

Once the machine compliance and baseline force values are estimated, a closed – form relation between the programmed and the effective squeeze factor value is calculated using the set of equations from Equations (3.11) to (3.18). Schematic representation of the used variables in these equations is labeled in **Figure 3.11**. Nomenclatures used in the figure for the programmed vs. effective squeeze factor calculations are listed as below:

- β is the distance between actual and programmed tool center
- β' is the projected β distance along the unit normal $\overrightarrow{S_n}$
- D is the programmed distance between tool and die surface along the unit normal $\overrightarrow{S_n}$
- D' is the actual distance between tool and die surface along the unit normal $\overrightarrow{S_n}$
- δ is the minimum programmed distance between tool and die surface

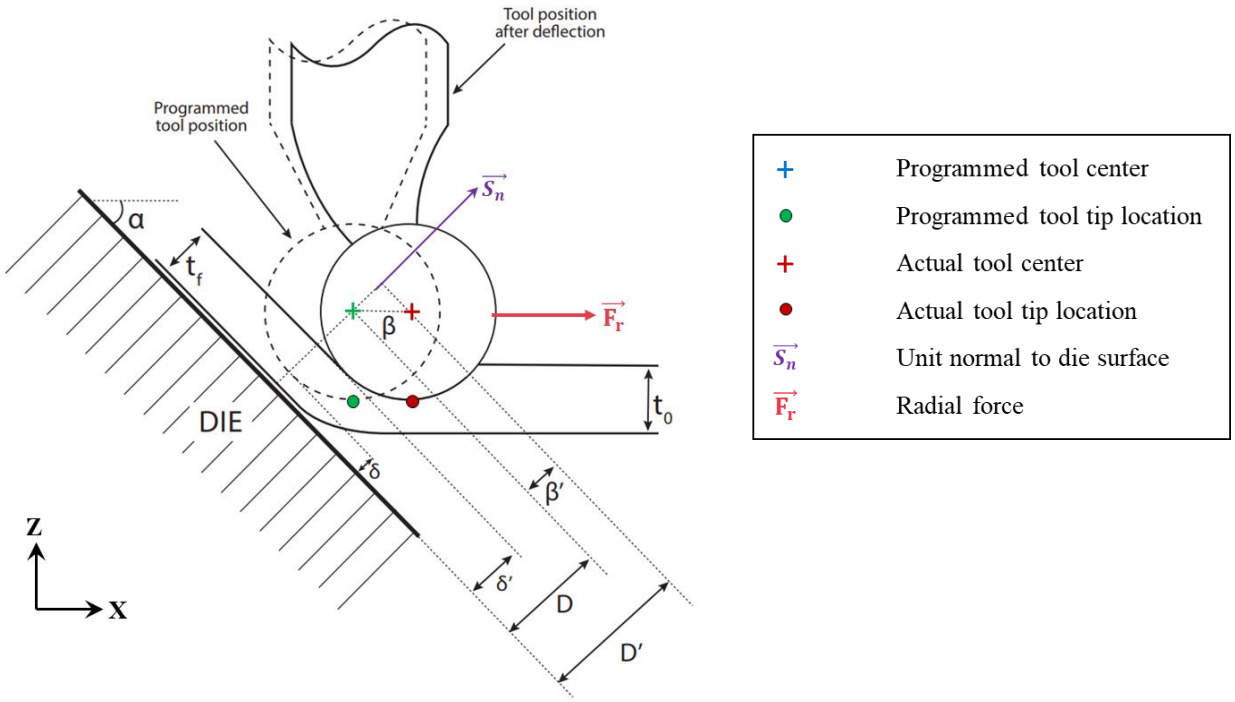

Figure 3.11: Cross-sectional schematic of TPIF part forming process to calculate effective material squeeze factor based on its programmed value

Following is the step-by-step procedure to calculate effective material squeeze value from its squeeze factor values programmed in the toolpath:

1. Using Sine law for part thickness prediction:

$$t_f = t_0 * \cos\alpha \tag{3.11}$$

2. For now, let's define programmed squeeze factor as presented in Equation (3.6), section 3.4:

$$\delta = \mathrm{SF_p} * t_f \tag{3.12}$$

3. From **Figure 3.11**, the values of different length variables can be related as:

$$\beta = \kappa * F_r \tag{3.13}$$

$$D' = \delta + R + \beta * \cos\alpha \tag{3.14}$$

$$\delta' = D' - R = \delta + \beta * \cos\alpha \tag{3.15}$$

4. Similar to Equation (3.12), effective squeeze factor can be presented as:

$$\delta' = \mathrm{SF}_e * t_f \tag{3.16}$$

5. Based on the set of above equations, the relation between effective and programmed squeeze factor can be calculated as:

$$esqz = \frac{\delta'}{t_f} = psqz + \frac{\kappa * F_r * \cos\alpha}{t_f} \tag{3.17}$$

OR, based on the second description of material squeeze factor:

$$\mathrm{SF}_e = \mathrm{SF}_\mathrm{p} - \left(\frac{\kappa * F_r * \cos\alpha}{t_f}\right) * 100 \tag{3.18}$$

The above presented Equation (3.18) is used throughout this study to relate SF_p vs. SF_e values. It must be noted that, effective material squeeze cannot be less than zero ($\mathrm{SF}_\mathrm{e} < 0$). Negative squeeze implies that contact between the sheet surface and local support is lost and the intended TPIF/DSIF process is degenerated to SPIF. Therefore, a high enough SF_p value must be used in the toolpath generation process so that SF_e is always greater than zero.

3.5 Experimental Setup

An experimental setup for TPIF process is custom – built on a Cincinnati HMC 400-EP CNC milling machine as shown in **Figure 3.12**. Initial blank of 1.64 mm thick AL 7075 alloy is cut to the required dimensions in a square shape and clamped to the machine using fasteners and two frames over a female-type die as schematized in **Figure 3.13**(a). A forming tool of 8 mm tip diameter is designed and fabricated with a shank diameter of 19 mm to reduce tool bending during part forming as shown in **Figure 3.13** (b). It is mounted on a 4-component KISTLER dynamometer (RCD Type 9171A) for precises force measurement during the forming process. They are recorded along x, y and z – directions throughout the forming process using a LabVIEW interface to present force evolution for various geometries and process parameters. A conventional out-to-in toolpath is used for experiments in which deformation begins near the periphery of top surface of the sheet and continues in downward direction.

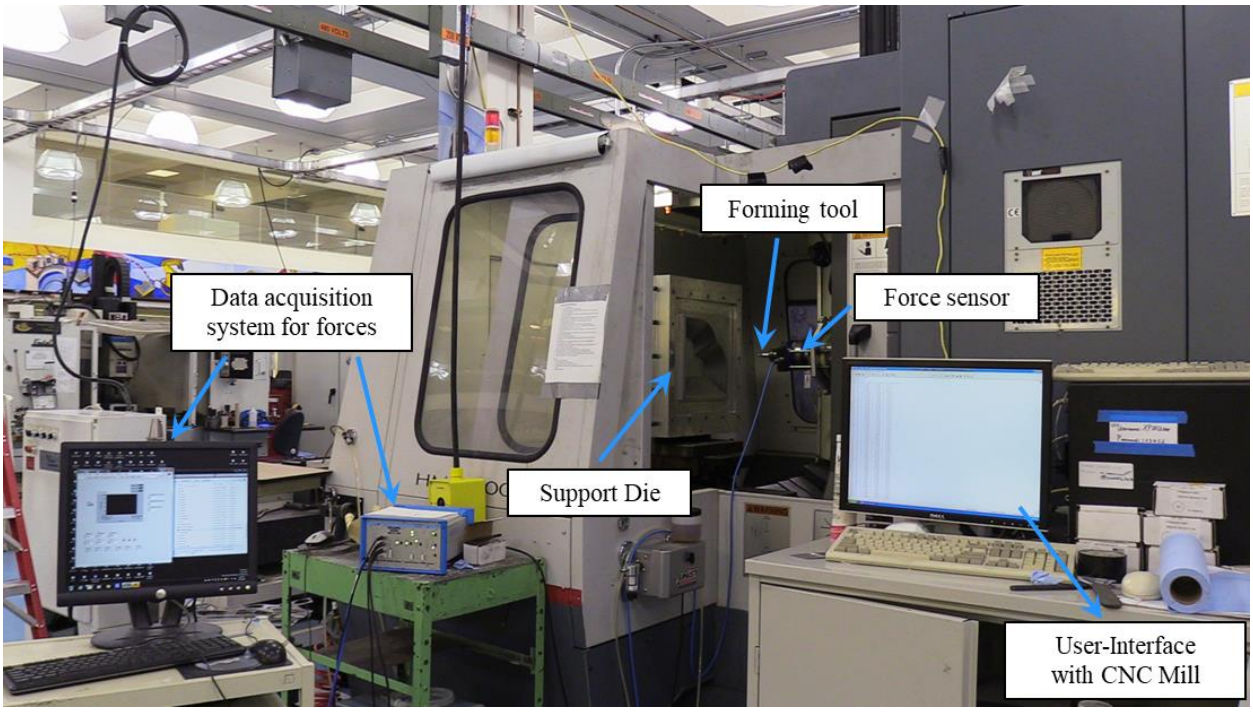

Figure 3.12: Experimental setup for macro-scale TPIF process developed at WuMRC, University of Michigan.

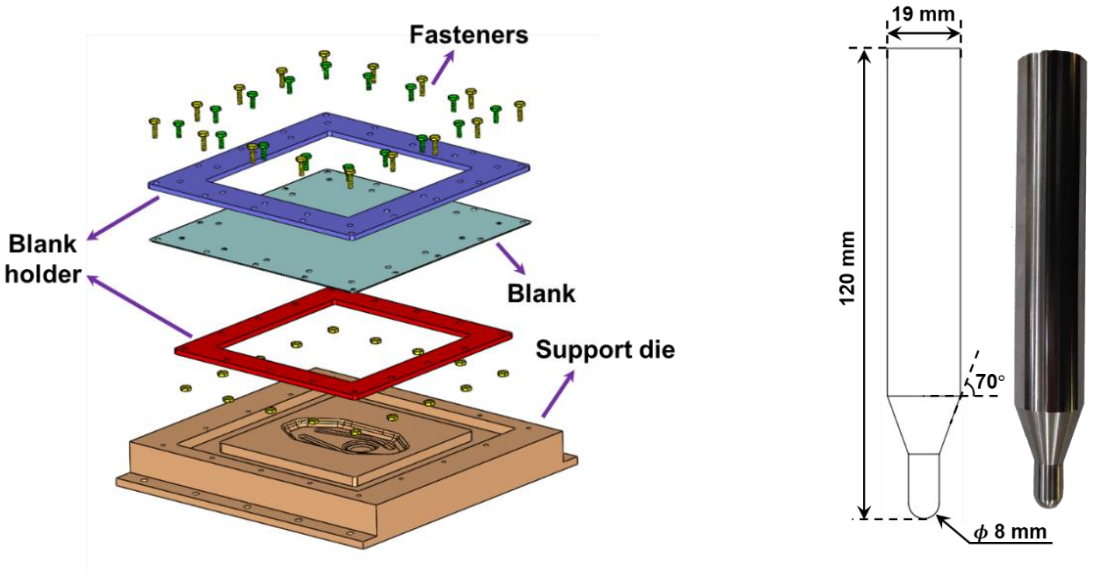

(a) (b)

Figure 3.13: (a) Schematic of the initial blank clamping setup in the CNC machine; (b) tool geometry designed and manufactured for the TPIF experiments with 8 mm tip diameter

Produced parts are laser scanned on both sides using Romer Absolute Arm with Integrated Scanner (Hexagon-7525SI). Obtained point cloud data is reconstructed in the Polyworks software as a polygonal model and exported as a 3D mesh of triangulated surfaces. The best-fit function in the software is used to align the two surfaces together. The function shifts and rotates the scanned points along the three orthogonal axes under constraints of minimized mean square deviation (MSD). Cross sectional profiles for the test cases are extracted from the scanned data and compared to the ideal part geometries shown in **Figure 3.14** to quantify the geometric deviations.

3.6 Results and Discussion

For TPIF experiments of an axisymmetric part, truncated cones are designed with a constant wall angle (45° or 67°) and total depth of 55 mm. Their cross-sectional profiles are presented in **Figure 3.14**(c) and (d). Initial blank size of 250 mm x 250 mm is cut and clamped from its periphery on top of a die. Based on the part geometry, female type half-dies were fabricated outs of aluminum alloy for support on non-tool side of the sheet. For a test case with non-axisymmetric shape, heart shape geometry that contains a combination of flat, concave and convex curved walls is formed on a 450 mm x 450 mm blank size. Part design and its cross-sectional profile is shown in **Figure 3.14**(a) and (b) respectively.

A variety of step sizes and programmed squeeze factor values are used to elucidate their effect on the final part. For truncated cone geometries, a step size of 0.5 mm is used in conjunction

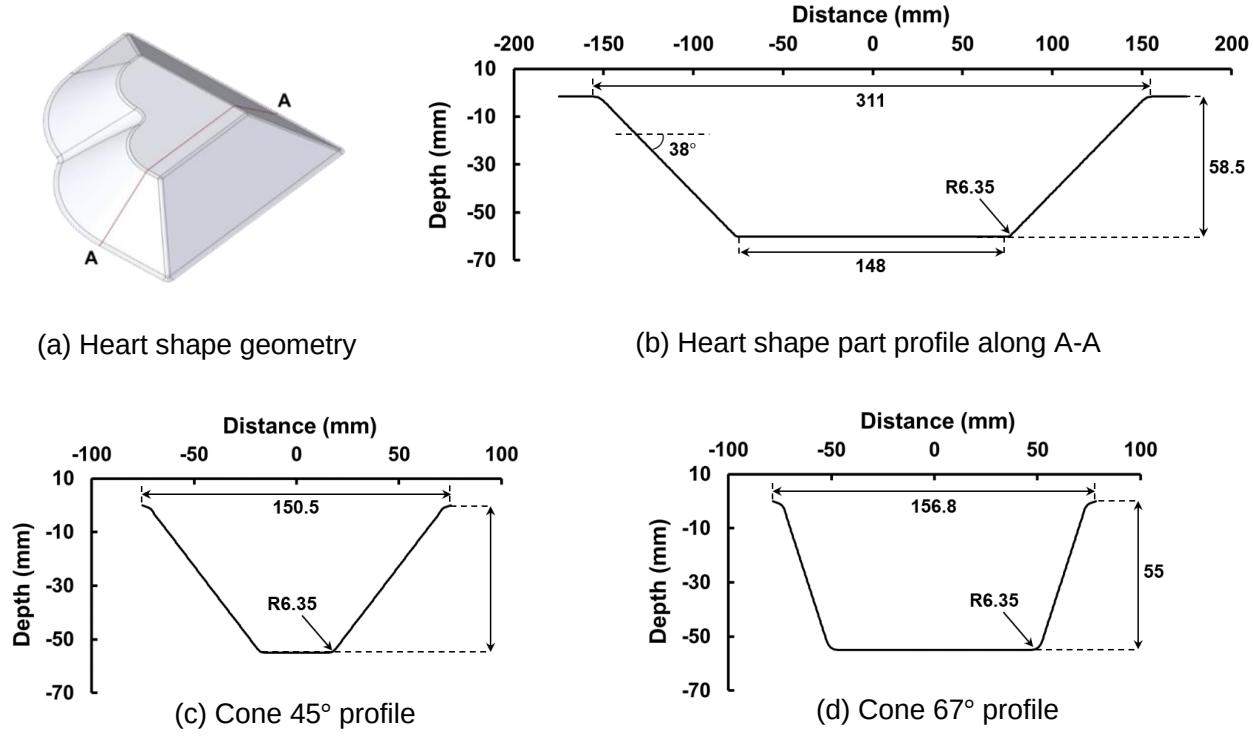

Figure 3.14: (a) Geometry of heart shape part, (b) cross-sectional profile of heart shape part along section A-A, (c) cone 45° profile and (d) cone 67° profile

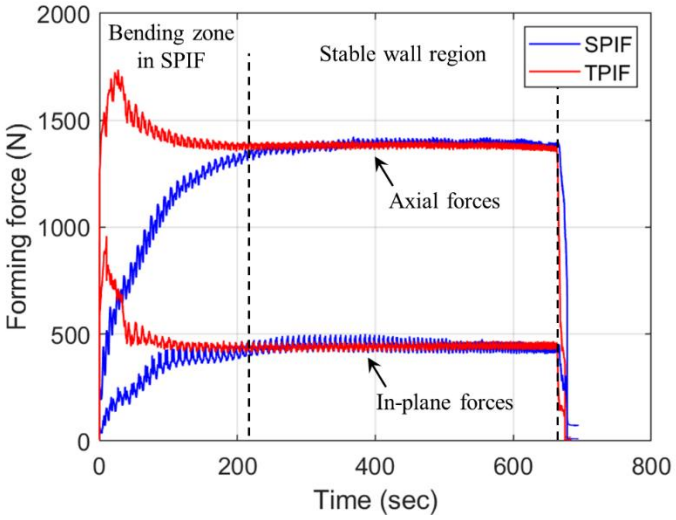

Parameters	Values
Wall angle	45°
Tool diameter	8 mm
Step size	0.5 mm
Feed rate	100 in/min
Sheet t0	1.64 mm
Squeeze	0 %

Figure 3.15: Comparison of forming forces in SPIF and TPIF process for cone 45º part formed using same process parameters and toolpath

with SF_p value varying from 0% to 40%. Whereas in case of heart shape part, step size values from 0.25 mm to 0.75 mm are used in the experiments with 0% to 15% to achieve an optimal part geometry. The feed rate in the forming process is kept constant at 42 mm/sec and molybdenum disulfide in grease form is generously applied on the sheet surface for lubrication. The results obtained through these experiments related to forming forces, geometric accuracy and part formability with respect to different processing conditions are quantified below:

3.6.1 Evolution of forming forces with different squeeze factors

Though parts formed using both SPIF and TPIF process with $SF_p = 0\%$ have same process parameters and toolpaths, they tend to have subtle differences in part geometry and forming force values. TPIFed part has a die support at the bottom that does not allow any unwanted bending near the part opening region similar to previously seen in **Figure 2.13**. Therefore, it leads to an early spike in both in-plane and axial forces as the tool is initially plunging the sheet metal into the die surface. Comparison of these forming forces in case of cone 45º part can be seen in **Figure 3.15**.

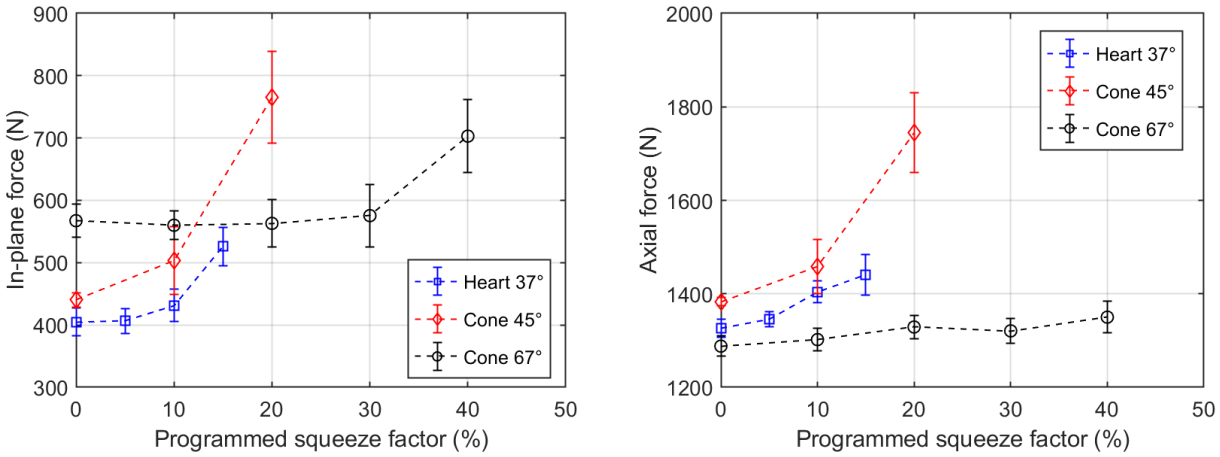

(a) In – plane forces

(b) Axial forces

Figure 3.16: Variation of in-plane and axial forming forces with increase in programmed squeeze factor value for truncated cone and heart shape geometry

Once the stable wall angle is achieved, the force values converge and saturate at a constant value. Further in this chapter, average force values in this stable region are reported with their deviation for easier and better comparison.

Test samples with previously mentioned three geometries are fabricated using TPIF process with varying squeeze factors to analyze its effect on forming force values. The list of parameters for all the tests is given in **Table 3.1**. Forming force for each test case is resolved into in-plane and axial directions and plotted with respect to programmed squeeze factor as shown in **Figure 3.16**(a) and (b) respectively. Here, in-plane forces are the resultant of force values in x and y directions whereas axial forces are measured along the z direction (axis of symmetry).

Based on the reported strain history analysis [49] during ISF process, principal strain value in circumferential direction is very low compared to the thickness and meridional directions. Therefore, it is safe to assume that tangential forces can be neglected in comparison with radial and axial forces; and radial force can be approximately assumed to be equal to in-plane force.

Table 3.1: List of step sizes and programmed squeeze factors used to study its effect on forming forces

Part geometry	Cone 45º	Cone 67º	Heart shape
Step size	0.5 mm	0.5 mm	0.63 mm
Squeeze factor	0, 10, 20%	0, 10, 20, 30, 40%	0, 5, 10, 15%

It is evident from **Figure 3.16**(a) that radial forces initially remain constant with programmed squeeze factor, indicating no effective squeeze. But it sharply increases after a threshold where effective material squeeze is achieved as previously hypothesized in section 3.4. Effective squeeze factor values for all the geometries and parameters are calculated using the Equation (3.18) as listed in **Table 3.2**. Machine compliance with respect to reactionary force is different in x and y directions leading to different effective squeeze on the final part. Therefore, two SF_e are reported in the table as (SF_e along x – axis, SF_e along y – axis). Note that, forming force values obtained through experiments are used here for robust demonstration of the proposed methodology and avoid any prediction errors transferring from FEA or analytical force prediction models.

Table 3.2: Effective squeeze factor values calculated for different programmed squeeze factors and geometries based on experimentally obtained forces.

Part geometries					
Cone 45°		**Cone 67°**		**Heart shape**	
SF_p	**SF_e**	**SF_p**	**SF_e**	**SF_p**	**SF_e**
0	(-10.7, -10.1)	0	(-32.7, -30.6)	0	(-7.7, -7.2)
10	(-2.8, -2.0)	20	(-12.5, -10.3)	5	(-2.7, -2.3)
20	(1.2, 2.5)	30	(-3.2, -1.0)	10	(1.8, 2.3)
		40	(1.3, 2,4)	15	(4.9, 5.6)

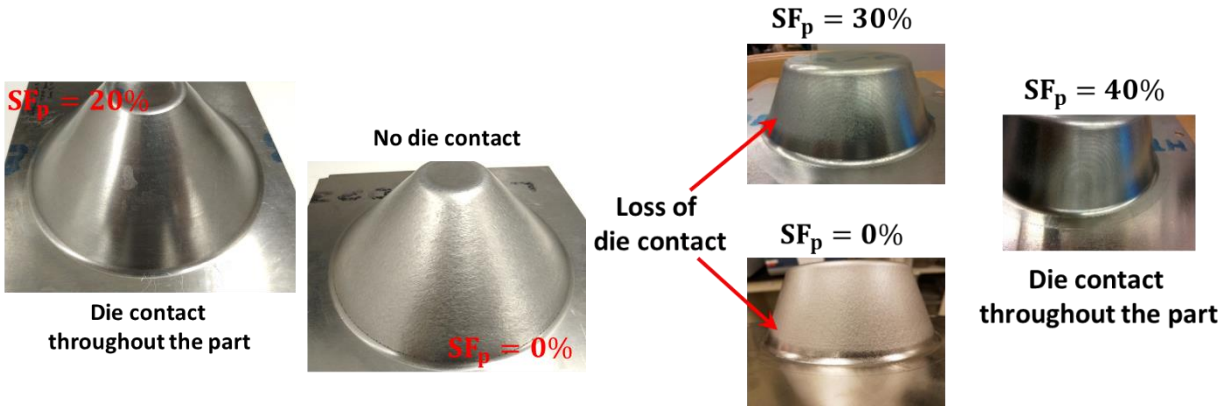

(a) Cone 45º (b) Cone 67º

Figure 3.17: Die - side surface pictures of truncated conical geometry parts formed using TPIF process with different SF_e values

In case of heart shape, $SF_p = 0\%$ translates to $SF_e \approx 7\%$ whereas for cone 67°, $SF_p = 0\%$ translates to $SF_e \approx 32\%$. Negative effective squeeze results in the loss of contact between specimen and support die after top fillet region as shown in **Figure 3.17**. Therefore, the corresponding parts must be considered as formed through degenerated SPIF process rather than TPIF. SF_e calculations above infer that depending on the part geometry, toolpaths must be designed with part specific programmed squeeze factor to achieve positive material squeeze ($SF_e > 0$). SF_p must be above 7-8% in heart shape and 30-33% in case of cone 67° parts.

To validate the above hypothesis, heart shape and cone 67° parts are fabricated using toolpaths for both slightly lower and higher than these calculated SF_e transition point and checked for sharp increase in force values when effective material squeeze is achieved. In heart shape, the radial force values for both $SF_p = 0\%$ and 5% are approximately same but later increase by 6.6% and 30% for $SF_p = 10\%$ and 15%, respectively. In cone 67°, radial force remains constant for $SF_p = 0 - 30\%$ but significantly increases by 23.9% for $SF_p = 40\%$ where positive material squeeze is successfully achieved. It needs to be recognized that though very high programmed

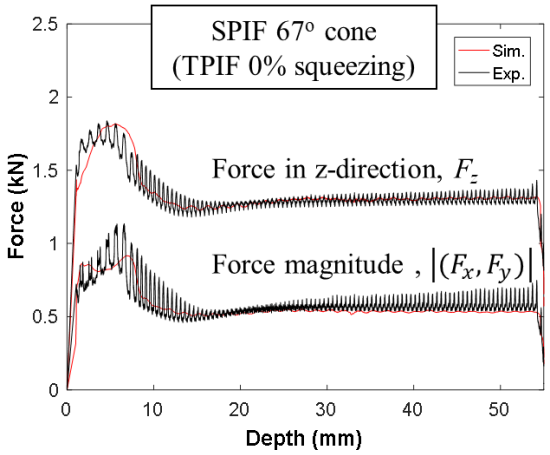

(a) Formed and simulated with 0% programmed squeeze factor

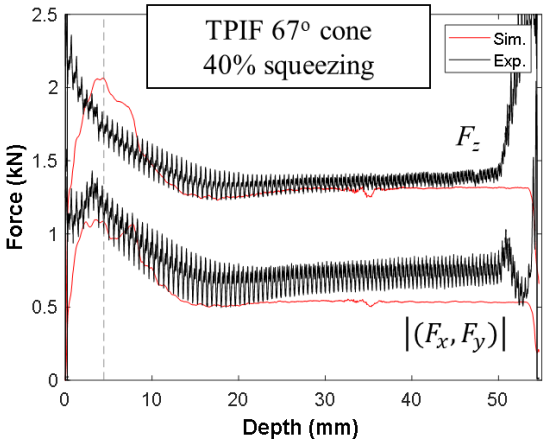

(b) Formed with $SF_p = 40\%$ and simulated with $SF_p = 2.3\%$

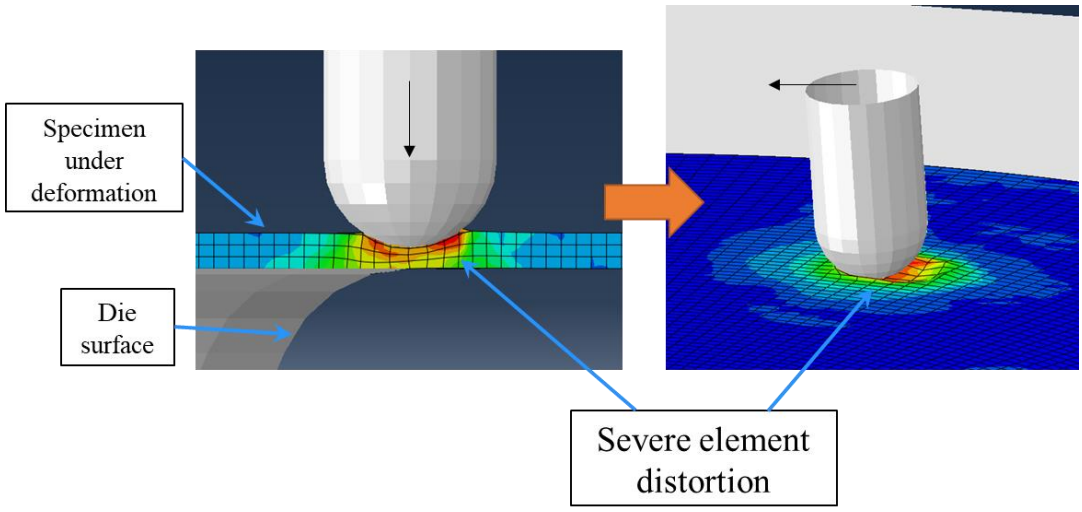

(c) Simulation failed when run with a toolpath of $SF_p = 40\%$

Figure 3.18: Effect of using programmed and effective material squeeze factor in FE analysis

squeeze factor is used in experiments, only 2-3% of effective material squeeze is obtained, which is enough to increase forming forces by more than 30%.

A similar study was conducted by fabricating cone 45° using the same processing conditions through TPIF. The transition point to attain positive material squeeze was estimated at $SF_p \approx 12\%$ using experimental force value obtained for $SF_p = 0\%$. This discrepancy due to

system compliance in TPIF and DSIF process can significantly influence the outcome of finite element simulations.

In collaboration with Prof. Pourboghrat group – The Ohio State University, a finite element model for cone 67° is developed to understand the effect of squeeze factor on the geometry and force prediction results. Further details of the model, boundary conditions and its material properties are available in [50]. When a FE simulation with $SF_p = 0\%$ toolpath is performed, the reactionary forces on the tool are compared with the corresponding experimental values as shown in **Figure 3.18**(a). The predicted results are in very good agreement with the experimental values in both axial and radial directions. However, when the same model is run with a $SF_p = 40\%$ toolpath, error due to excessive element distortion and high hourglassing effect is obtained as shown in **Figure 3.18**(c). This occurred because the toolpath input to the FE model was not corrected for the tool deflection and machine compliance. To mimic the experimental conditions in the simulation, toolpath should be used with effective material squeeze. Therefore, the same simulation was run with an adjusted toolpath of $SF_p = 2.3\%$ that is equal to its effective squeeze factor value as calculated in **Table 3.2**. This significantly improves the simulation convergence, and the FE results match very closely with the experimental observations as shown in **Figure 3.18**(b). Therefore, ISF process must be simulated with effective squeeze factor rather than its programmed value for correct representation of material deformation state obtained in corresponding experimental conditions.

3.6.2 Part geometric accuracy in TPIF process

Parts fabricated through ISF tend to have inferior geometric accuracy compared to traditional sheet forming processes, such as deep drawing and hydroforming, due to local sheet springback and elastic tool deflection. In this section, the effect of material squeeze on part

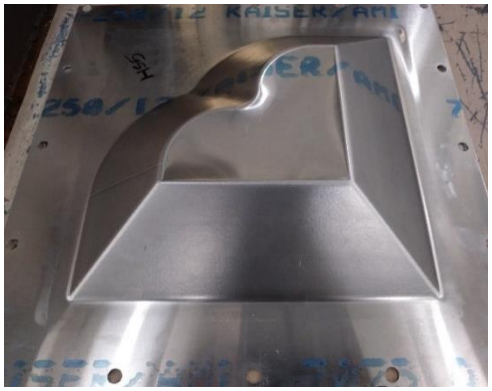

(a) Heart shape formed part

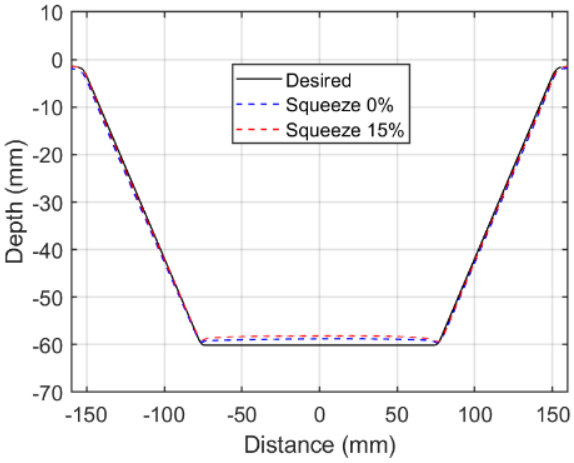

(b) Cross-sectional profile comparison

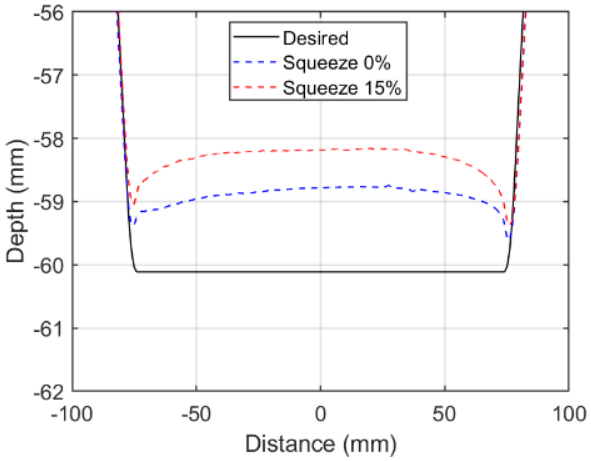

(c) Zoomed view of (b) at part bottom

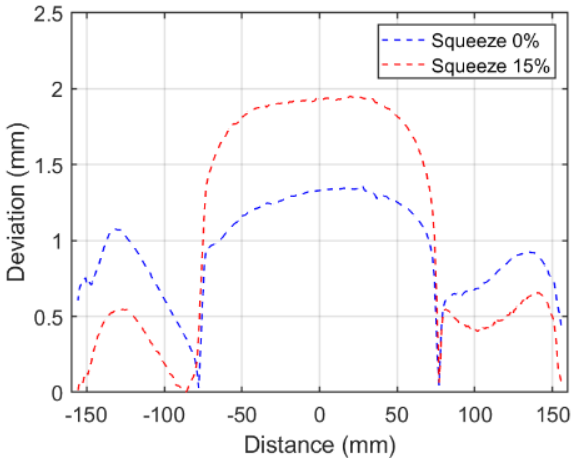

(d) Deviation of experimental and designed profile

Figure 3.19: Comparison of experimentally obtained and designed cross-sectional profiles of heart shape part with two different squeeze factors

accuracy is investigated by fabricating heart shape and cone 67° parts using various squeeze factors. Process parameters are set at step size = 0.63 mm and feed rate = 100 inch/min for heart shape whereas cone 67° are fabricated with step size = 0.5 mm and feed rate = 25 inch/min. Produced parts are compared with their CAD models along different cross sections and overall 3D profile shown in **Figure 3.14**.

Experimental results obtained for different geometries show strong influence of material squeeze on part's accuracy in both the wall region and undeformed base. Compressive stress state

(a) Cone 67º formed part

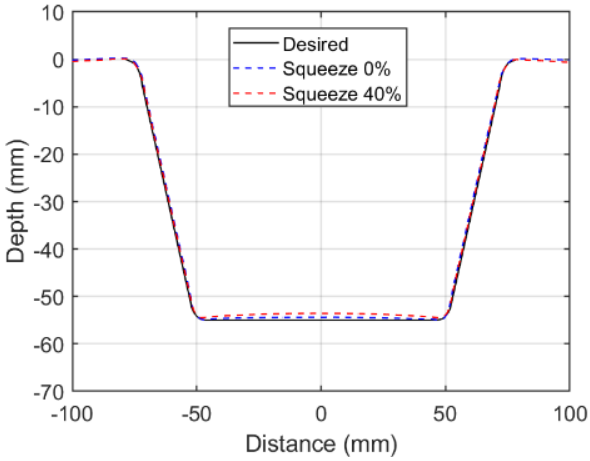

(b) Cross-sectional profile comparison

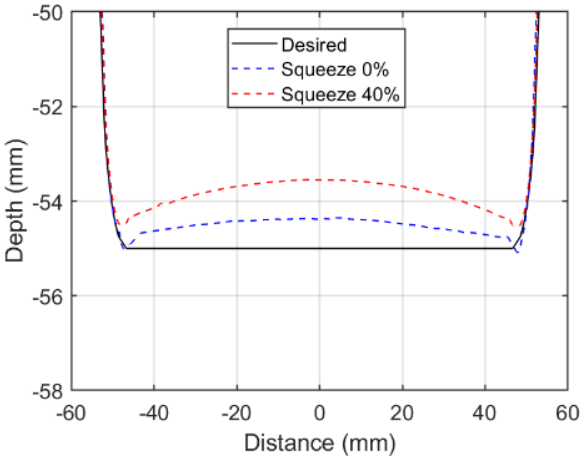

(c) Zoomed view of (b) at part bottom

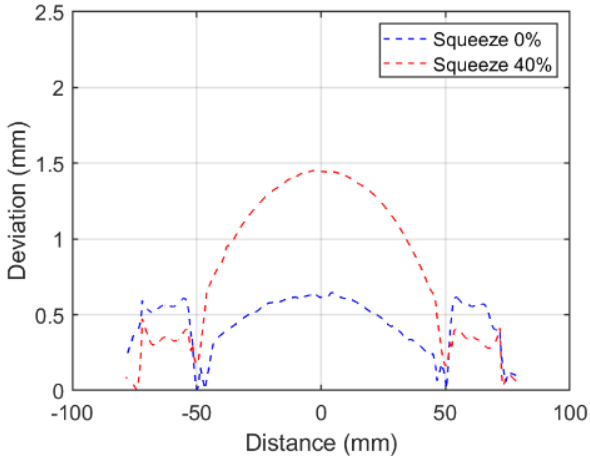

(d) Deviation of experimental and designed profile

Figure 3.20: Comparison of experimentally obtained and designed cross-sectional profiles of cone 67º with two different squeeze factors

introduced by material squeeze tends to reduce sheet springback and eventually improves accuracy in the inclined wall region. However, material squeeze also increases the bulge height in the part's base region due to material accumulation and flattened tool asperities from the wall region.

Cross sectional profile for heart shape is taken at an offset of 69 mm from its center to measure accuracy along straight walled region. It is observed to have maximum profile deviation of 1.07 mm in the inclined wall region when formed with $SF_p = 0\%$ and it significantly reduced

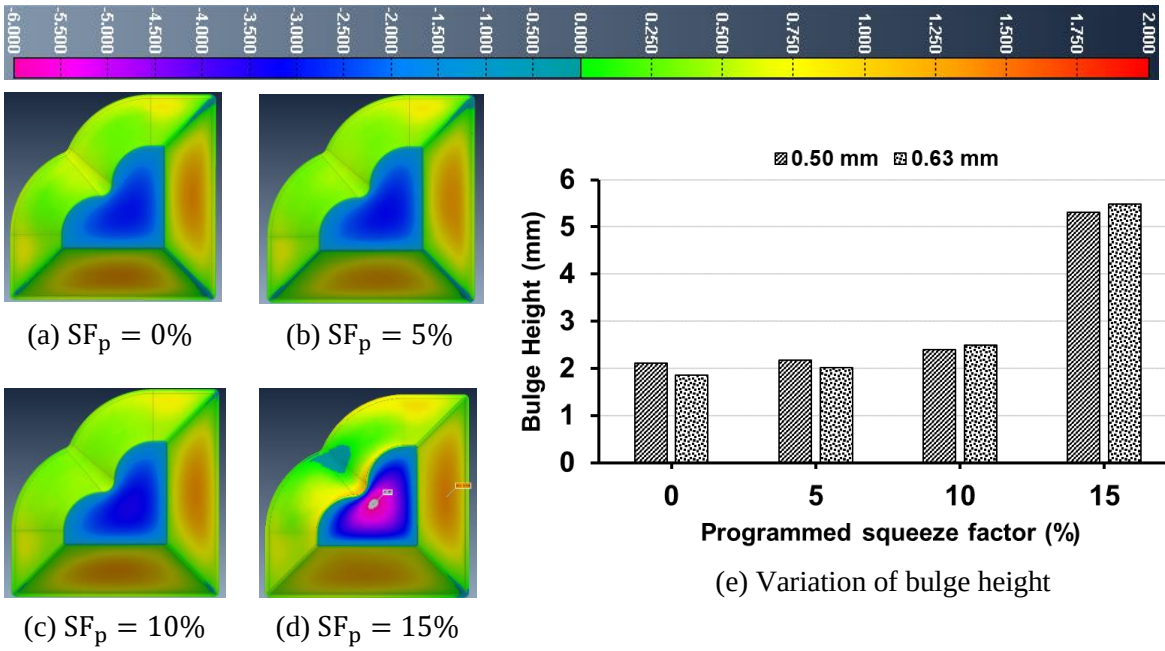

(a) $SF_p = 0\%$ (b) $SF_p = 5\%$

(c) $SF_p = 10\%$ (d) $SF_p = 15\%$

(e) Variation of bulge height

Figure 3.21: 3D geometric accuracy of heart shape part forming using Δz = 0.63 mm and (a) $SF_p = 0\%$, (b) $SF_p = 5\%$, (c) $SF_p = 10\%$, (d) $SF_p = 15\%$ and (e) variation of bulge height for Δz = 0.5 mm and Δz = 0.63 mm with different programmed squeeze factors.

to 0.65 mm when formed with $SF_p = 15\%$ as compared in **Figure 3.19**. However, bulge height along the cross section increases to 1.93 mm in $SF_p = 15\%$ compared to 1.34 mm obtained in $SF_p = 0\%$ which reduces accuracy in base region. Similar result is observed with accuracy measurements of cone 67°. Maximum profile deviation reduces to 0.39 mm when it is produced using $SF_p = 40\%$ compared to 0.61 mm obtained with $SF_p = 0\%$ and bulge height increases to 1.45 mm from 0.64 mm for respective programmed squeeze factors as shown in **Figure 3.20**.

Besides, maximum bulge height in heart shape is observed close to its center through comparison of 3D geometric deviation. **Figure 3.21** shows that bulge for both $SF_p = 0\%$ and $SF_p = 5\%$ remains similar but significantly increases for $SF_p = 15\%$. When small effective material squeeze is achieved at $SF_p = 10\%$, slight increase in bulge height is observed for both heart shapes formed using 0.5 mm and 0.63 mm step sizes. On further increasing the material squeeze to $SF_p = 15\%$, bulge height for both step sizes significantly increase by more than 120%.

Therefore, a trade-off between part accuracy along wall region and base region needs to be identified depending on application to keep overall accuracy acceptable.

3.6.3 Benchmarking multi-stage ISF against hydroforming process

Even when good geometric accuracy is achieved in incrementally formed parts, the presence of any bulge at the bottom of the part could make TPIF process less attractive compared to other sheet metal forming process such as hydroforming. Therefore, to overcome this drawback, a hybrid toolpath generation strategy is proposed as a combination of both out-to-in and in-to-out tool movement. In stage 1, a toolpath is designed with out-to-in strategy keeping a small clearance between part and die surface. This toolpath avoids any undesired material squeezing and fabricates the part with near required shape. In subsequent stage, a toolpath with in-to-out strategy is designed to mildly squeeze the specimen between tool and die surface as represented in **Figure 3.22**. This forming pass pushes the specimen material against die surface and flattens out all asperities produced in previous pass.

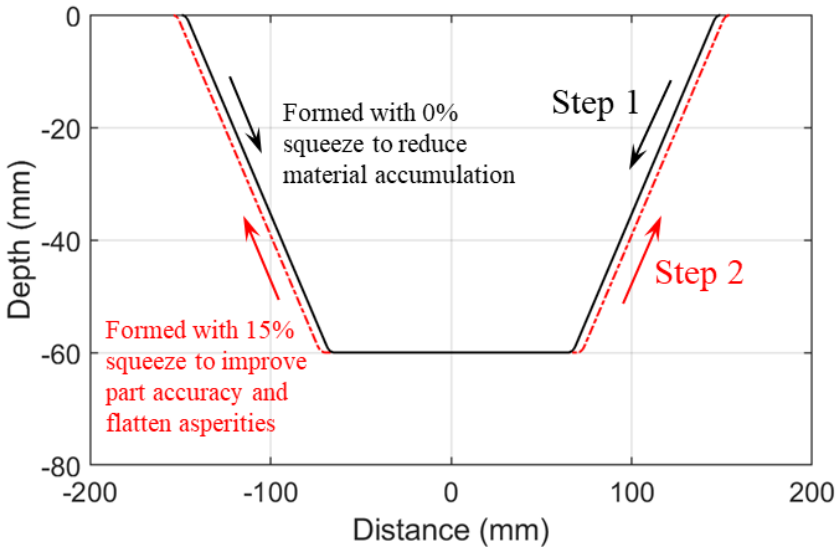

Figure 3.22: Multi-stage forming strategy for ISF process to reduce bulge formation and improve geometric accuracy

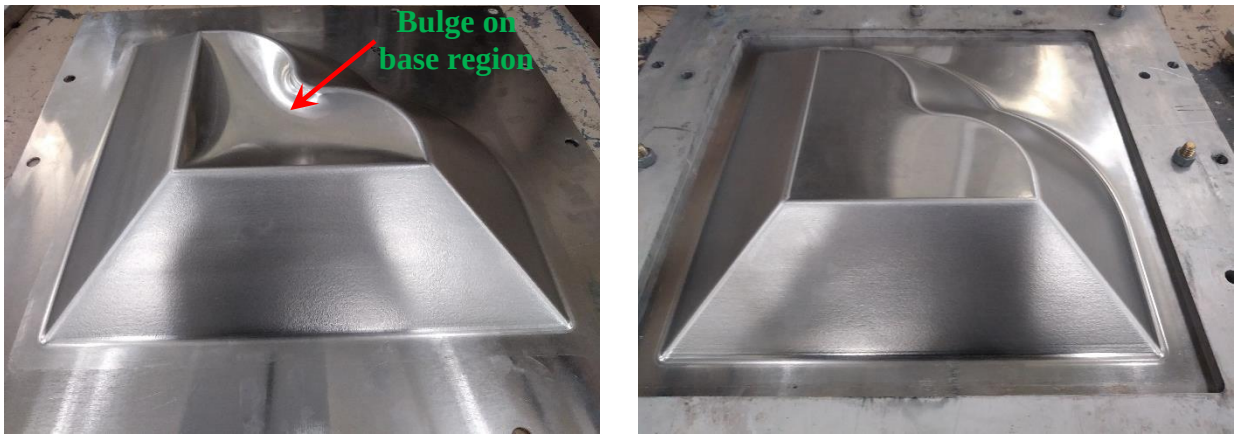

(a) (b)

Figure 3.23: Heart shaped parts fabricated using (a) TPIF process and (b) Hybrid-TPIF process

Primarily, the presented hybrid toolpath strategy redistributes surface material throughout part geometry and avoids material accumulation in front of the tool. Therefore, it helps in eliminating the formation of any bulged feature in part's base as compared in **Figure 3.23**. To further strengthen the benefits of multi-stage TPIF process, geometric accuracy of the parts fabricated by three different processes as: (a) TPIF; (b) Multi-stage TPIF and (c) Hydro-forming; are compared to the designed heart shape geometry. Process parameters used for these TPIF and multi-stage TPIF process are:

- TPIF : step size = 0.5 mm; $SF_p = 15\%$
- Multi-stage TPIF : step size = 0.5 mm; SF_p [stage 1] $= 0\%$, SF_p [stage 2] $= 15\%$

Geometric accuracy for all three parts is individually color plotted in **Figure 3.24**. Deviation of approximately 5 mm when compared to the ideal geometry can be observed at the bottom of the TPIFed part due to bulge whereas it is less than 1 mm in the wall region. In case of the multi-stage TPIFed part, bulge at the bottom is significantly reduced to less than 2 mm with less than 1 mm deviation in wall region too. However, it is difficult to quantify the geometric accuracy distribution solely based on its 3D color plot. Therefore, a gaussian distribution of the

part accuracy is compared for all three parts as shown in **Figure 3.25**. It is evident from error distribution (**Figure 3.25**(a)) that geometric accuracy in hybrid-TPIF is close to hydroformed part and far better than conventional TPIF part.

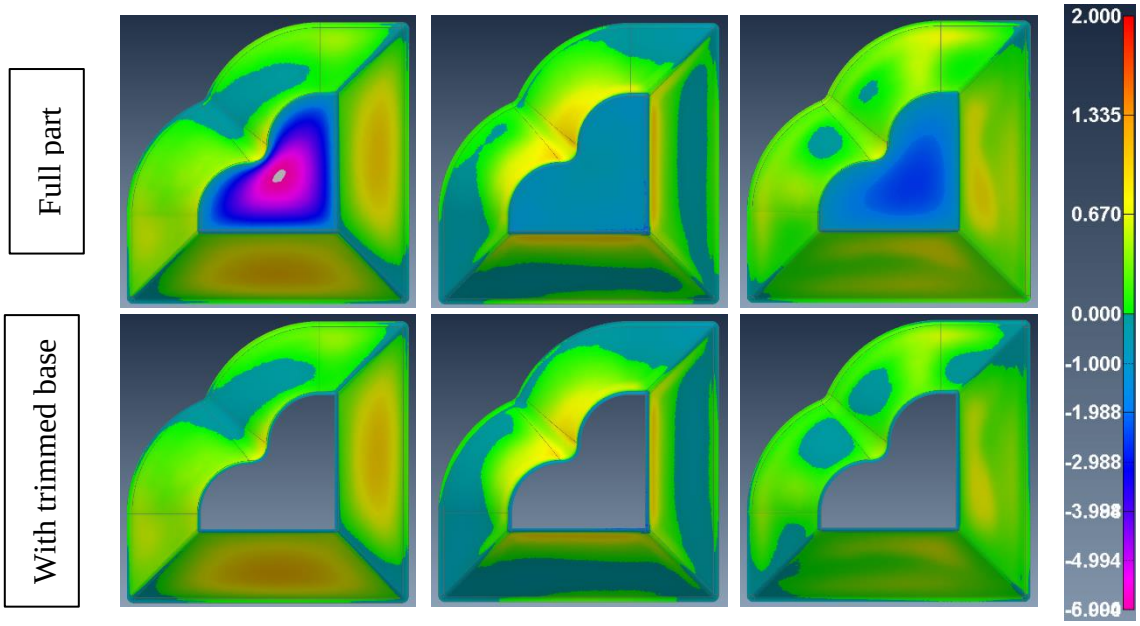

(a) TPIF (b) Hydro-forming (c) Multi-stage TPIF

Figure 3.24: Geometric deviation of heart shape parts formed using (a) TPIF process; (b) hydroforming and (c) multi-stage TPIF process

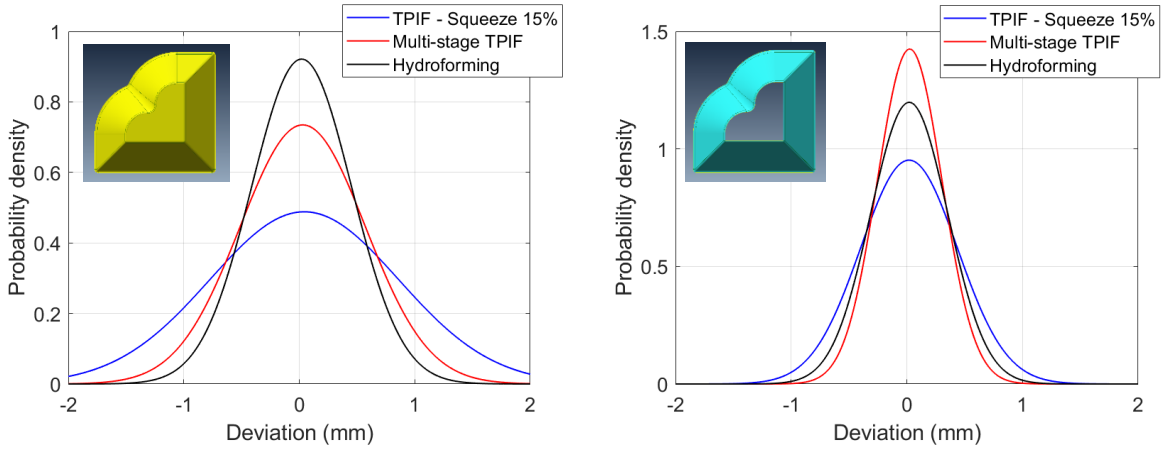

(a) Full part (b) Part with trimmed base

Figure 3.25: Distribution of geometry accuracy of heart shape parts produced using TPIF, multi-stage TPIF and hydroforming process

If the base region is neglected, conventional TPIF and hydroformed parts have similar geometric accuracy based on error distribution plotted in **Figure 3.25**(b). But in this case, part fabricated using hybrid-TPIF has significantly better accuracy than other two parts. This makes hybrid-TPIF process much more desirable in industrial applications than hydroforming process when small batch production is required.

3.6.4 Material and part formability

Though material forming limit obtained in incremental forming is much higher compared to that in traditional forming processes, it can be significantly influenced by process parameters such as step size, tool diameter and sheet thickness. Generally, formability in ISF is considered insensitive to strain rate due to relatively low deformation rate. But experimental investigation conducted on cone 67° through TPIF indicates considerable effect of feed rate and effective squeeze on material forming limit. A set of experiments is performed fabricating cone 67° with different feed rates of 25, 50, 75 and 100 inch/min and $SF_p = 0, 10, 20, 30$ and 40% keeping step size constant at 0.5 mm.

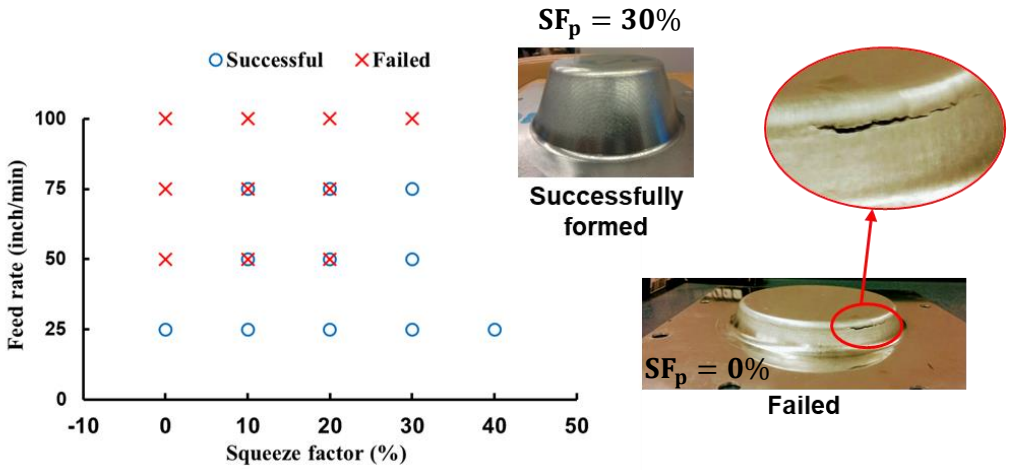

Figure 3.26: Effect of programmed squeeze factor and feed rate on formability of cone 67°

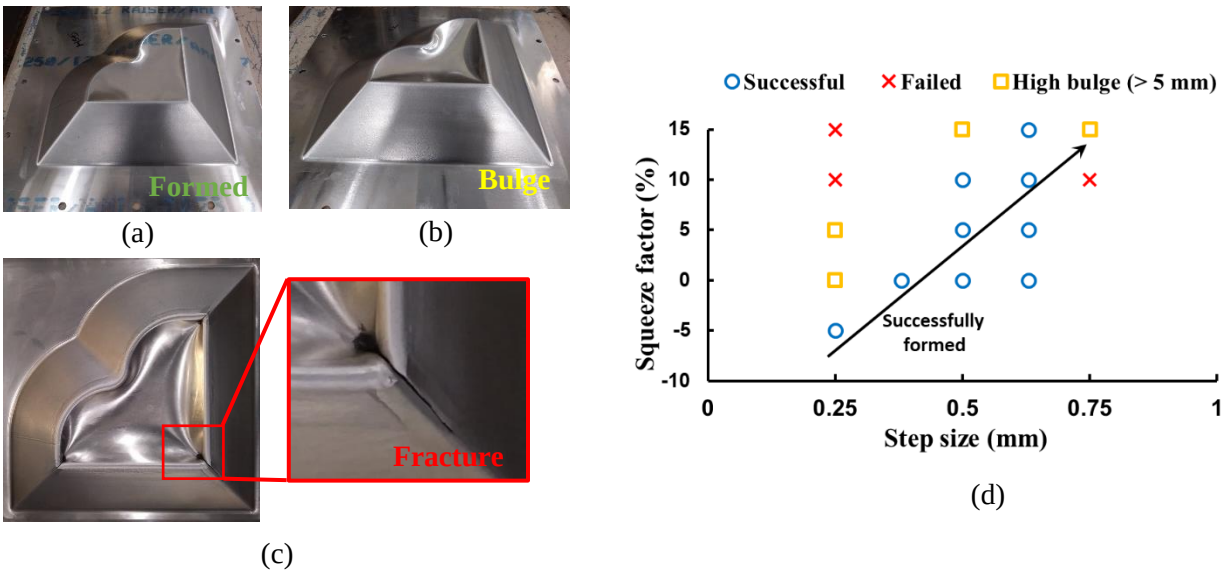

Figure 3.27: Formability analysis of heart shape part with different process parameters as: (a) $\Delta z = 0.5$ mm and $SF_p = 0\%$; (b) $\Delta z = 0.63$ mm and $SF_p = 15\%$; (a) $\Delta z = 0.75$ mm and $SF_p = 10\%$; and (d) effect of SF_p and step size

For $SF_p = 0\%$, parts are successfully formed with the feed rate of 25 inch/min whereas it consistently failed for higher feed rate values ranging from 50-100 inch/min as presented in **Figure 3.26**. On increasing the squeeze factor to 30% where partial contact is observed between sheet and die, experimental results indicate successful part formability at even higher feed rates of 50 and 75 inch/min. This effect can be attributed to the compressive stress state attained by squeezing the material under deformation between two rigid surfaces. It helps suppress the neck formation in thinning region and delay material instability. For $SF_p = 10\%$ and 20%, formability of cone 67° obtained with feed rate of 25 and 100 inch/min remained consistent for all three trials whereas inconsistency in part formability is observed for feed rate of 50-75 inch/min. One of the three parts is successfully formed with these feed rate settings while two others developed fracture along tool motion direction in thinning region slightly below the part opening. Further experimental and numerical investigations need to be conducted to analyze the inconsistent formability behavior. Note that this difference in material formability with respect to feed rate could also be hypothesized to be a cause of machine kinetics and high speed. A vibrometer based frequency analysis of the

tool spindle at different speeds can provide a better explanation. Therefore, further experimental investigation is needed to definitively conclude that incrementally formed parts have strain-rate sensitive formability.

Failure mode in ISF is generally governed by ductile fracture with no experimental evidence of necking. When fabricating parts with higher wall angle, excessive material thinning leads to ductile fracture under the tool and along circumferential direction as highlighted in **Figure 3.26**. However, in case of heart shape, part failure is observed in a corner due to excess bulge in its base as shown in **Figure 3.27**(c). As the bulge height keeps increasing, it induces an additional tensile force along circumferential direction on the corner and results in material failure. Though it can be believed that it is still a ductile mode of failure, fractography needs to be performed to identify the failure mode by analyzing the surface of fractured cross-section.

As the fracture in heart shape appears to be governed by the amount of bulge on its base, further experimental investigation was conducted to understand the influence of step size and squeeze factor on its height. Processing conditions used to fabricate the parts are set at: (a) Δz = 0.25 to 0.75 mm, (b) F = 100 inch/min and (c) SF_p = -5 to 15%. The produced parts are classified into three sections: (a) successfully formed with minor bulge, (b) successfully formed with large bulge and (c) failed at the corner ribs. Results demonstrate that the bulge height is a combined function of both step size and squeeze factor as presented in **Figure 3.27**(d). It consistently increases with increase in squeeze factor due to material accumulation as explained earlier but effect of step size is non-linear. However, parts with better accuracy and minimum bulge height are produced when squeeze factor and step size both are increased together along the matrix diagonal. The combined advantages of using a high step size and squeeze factor are shorter forming

time and better geometric accuracy respectively. Therefore, a balance between these parameters needs to be maintained to produce parts with best possible quality.

3.6.5 Boeing fuel cover part formed using TPIF and multi-frame SPIF process

To further demonstrate the robustness of TPIF process, a fuel cover part with intricate features is fabricated using a toolpath generated with process parameters set at step size = 0.5 mm and feed rate = 100 inch/min as shown in **Figure 3.28**. The situation where the TPIF process with a die – support is generally known to be effective is when forming a concave-shaped or a multi-feature part. Here, multi-feature part is defined as a part that comprises of discrete features that are not capable of being formed in single continuous tool path and requires multiple forming steps. For a part like fuel cover, it is near impossible to fabricate its intricate features only through a single – step SPIF process without leading to too much unwanted deformation in the flat surface area. Therefore, TPIF process with the die – support would be necessary to achieve any acceptable level of geometric accuracy. Its accuracy is compared along two cross-sections with the designed part profiles as shown in **Figure 3.31**(a) and (b). Profile deviation of less than 1.1 mm is observed

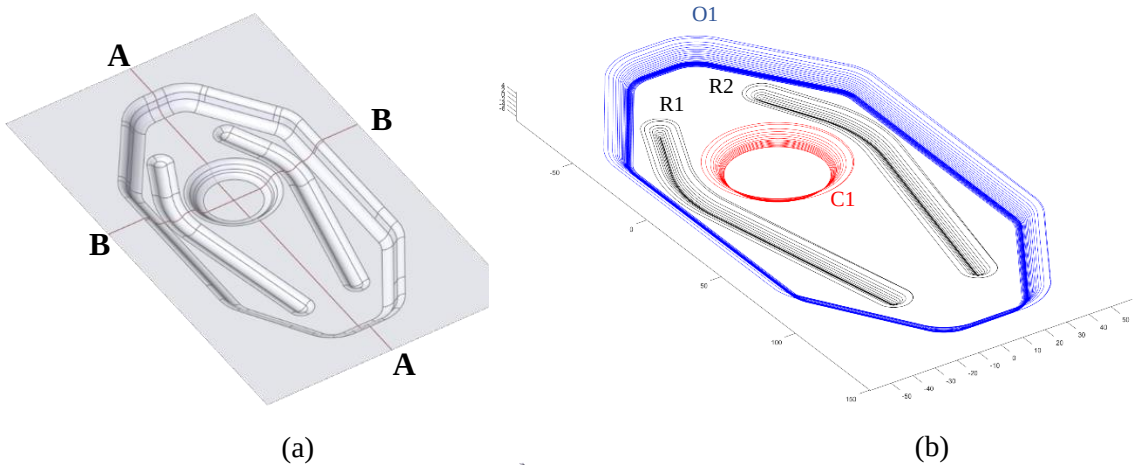

Figure 3.28: (a) Fuel cover part designed with intricated features and (b) toolpath generated for the same with Δz = 0.5 mm and TD = 8 mm

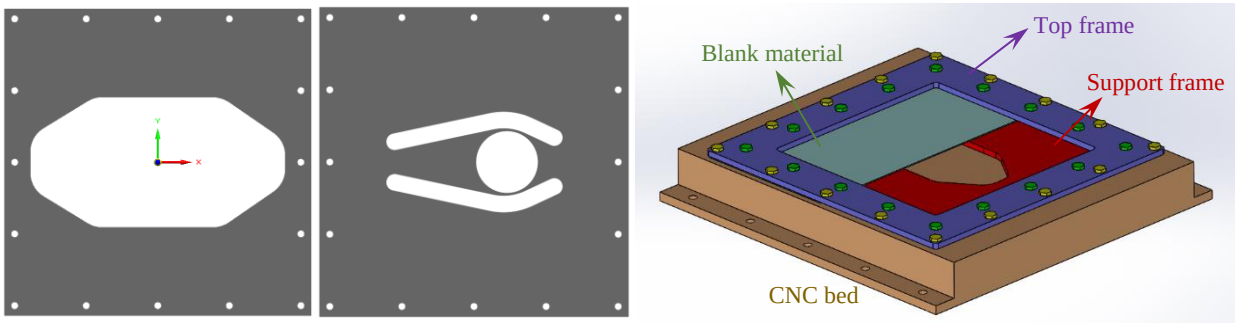

(a) Outer feature frame (b) Inner feature frame (c) SPIF setup in CNC

Figure 3.29: Back - support frames designed and manufactured for fabrication of fuel cover part using SPIF process

along these two cross-sections that includes fine rib features. It tends to deviate more along feature opening regions but remains less than 400 microns in stable wall region.

It must be noted that the cost of manufacturing a die is substantially high compared to the cost of manufacturing a frame since precision CNC machining is needed. Therefore, for a part like fuel cover, a new approach is proposed where the die is replaced with a set of frames as backing-plates to fabricate the same part through SPIF process in multiple stages. This process is named as multi-frame SPIF or MF – SPIF forming strategy. Two separate frames for back support are designed and water-jetted as shown in **Figure 3.29**(a) and (b). The blank material is then clamped between these backup frames and a top frame and mounted on a CNC machine bed as shown in **Figure 3.29**(c). It should be noted that feature forming sequence is different in both TPIF and MF – SPIF fabrication strategies. Outer feature is formed prior to forming inner ribs and circle in case of TPIF (sequence: O1-R1-R2-C1) whereas in case of MS-ISF, inner features are formed first followed by forming outer feature (sequence: R1-R2-C1-O1). It is observed from the geometry comparisons plotted in **Figure 3.31** that TPIF strategy still provides better part accuracy; however, it does come with a drawback of a die requirement. MF – SPIF strategy provides much more flexibility and cost-efficiency in part fabrication and can be believed to significantly improve on the part accuracy if the toolpath is appropriately optimized.

(a) Tool side view: MF-ISF strategy

(b) Tool side view: Base die

(c) Non-tool side view: MF-ISF strategy

(d) Non-tool side view: Base die strategy

Figure 3.30: Images of fuel cover part produced using both TPIF and MF-SPIF fabrication strategies

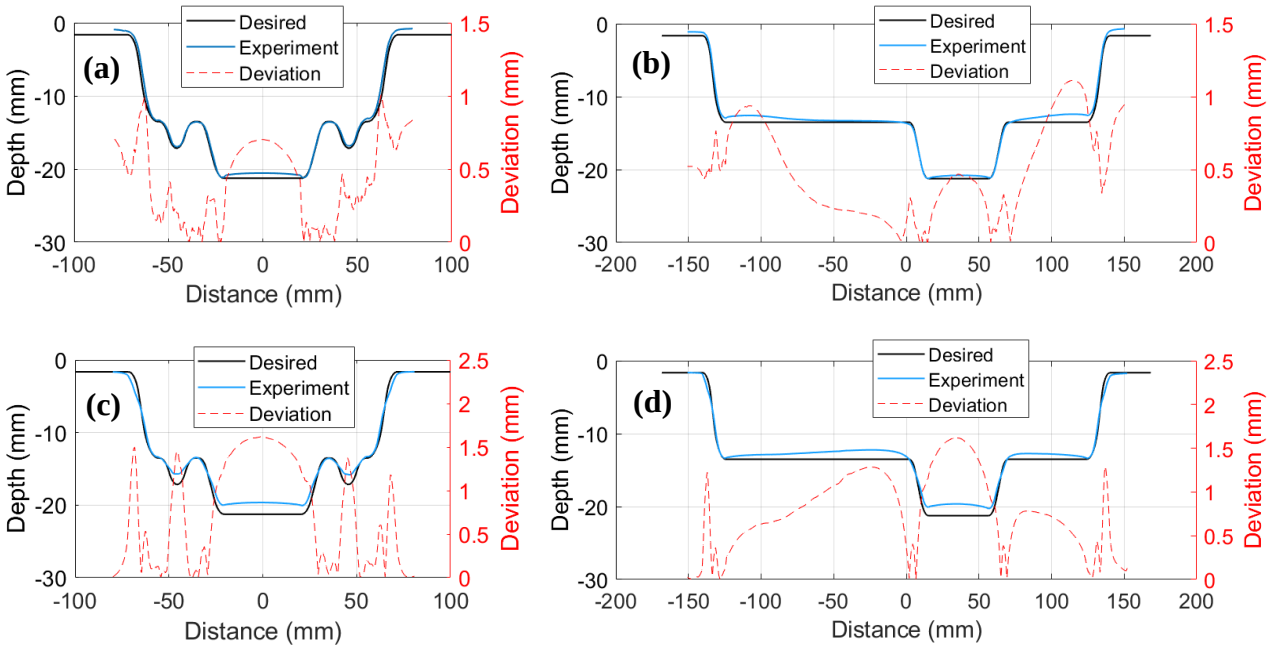

Figure 3.31: Comparison of cross-sectional part profiles of the fuel cover part (a) along B-B formed using TPIF; (b) along A-A formed using TPIF; (c) along B-B formed using MF – SPIF and (d) along A-A formed using MF – SPIF.

3.7 Summary and Conclusions

Experimental results presented in this chapter show significant influence of material squeeze factor on forming forces, part accuracy and material formability. It also shows that effective material squeeze obtained in the experiments is not necessarily same as the squeeze factor programmed in the toolpath due to forming tool deflection and machine compliances. Therefore, a mathematical framework is proposed to be capable of estimating effective material squeeze in two-point incremental forming (TPIF) for a variety of processing conditions and programmed squeeze factors. The same framework could also be implemented in double-sided incremental forming (DSIF) to achieve better process performance as part of follow-up work. Material squeeze between forming tool and back support introduces a compressive stress state in deformation zone and tends to enhance part accuracy and material formability.

Truncated cone, heart shape and fuel cover parts are produced under various processing conditions to analyze these effects in TPIF as follow:

- Effective squeeze factor can be drastically different than programmed squeeze factor due to machine compliances. When cone 67° parts are produced, only partial material squeeze is achieved even for 30% programmed squeeze factor.
- Forming forces are significantly influenced by a small amount of effective material squeeze. Radial force in cone 67° is observed to increases by 23.9% when approximately 2% effective squeeze is obtained. Similarly, in case of heart shape, an increase of 30% is observed in radial force for approx. 5% effective squeeze compared to that obtained in zero squeeze part.
- Part accuracy is observed to increase with positive effective material squeeze in wall region. However, it also accumulates a larger bulge on its undeformed base making geometry accuracy worse. Therefore, a balance between side wall and part's base accuracy needs to be maintained.

- A new multi-stage TPIF forming strategy is proposed to overcome the problem of bulging at the part base and demonstrated its effectiveness in case of heart shape geometry. This strategy helps redistribute the surface material and flatten asperities in order to reduce material accumulation at its base therefore leading to significantly better geometric accuracy when benchmarked against hydroforming process.
- Though material formability in ISF is previously explored to be dependent on step size, sheet thickness and tool diameter, notable impact of part forming rate (strain rate) and squeeze factor are identified while fabricating cone 67° parts. In case of heart shape, an interesting part failure mode is observed along the corner rib due to high bulge formation.
- A new MF – SPIF process is proposed to fabricate any parts with intricate features using SPIF process without any die-support to improve process flexibility.

Chapter 4
Constitutive Material Model and Fast Finite Element Analysis of µSPIF Process

4.1 Introduction

As incremental forming is a relatively new sheet metal forming process, very limited analytical and finite element prediction models are available in literature to study the process mechanics and improve its performance. Thus, most studies involve many trial-and-error iterations to optimize the processing conditions in order to take advantage of the major advantages of high flexibility and material formability without minimal tradeoff on geometric accuracy. However, reducing efforts of trial-and-error iterations is of utmost importance to make a process financially viable by reducing the amount of lead time and material tooling costs. Advances in finite element analysis (FEA) can be used to accurately represent the complex deformation process and capture local mechanical response of the material under the forming tool. In addition, it will help better understand the process mechanics and complement the further development of analytical process prediction models.

The main objective of this chapter is to develop an FEA model to represent the μISF process so that the unknown stress state, material movement, excessive thinning and part failure can be successfully predicted for any given set of process parameters and part geometry. With this clear understanding, process performance quantifiers such as geometric accuracy and mechanical strength can be significantly improved in conjunction with failure prevention. To achieve this,

material characterization and model verification is performed to validate the finite element analysis with sufficient accuracy.

4.2 Literature Review

4.2.1 Grain size effect on material constitutive model

Material behavior varies greatly when a conventional forming process is scaled down to the micro/mesoscale from macroscale. Conventional constitutive models can no longer be used to describe material behavior in this case. Peng et al. [51] developed a material model for size effect based on the hypothesis of surface model. Grains on the material surface were less restricted compared to that in the bulk. Therefore, surface grains were considered to have similar material properties to a single crystal whereas inner grains are more like polycrystal material as shown in **Figure 4.1**. According to the surface model, the material flow stress consisted of two terms: (a) the stress of inner grains and (b) the stress of surface grains. The stress of inner and surface grains was expressed as:

$$\sigma_s(\epsilon) = m\tau_R(\epsilon) \tag{4.1}$$

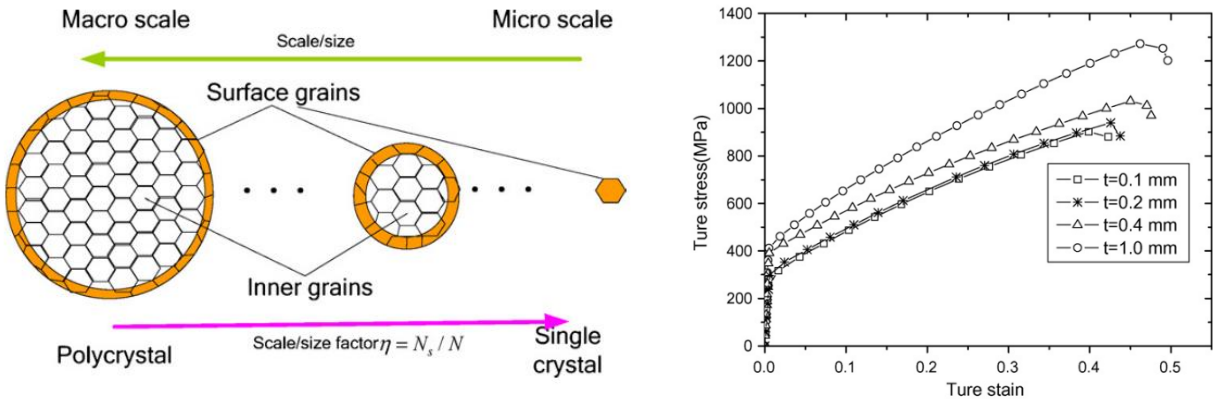

(a) (b)

Figure 4.1: (a) Schematic of grain distribution in material section and (b) True stress-strain curves for SUS304 material (Peng et al. [51])

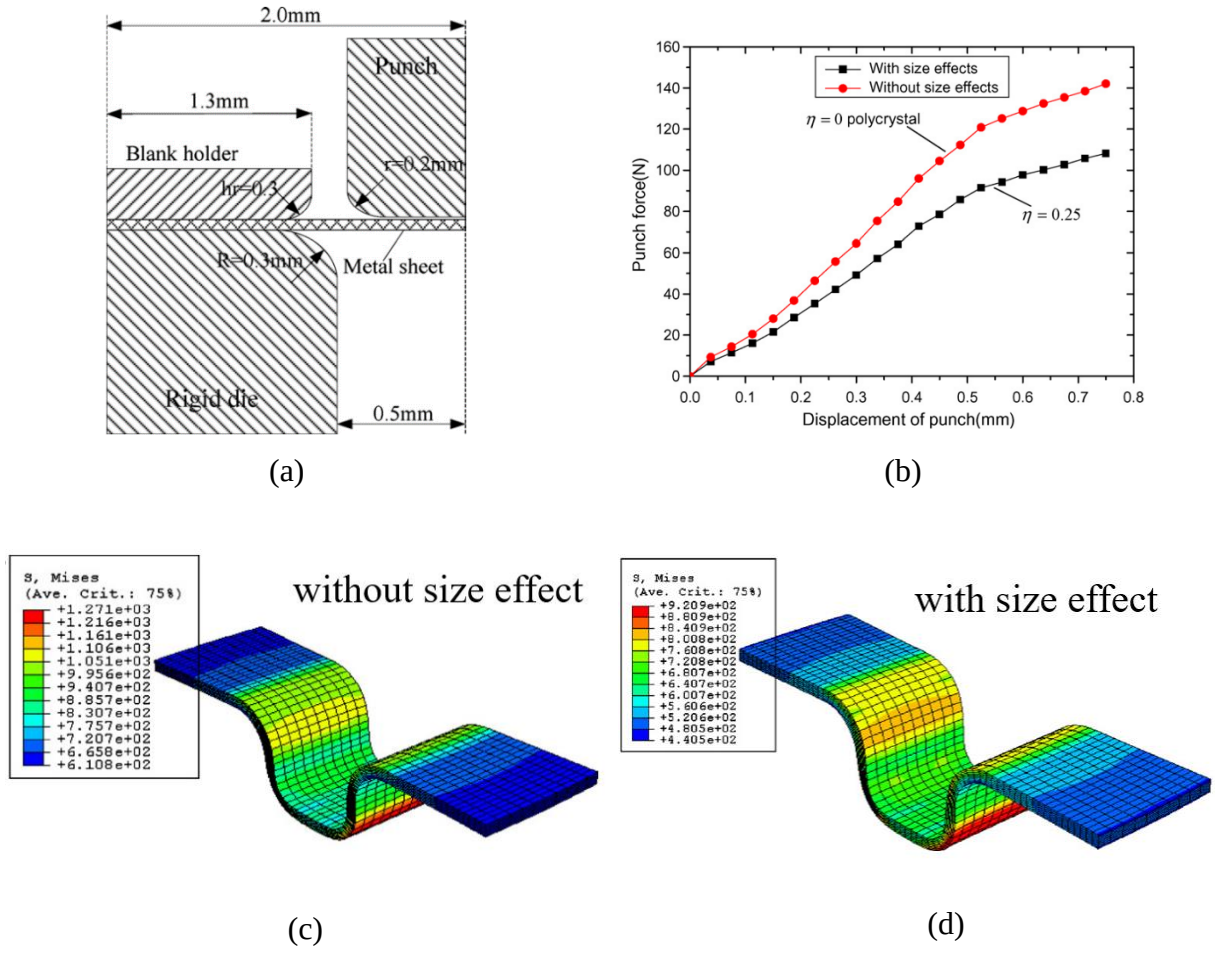

Figure 4.2: (a) Schematic of micro sheet forming process; (b) comparison of the punch force vs. relative punch stroke; (c) comparison of Mises stress distribution of micro-stamping part with and (d) without considering size effect in material property (Peng et al. [51])

$$\sigma_i(\epsilon) = M\tau_R(\epsilon) + \frac{k(\epsilon)}{\sqrt{d}}$$

where, σ_s and σ_i are the flow stresses of surface and internal grains respectively, m is the orientation factor, d is the graine size, M is the orientation factor related to the slips on deformation systems.

The authors introduced a scale factor (η) as the ratio of the number of surface grains (N_s) to total grains (N) in the specimen. Based on this analysis, flow stress considering size effect was expressed as:

$$\sigma_{micro/meso}(\epsilon) = \frac{N_s\sigma_s + N_i\sigma_i}{N} = \frac{N_s m\tau_R(\epsilon) + N_i * \left[M\tau_R(\epsilon) + \left(k(\epsilon)/\sqrt{d}\right)\right]}{N} \quad (4.2)$$

where, N_i is the number of inner grains, m is the orientation factor, d is the graine size, M is the orientation factor related to the slips on deformation systems and k is the locally intensified stress needed to propagate general yield across the polycrystal grain boundaries. Assuming sheet width (d) to be much higher compared to its thickness (t), the scale factor can be calculated as η = d/t.

Tensile specimens were prepared by them, and tests were performed using SUS304 stainless steel sheets with different thicknesses. The true stress-strain curves obtained from these tests are shown in **Figure 4.2**(b). It is observed that the flow stress is decreasing with decrease in sheet thickness for material with same grain size. This effect is attributed to the less restricted surface grains compared to inner grains of the material.

A finite element model for U-shape micro-forming was also developed to study the influence of material size to micro-sheet stamping process as shown in **Figure 4.2**(a). Size dependent material constitutive model as proposed in their study was implemented in finite element model with different scale factor inputs (η). A clear difference of stress distribution and forming forces was observed between the results in which size effect was considered and not considered as shown in **Figure 4.2**(b), (c) and (d) respectively. This difference occurs because of the size dependent term in their proposed material model which diminishes in case of conventional polycrystal model.

4.2.2 Grain size effect on material formability

In the micro-forming process, the reduction of limiting drawing ratio or material forming limit is observed in deep drawing of metal foils is a major challenge. Wielage et al. [52] conducted pneumatic bulge tests on a 2 µm thick cold-rolled aluminum foil (Al99.5) to get it's forming limit diagram. Contrary to the expected concentric strain pattern, a highly irregular local (non-uniform) distribution of strain was observed via digital image correlation (DIC) on the specimen surface as shown in **Figure 4.3**(a). The fractures are randomly distributed between the boundary and center

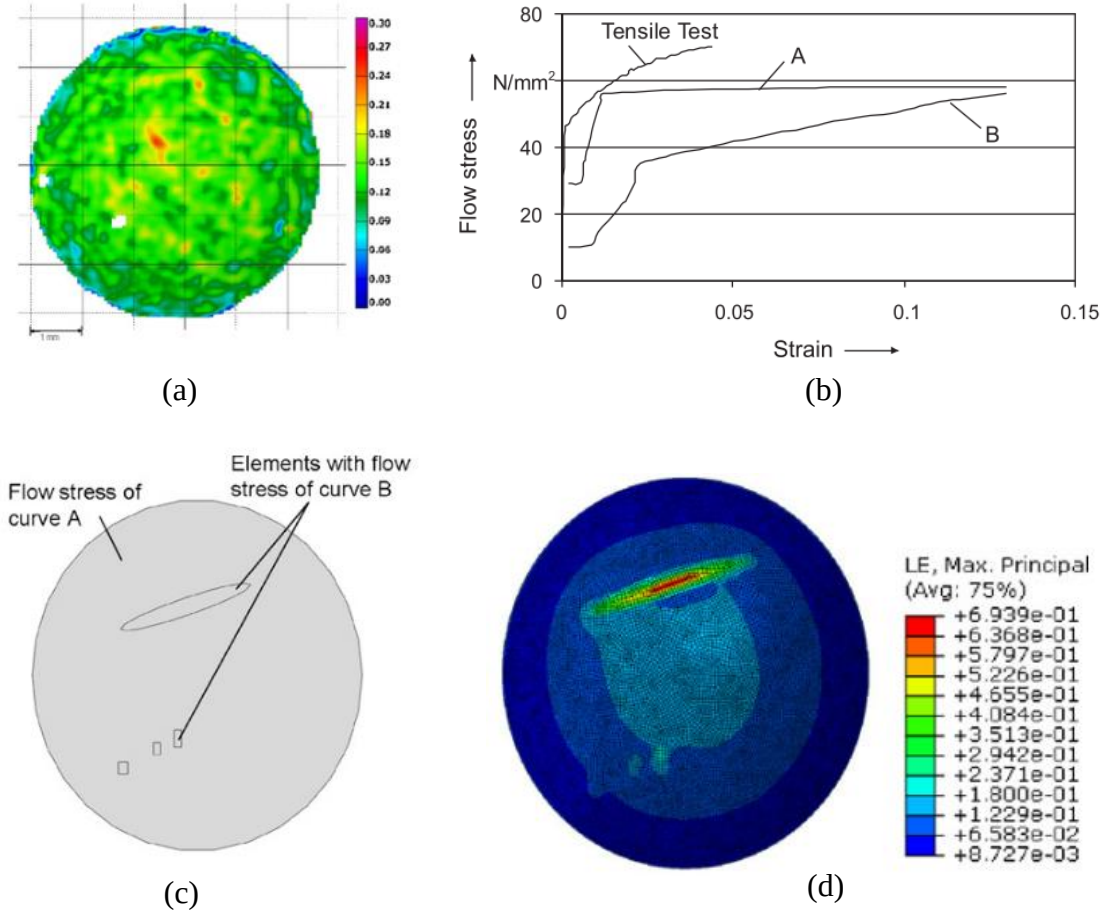

Figure 4.3: (a) von Mises strain of the Al99.5 sample just before crack; (b) Flow curves of different regions of the specimen; (c) Simulation model of the pneumatic bulge test with the material property assignment; (d) Simulation result of the true strain distribution (Wielage et al. [52])

of the specimen. It is observed through simulations that non-uniform fracture behavior of thin specimen is due to non-uniform material flow (stress-strain curve) as compared in **Figure 4.3**(d).

Peng et al. [53] performed a systematic forming limit analysis to study the effect of grain size on material formability. Cu – FRHC sheets with 0.2 mm and 0.4 mm thickness were annealed at different temperatures and used in the experiments (Marciniak tests) to determine FLC and FFLC shown in **Figure 4.4**. They observed a significant reduction in material formability with the increase in grain size (agrees with surface layer model, i.e., ratio of surface to inner grains presented in previous subsection). For smallest grain size, the strain is uniformly distributed during deformation. In contrast, inhomogeneous strain distribution is observed for the largest grain size.

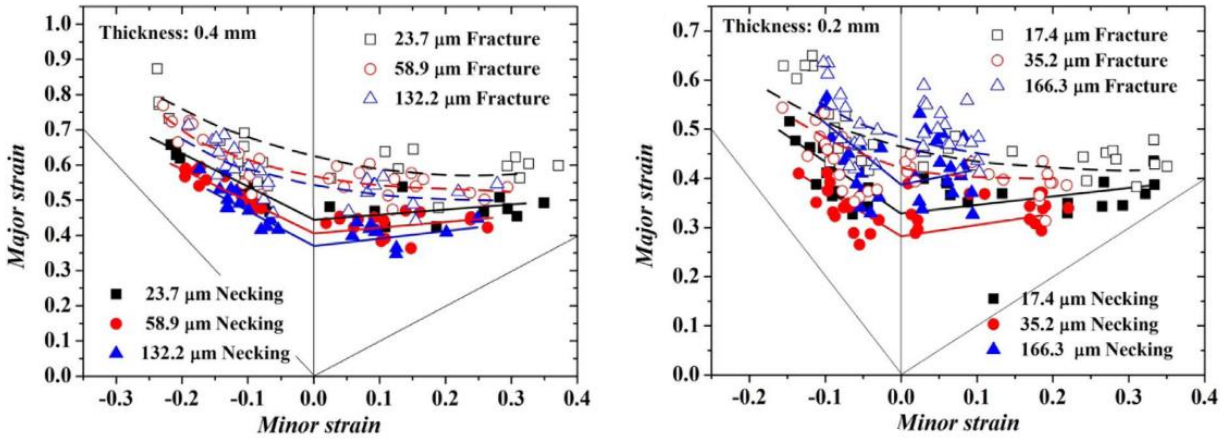

(a) (b)

Figure 4.4: The forming limit curves obtained through Marciniak test for Cu – FRHC sheets with thickness: (a) 0.4 mm and (b) 0.2 mm (Peng et al. [53])

4.2.3 Finite element analysis of incrementally formed parts

Numerical simulations of ISF process are widely utilized to predict its process performance and gain knowledge of underlying mechanics. Some of the key considerations in designing FE models for incremental forming to attain good precision, highlighted by Behera et al. [54], are

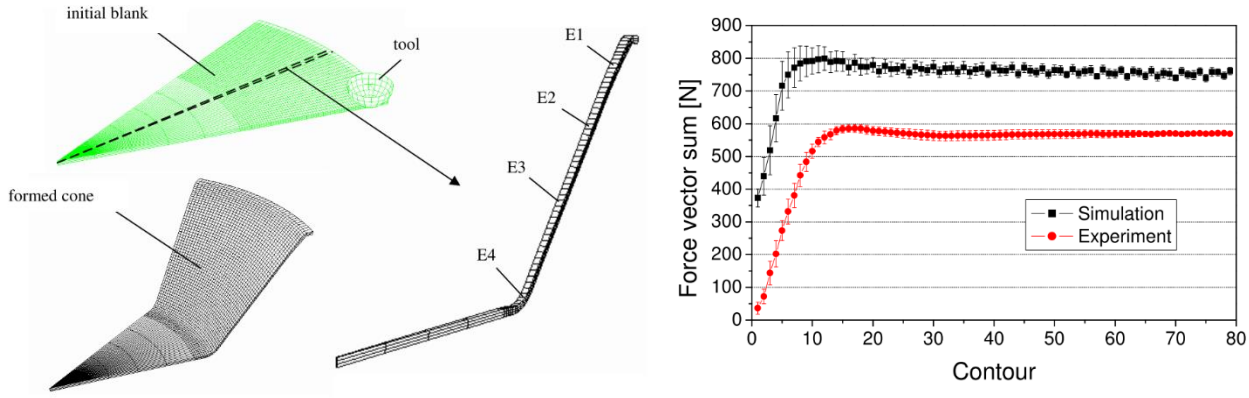

Figure 4.5: (a) FE sub model for ISF process and (b) comparison of numerically predicted and experimental forces (He et al. [55])

constitutive material models, choice of integration schemes (explicit or implicit), element type (solid or shell element) and surface interaction modeling.

He et al. [55] developed an elasto-plastic FE model using implicit Abaqus/Standard package for the simulations of SPIF process. Implicit solver is known to consume high computation time. Therefore, only a 40-degree pie-shaped blank was modeled to simplify the numerical analysis as shown in the **Figure 4.5**(a), assuming the axisymmetric deformation condition of a conical geometry. Also, a simple material model with Swift hardening law, isotropic-hardening and von-Mises yield criteria was used in the simulation. It showed promising results in explaining plain-strain state of deformation but struggled to achieve good prediction accuracy in forming forces when compared with experimental values as per **Figure 4.5**(b).

Li et al. [56] developed a similar FE model with a full deformable blank of fine solid elements and explicit time integration scheme available in LS-Dyna. Although, a simple material model with isotropic hardening was used, predicted forming force values closely matched to that obtained through experiments. They confirmed from the results that deformation behavior in ISF process was a combination of stretching, shearing and bending. Other FE simulations explained

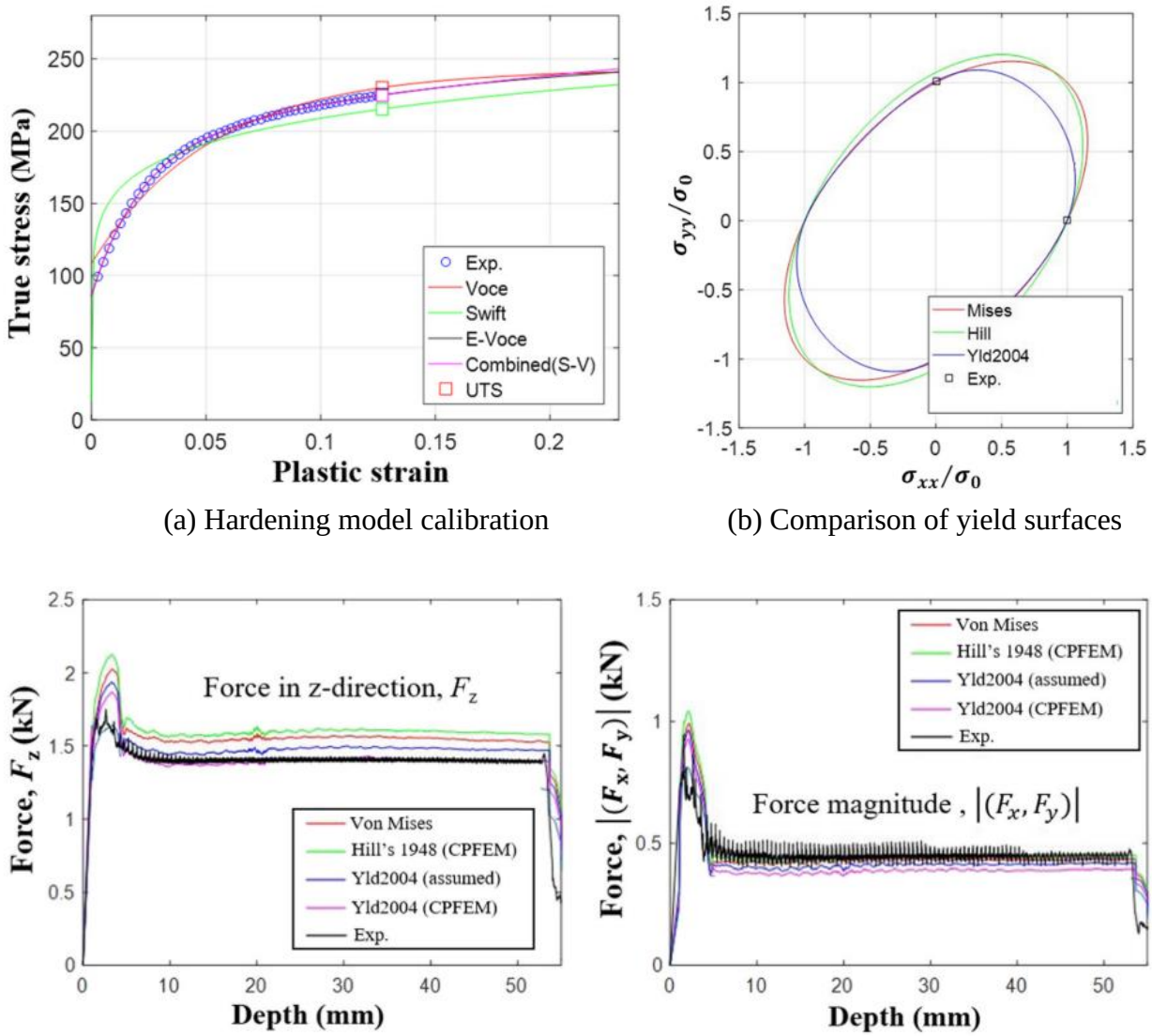

(a) Hardening model calibration

(b) Comparison of yield surfaces

(c) Comparison of axial forces

(d) Comparison of radial forces

Figure 4.6: Advanced material model developed for ISF process and the validation of its FE simulation through reactionary force values (Esmaeilpour et al. [50], [58])

that kinematic hardening models could predict much better part geometries compared to simple isotropic hardening law [57].

Esmaeilpour et al. [50], [58] pointed out that significant out-of-plane shear stress developed in the ISF process requiring implementation of a 3D yield function to accurately represent its complex nature of 3D stress state. They calibrated all the parameters of Barlat Yld2004-18p non-quadratic yield function using crystal plasticity model as out-of-plane tensile test properties could

not be obtained experimentally. The extended Voce-type hardening model is shown to better represent the material behavior and therefore used in combination with Barlat's yield criteria as plotted in **Figure 4.6**(a) and (b), respectively. The developed FE model was run to simulate the fabrication of cone 45º geometry and validated against experimental results. Predicted axial and radial forces showed great agreement with the experimentally obtained values as compared in **Figure 4.6**(c) and (d) respectively. This analysis demonstrated the importance of advanced material modeling for incremental forming where complex stress states played a major role.

Seong et al. [10] carried out simulations using implicit FEM solver, planar anisotropic material properties and Hill's 1948 yield function to uncover suppression of necking in ISF. They utilized stress-based FLC (strain path independent) for through-thickness necking analysis and discovered that stress state of top, middle and bottom part surface were different in their deformation history, which led to suppressed necking.

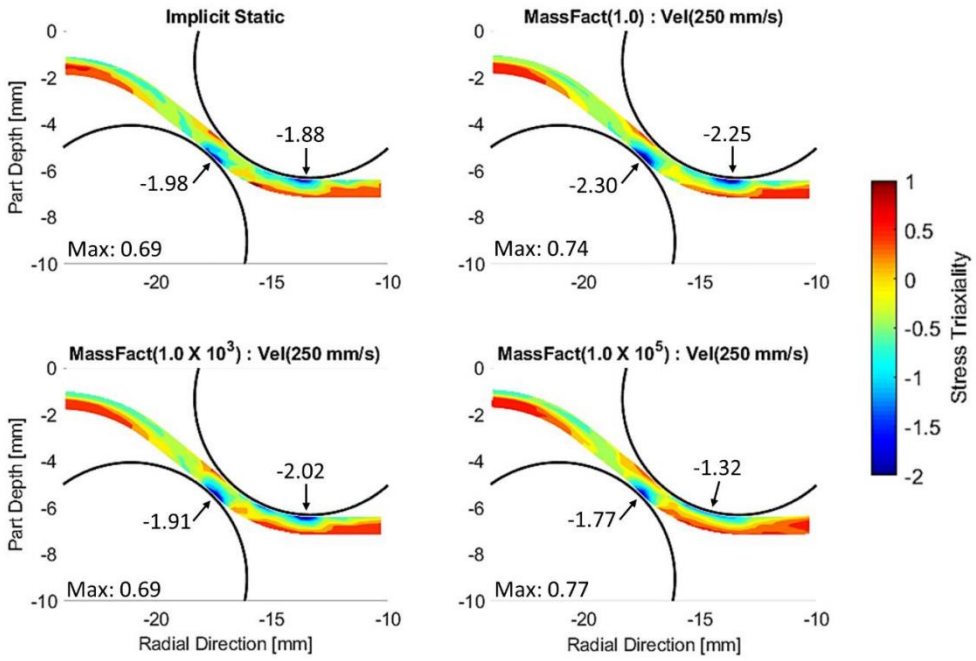

Figure 4.7: Comparison of stress triaxiality in a cross-sectional profile for different mass scaling schemes (Moser et al. [59])

Moser et al. [59] performed extensive analysis of ISF simulation by ABAQUS/Explicit solver scheme to study the effect of mass and velocity scaling on prediction results. Using a simple DE model for DSIF process, they demonstrated that changing mass scaling significantly increased the kinetic energy in the system. However, it did not have much influence on the forming forces other than some scattered sporadic values. Despite that, mass scaling was shown to have considerable effect on the forming mechanics. The comparison of stress triaxiality under the tool shown in **Figure 4.7** displays that increasing mass scaling leads to reduction in triaxiality in the deformation zone moving it away from accuracy prediction. In classical fracture mechanics, low triaxiality implies that the deformation state is approximately close to ”plane stress” whereas, high stress triaxiality implies a ”plane strain” deformation mode. Therefore, mass scaling must be cautiously used in the range of 102 to 104. Still, its value is dependent on a case-by-case basis.

4.3 Constitutive Material Model of AL1100

Aluminum 1100 is chosen for all the baseline experiments and model verification in this chapter since it is close to pure aluminum and known for excellent formability characteristics. It has strong corrosion resistance and is well-known for applications in fin stock, heat exchanger fins, spun hollowware, dials and name plates. The typical chemical composition for AL 1100 is shown in **Table 4.1**.

Table 4.1: Chemical composition of aluminum 1100 (in wt. %)

Al	Cu	Mn	Si + Fe	Zn	Other
> 99.00%	0.05 to 0.20%	< 0.05%	< 0.95%	< 0.10%	< 0.15%

Uniaxial tensile tests of 50 μm thick foils are performed to characterize strain hardening behavior and plastic flow curve. Due to the low rigidity of thin foil, it was sandwiched between thick metal sheets and cut to the required specimen shape (geometry was proposed by Hayashi et al. [60] and shown in **Figure 4.8**(a)) using wire-cut EDM machine. Tensile tests are performed on

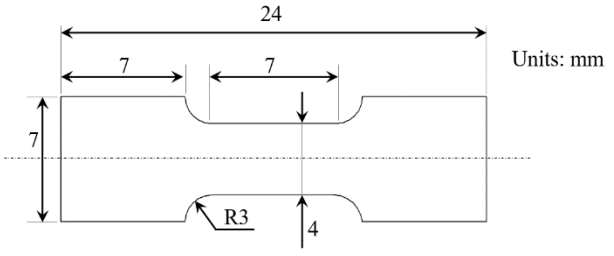

(a) Tensile test specimen

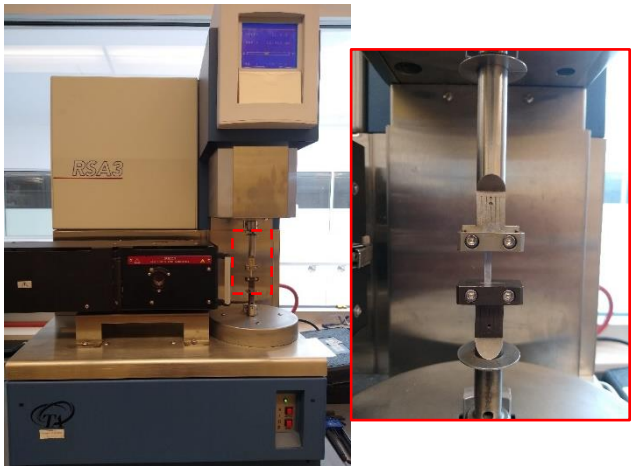

(b) Micro-tensile testing setup

Figure 4.8: Micro-tensile test specimen and testing setup used for AL 1100 material

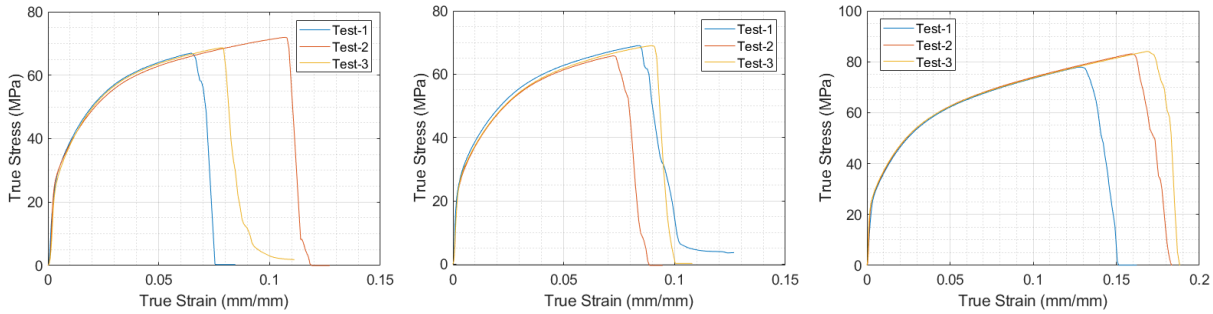

(a) Rolling direction (b) Transverse direction (c) Diagonal direction

Figure 4.9: True stress-strain curve obtained for AL 1100 material along rolling, diagonal and transverse directions

a DMA RSA-3 of TA Instruments equipment at the University of Michigan. To ensure minimal dynamic effect on the results, specimen is uniaxially loaded with a quasi-static strain rate of $1 * 10^{-3}$ per second. Each test is repeated three times to ensure repeatability and minimize experimental errors. Tensile tests samples are prepared from rolling, transverse and diagonal directions to study the effect of material anisotropy on flow stress as shown in **Figure 4.9**. Results show that flow stress in all three directions look very similar and the material can be safely assumed to be isotropic in nature while developing a FE model. Only difference observed in these tests is – tests along diagonal direction tends to have 50% higher strain at failure compared to the other two directions.

As a response to the experimentally obtained true plastic curve shown in **Figure 4.10**, various strain hardening functions such as Ludwick 1909, Prager 1938, Hollomon 1944, Swift 1947, Voce 1948, etc. can be fit through it to mathematically represent the material plastic behavior under uniaxial loading. However, it's choice can play a critical role when used in μISF simulation. For comparison, Holloman and Voce-type strain hardening functions are chosen and verified in FEA to demonstrate the significant difference between them. Both these strain hardening functions are mathematically represented as Equations (4.3) and (4.4), respectively.

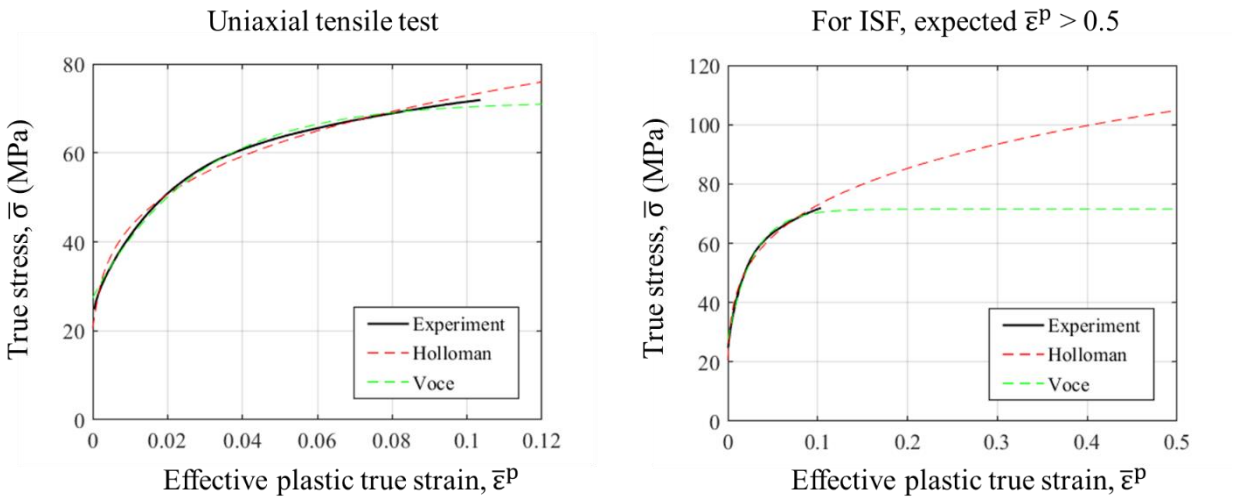

(a) Range: $0 < \bar{\varepsilon}^p < 0.1$ (b) Range: $0 < \bar{\varepsilon}^p < 0.5$

Figure 4.10: (a) Effective plastic stress-strain response of Al 1100 material under uniaxial tensile loading and (b) Holloman and Voce strain hardening functions fit through the experimental data

$$\bar{\sigma}(\bar{\varepsilon}^p) = K * (\bar{\varepsilon}^p)^n \tag{4.3}$$

$$\bar{\sigma}(\bar{\varepsilon}^p) = \sigma_Y + (\sigma_S - \sigma_Y) * \left[1 - e^{-\beta\bar{\varepsilon}^p}\right] \tag{4.4}$$

where, $\bar{\sigma}$ and $\bar{\varepsilon}^p$ are plastic true stress and strain respectively; K and n are the strength coefficient and strain hardening exponent in Holloman law; σ_Y, σ_S and β are initial yield stress, saturation stress and material constant in Voce-type hardening law, respectively.

True stress value via Holloman-type hardening function keeps monotonically increasing with effective plastic strain whereas, it asymptotes to a constant σ_S in Voce-type hardening function. Material parameters are fit through the measured true stress-strain data by minimizing the sum of squared errors to determine the material parameters given in **Table 4.2**. When compared, both of them appear to be in good agreement with the experiments as shown in **Figure 4.10**(a). It must be noted from the plot that effective plastic strain at fracture in tensile test is less than 0.1. However, it reaches above five to ten times of that value in the case of incremental forming. Upon extrapolation to large strain values, Holloman and Voce-type functions start to deviate from each other as shown in **Figure 4.10**(b) and might lead to erroneous prediction results.

Therefore, the choice of hardening function will have a significant influence of any results obtained by finite element analysis.

Table 4.2: Material parameters obtained for Holloman and Voce-type strain hardening functions by uniaxial tensile test

K	n	σ_Y	σ_S	β
122.6	0.226	27.4	44.1	36.08

Ideally, the strain hardening function must fit somewhere between the two compared laws and therefore can be represented as a mixed Holloman-Voce function as constituted by Equation (4.5) where α_m is an additional material parameter that cannot be obtained through a tensile test. Additional material characterizations such as shear or in-plane torsion tests need to be performed to measure its value at large strains. For the investigation presented in this chapter, Holloman-type strain hardening model is chosen to conduct all finite element simulations and analyze process mechanics.

$$\bar{\sigma}(\bar{\varepsilon}^p) = \alpha_m \left[K * (\bar{\varepsilon}^p)^n\right] + (1 - \alpha_m) * \left(\sigma_Y + (\sigma_S - \sigma_Y) * \left[1 - e^{-\beta \bar{\varepsilon}^p}\right]\right) \qquad (4.5)$$

According to the classical theory of plasticity, several properties are required to model deformation behavior of a material under biaxial or triaxial loading conditions. Summary of those properties used in case of Al 1100 for finite element analysis are given below:

- a linear elastic law defined by Young's modulus below the strain where any plastic deformation begins.
- a plastic flow rule through Holloman-type hardening function is used to define evolution of plastic strain under loading.
- the classical von Mises (J_2 – plasticity) yield criterion is used to define the onset of plastic deformation under multi-axial loading condition.

- isotropic hardening is utilized to characterize evolution of J_2 – plasticity in case of cyclic loading-unloading condition.

Yield criterion not only helps the prediction model with defining onset of plastic deformation. But it also helps with determining the direction of incremental plastic strain (via associated plastic flow rule in metals). Some of the literature suggests that complex yield loci such as Barlat's Yld2000-2D (specifically designed for aluminum alloys) and Yld2004-18p that incorporates material anisotropy can provide much more accurate results due to triaxial stresses in incremental forming. However, in this study, it is considered that a simple J2 - type yield locus can provide sufficient prediction model to beginning the process modeling. It is also known as von Mises yield function and is given by Equation (4.6):

$$\sigma_Y = \frac{1}{\sqrt{2}}\left[\left(\sigma_{xx}-\sigma_{yy}\right)^2+\left(\sigma_{yy}-\sigma_{zz}\right)^2+\left(\sigma_{zz}-\sigma_{xx}\right)^2+6\left({\sigma_{xy}}^2+{\sigma_{yz}}^2+{\sigma_{xz}}^2\right)\right] = \sqrt{\frac{3}{2}s_{ij}s_{ij}} \tag{4.6}$$

where, σ_Y is the initial yield stress; σ_{ij} is effective stress; and s_{ij} are the deviatoric stresses.

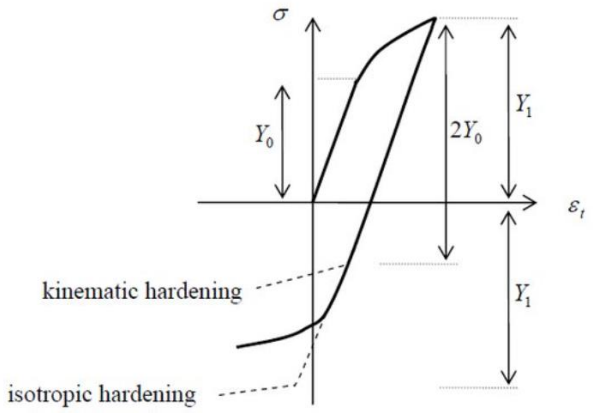

Figure 4.11: Effect of permanent material softening due to kinematic hardening effect

According to the Bauschinger effect, a reduction in yield strength must be observed under reverse loading followed by forward loading due to permanent softening as illustrated in **Figure**

4.11. However, it is difficult to obtain tension-compression data of thin aluminum foils due to low rigidity. Therefore, isotropic hardening is used to determine the evolution of yield locus is case of cyclic forward and reverse loading. This assumption is expected to over-predict the yield strength under reverse loading leading to marginal over-prediction of forming forces through finite element analysis. This might also lead to some inaccuracies in the prediction of sheet spring-back and residual stresses.

4.4 Development of Finite Element Model

Considering the above discussion, it is highly recommended that numerical parameters related to finite element analysis such as mesh refinement, element-type selection, boundary conditions and artificial acceleration via mass/velocity scaling must be fine-tuned first to optimize the FEA model and not risk over-calibrating the material constitutive model to match with

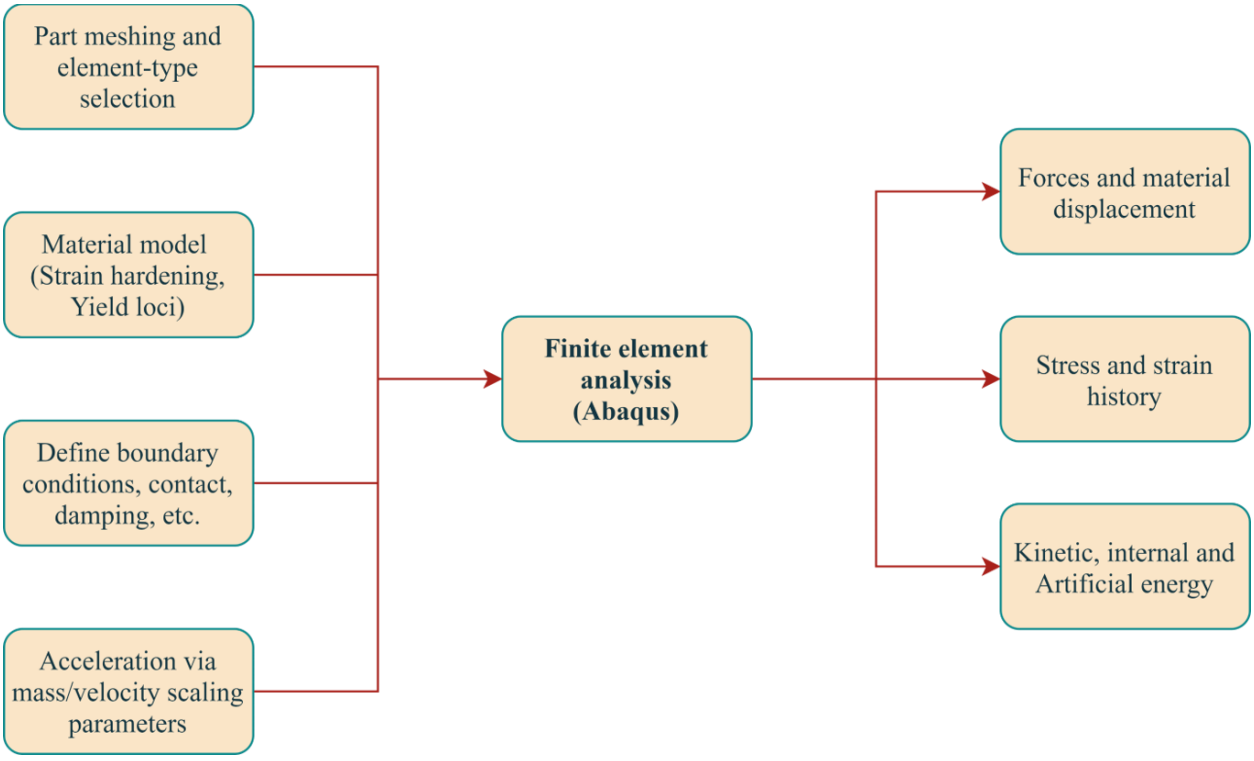

Figure 4.12: An illustration of required inputs and expected outputs for finite element analysis of incremental forming process

experimental results. In general, if all these parameters are tuned appropriately, it is expected of finite element analysis to provide an accurate prediction of forming forces, material movement and stress-strain history. Overview of the inputs and expected outputs of FE analysis is illustrated by **Figure 4.12**.

4.4.1 Part meshing and element-type selection

In the literature, a few researchers have developed an FEA model for incremental forming process by implementing only a quarter or one-sixth of the sheet domain for simulation of axisymmetric conical parts to reduce the computation cost. However, it is well understood by the reduced domain analysis that capturing circumferential strain and material movement along the tool motion direction could be a challenging task. On top of that, µISF tends to have much higher material movement along tool motion due to high friction in the tool-sheet interface. Therefore, a full sheet domain is modeled in this study to avoid any assumptions of plane strain deformation in a plane perpendicular to tool motion.

A thin metal foil is modeled in a circular shape of 8 mm diameter and 50 µm thickness to appropriately imitate the experimental conditions. It is divided into two sections - A. one under deformation zone (which comes in contact with the tool) and B. the flange area (where tool does not contact the foil) as shown in **Figure 4.13**. A coarse-size mesh is implemented in the flange area as strains are expected to be much lower here compared to that under deformation zone. Whereas, large through thickness strain is expected in the deformation zone based on experimental observation and therefore, much finer mesh is implemented there. Also, researchers have studied the effect of number of elements in through the thickness direction. They concluded that five elements in thickness are most optimal to accurately capture high shearing effect of incremental forming process while keeping computation cost low. Also, in case of low wall angle parts, only

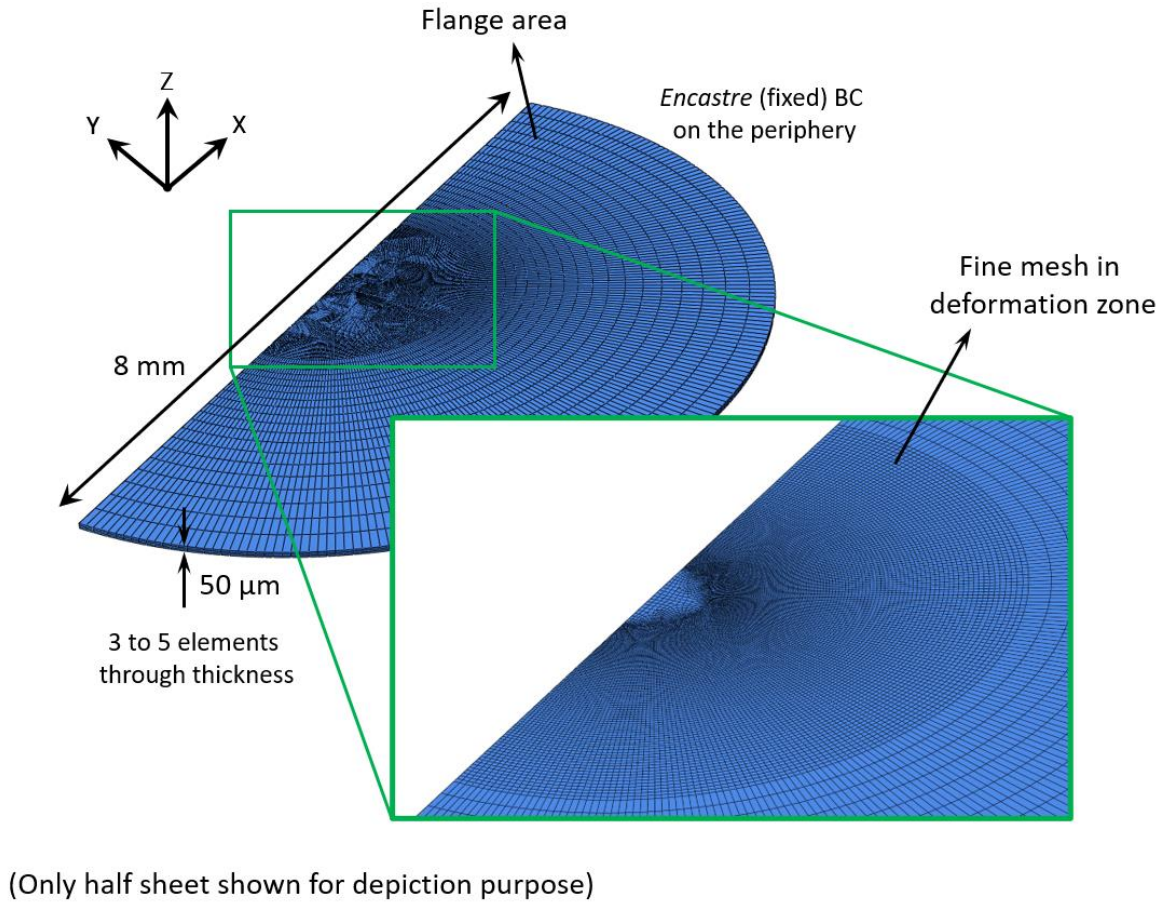

Figure 4.13: Part mesh created for the circular sample of AL 1100 in pre-deformation state

three elements in thickness could yield ”good enough” prediction results of forming forces and part geometry. So, both three and five elements in thickness are implemented in the model to analyze its effect in µISF process which led to a total of 125,670 and 209,450 solid continuum elements respectively.

There is limited research available on selection of element-type for a successive deformation process with very large strain as obtained in case of µISF. A qualitative analysis based on expert knowledge is performed in choosing suitable element type for this process. Some of the possible options available are first-order and second-order hexahedral elements with combination of either reduced or full-integration solving scheme. An 8-node hexahedral linear solid element

with reduced integration (C3D8R) is consistently used without hourglass control to keep the computation time low and still obtain good prediction accuracy.

Kim et al. [61] conducted a parametric study on FE simulations of incremental forming process to analyze the effect of analytical and discreet rigid tool on the prediction of forming forces. They observed abnormal force peaks in the predictions with discreet rigid tool due to unstable contact between coarse rigid elements of tool and the workpiece. Therefore, in this study, the tool is modeled to be analytically rigid with a hemispherical end of 200 μm diameter. It is expected to reduce contact noise due to smoother surface description and predict more realistic trend of reactionary forces.

4.4.2 Defining tool-sheet contact and boundary conditions

In experiments, the aluminum foil is cut to 25x25 mm size and clamped between two frames with open deformation area of 8mm diameter. The area of foil clamped under the frames does not draw in during part fabrication. This simplification should not have any effect on the simulation results as the area under frames does not go under any type of deformation. However,

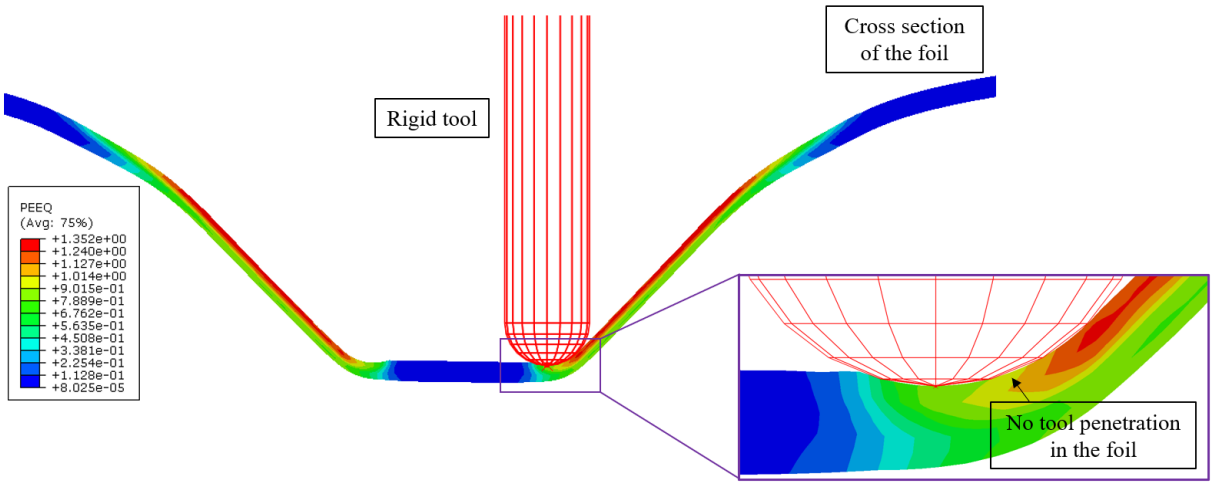

Figure 4.14: Cross-sectional view of the µISF simulation verifies that no penetration condition of tool surface in the metal foil is satisfied by penalty contact enforcement algorithm

if modeled, it would increase the number of elements significantly making it computationally expensive. Therefore, sheet only in the free area is modeled with all six degrees-of-freedom constrained along its peripheral edge. Rotational degrees-of-freedom for the tool are constrained and the toolpath is applied to its reference point in x, y and z-directions as "Displacement" boundary conditions.

A penalty method of contact enforcement is utilized to define contact in the tool-sheet interaction area. For this, a general-type surface-to-surface contact between top surface of the sheet and tool outer surface is defined with frictional coefficient (μ) of 0.1 to avoid any penetration of tool surface into foil material. It can be seen in the simulation results for the benchmark cone 45° in upcoming sections, the contact condition is successfully achieved without any visible node penetration as shown in **Figure 4.14**. In μISF, though the friction is expected to be much higher, the modeling procedure is begun with μ = 0.1 but will later be increased to observe its effect on stress-strain distribution and reactionary forces on the tool.

4.4.3 Artificial acceleration via mass and velocity scaling

As mentioned in previous chapters, parts in μISF are formed using a hemispherical tool requiring thousands of tiny deformation steps to the achieve desired shape. It means that simulation for the same could easily take several weeks to complete and produce the prediction results. Also, implicit analysis requires large number of iterations in each time step to achieve "true" static equilibrium in any structural simulations. Meanwhile, explicit analysis determines the solution by forward Euler algorithm that does not require multiple iterations and advances the kinetic state from the information already known. Therefore, it motivates that explicit analysis could play a better alternative where for metal forming analysis of very large strains and large number of deformation steps.

$$\Delta t_i = \frac{L_e}{C_0} \qquad \text{where, } C_0 = \sqrt{\frac{E}{\rho}} \qquad (4.7)$$

In explicit analysis, the stable time increment is defined as the minimum time that a dilatational (i.e., pressure) wave takes to move across any element in the model. It is calculated based on material density (ρ) and characteristic length (L_e) of the mesh elements given by equation (4.7); where, C_0 is the dilatation wave speed (assuming Poisson's ratio equal to zero) and E is the Young's modulus. Assuming the tool feed rate of 0.5 mm/sec, a simulation of cone 45° would require more than a trillion of time increments taking total simulation time to more than a month even with explicit analysis.

The goal of this chapter is to model the process in the shortest time period (or with the maximum mass and velocity scaling), in which inertia forces are still insignificant keeping the process quasi-static. One of the major advantages of explicit analysis is the availability of two approaches to obtaining economical quasi-static solutions with an explicit FEA solver:

1. Velocity scaling or increased load rate:
    - Increasing the load rate by a factor of T_s would help artificially reduce the total time scale keeping the time increment same. Therefore, it will help reduce the total simulation time by the factor of T_s.
    - However, increasing the load rate will proportionally increase the material strain rate as well. It makes this approach unsuitable for rate-sensitive materials.
    - High velocity scaling changes the inertia conditions of the specimen and leads to increase in kinetic energy rendering the metal forming process dynamic ("Non"- quasi static). To avoid this, excessive velocity scaling should not be used.

2. Mass scaling:

- If we artificially increase the material density by a factor of f^2, the dilatational wave decreases and therefore increases the stable time increment by a factor of f as given by equation 4.8

$$C = \sqrt{\frac{E}{f^2\rho}} = \frac{C_0}{f} \qquad \text{and} \qquad \Delta t_i = \frac{L_e}{C_0} f \qquad (4.8)$$

- Similar to velocity scaling, excessive mass scaling also has adverse effects on the simulation health and leads to increased inertia. It can increase the artificial strain energy of the simulation model by hourglassing and reduces the geometric accuracy of the prediction results.

4.5 Benchmarking and Validation with a Cone 45° Geometry

For bench-marking a high-fidelity finite element model of µISF process, a truncated conical part with 45° wall angle designed in **Figure 2.12** (section 2.5.1) is formed using process parameters set as follow:

- Part opening diameter = 2 mm
- Part depth = 0.75 mm
- Tool diameter = 200 µm
- Step size = 10 µm

Table 4.3: Input parameters and material properties used for benchmarking of finite element analysis

		Case 1	Case 2	Case 3	Case 4
Targeted part shape		Truncated cone shape with **45º wall angle** ABAQUS\Explicit			
Material model	Hardening Law	Holloman type, isotropic	Holloman type, isotropic	Holloman type, isotropic	Holloman type, isotropic
	Yield locus	von Mises	von Mises	von Mises	von Mises
Element type		Solid element with reduced integration	Solid element with reduced integration	**Shell element** with reduced integration	Solid element with reduced integration and **hourglass control**
Mass scaling factor		1.0E7	1.0E6	1.0E6	1.0E7
Friction condition		Penalty, 0.1	Penalty, 0.1	Penalty, 0.1	Penalty, 0.1
Total # of elements		209,450 (5 in t_0)	209,450 (5 in t_0)	47,277	209,450 (5 in t_0)
Number of CPUs		108	108	**72**	108
CPU time HH:MM:SS		**40:41:47**	**102:00:30**	**77:40:15**	**29:38:05**

It is important to develop a FE model that is computationally efficient and does not require months of computation time to complete, which keeps acceptable prediction accuracy. Therefore, four different models (Case 1 to Case 4) are implemented with different FE parameters such as

part meshing and mass scaling as summarized in **Table 4.3**. In all these models, five elements in through the thickness direction are used to capture any effects of high shear deformation.

In this section, the FE model developed in the previous section is studied in depth to determine its robustness and what input parameters yield the best prediction results. Also, an insight into FE modeling of µISF process is provided with key focus on element-type selection, artificial simulation acceleration via mass scaling phenomenon in explicit dynamic solver and material characteristics.

4.5.1 Effect of mass scaling

First two cases are meshed using C3D8R 8-noded solid elements with 209,450 elements. Only mass scaling is changed and reduced by an order of magnitude in case 2 when compared with case 1 to study its effect on prediction accuracy and computation time. The comparisons of reactionary forces on the forming tool obtained through experiments and simulations are chosen as a way to validate the accuracy of the developed FE model. Good force prediction is very useful in estimating machine compliances, sheet spring-back and other inaccuracies on the part geometry.

Initially, simulations for benchmark Cases 1 and 2 are performed to study the efficacy of the above developed model for a simple axisymmetric geometry and expected strain levels below AL 1100 material formability in µISF. Part geometry obtained from the two simulations look (on macroscopic scale) exactly same as each other as compared in **Figure 4.15**. However, on further inspection, subtle differences on the deformed mesh and equivalent strain distribution can be clearly observed. In case 1, deformed mesh shows some instances of hourglassing effect on the top surface elements. Additionally, the strain distribution is displaying a so-called ”wavy” nature on the part surface visible in the enlarged **Figure 4.15**(a). Phenomenologically, strain must have an axisymmetric distribution on the part as its geometry is defined as axisymmetric and the

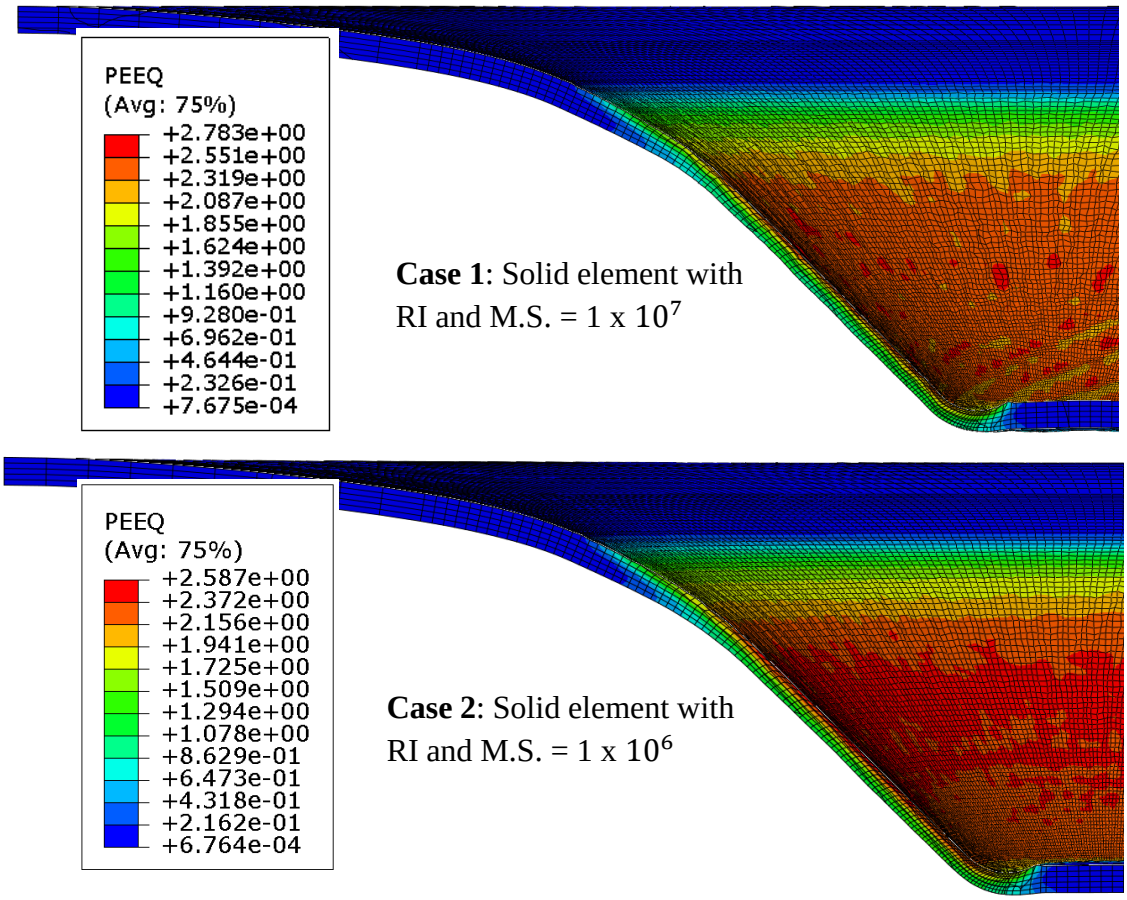

Figure 4.15: Comparison of deformed mesh in cone 45° simulation with different mass scaling factors

material is assumed to be isotropic in the simulation. When the amount of mass scaling is reduced in case 2, these erroneous results start to diminish and show much smoother strain distribution as shown in **Figure 4.15**(b).

On comparing their forming forces, Case 1 results do show promising predictions when compared to the experimental results up to half depth (2200 sec) as shown in **Figure 4.16**. However, numerically obtained force values start to fluctuate after the half depth and deviate from the expected force behavior observed in experiments. When mass scaling is reduced by one order of magnitude in Case 2, the force fluctuations disappear and show good agreement with experimental values. Although the prediction results are improved in case 2, the computation time due to reduced mass scaling also significantly increases from approx. 40 hours to 120 hours.

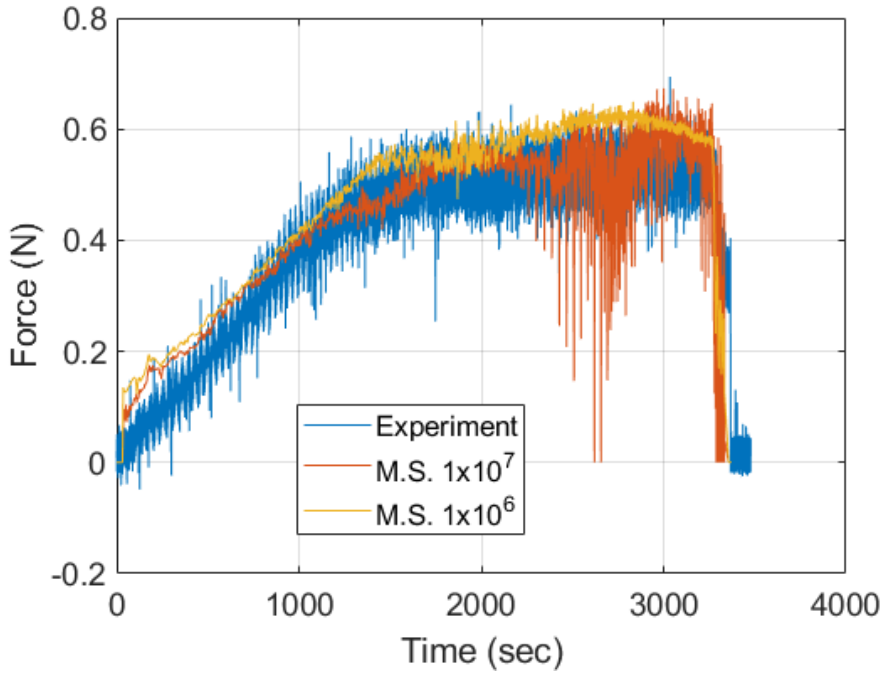

Figure 4.16: Effect of mass scaling on numerically predicted reactionary force values in axial direction

While accelerating finite element analysis of µISF process helps significantly reduce the computation cost, it can have adverse effects on the results if not appropriately utilized. The instantaneous energies stored in the simulation assembly such as kinetic, internal and artificial energies are used as a reliable indicator to check and quantify if any artificial effects have over-powered the results. These energies are defined as below:

- Internal strain energy: Internal strain energy refers to the energy stored in the metal foil due to the plastic deformation achieved during part fabrication process.
- Artificial strain energy: Artificial strain energy is the energy stored in the system by a deformation mode resulting from the excitation of zero-energy degrees of freedom (hourglass effect).
- Kinetic energy: In µISF, it can be defined as the dynamic effect induced in the mesh elements of metal foil due to tool motion.

It is expected that any metal forming process, keeping pragmatic strain rate, must have no dynamic effects and satisfy quasi-static process conditions. To quantify the extent to which this condition is satisfied, a fraction of kinetic energy to internal strain energy is calculated. Ideally, in implicit analysis, this ratio would remain zero. But, in explicit analysis, it should be as minimal as possible - approximately less than 1% as a thumb rule [62]. Additionally, energy due to hourglassing effect induces artifacts in the part geometry. These artifacts are in the form of excessive element distortion and oscillating strain distribution on an axisymmetric geometry as shown in **Figure 4.15**(a). The extent of this effect is quantified by the fraction of artificial to internal strain energy - approximately it should be less than 5-10%.

For the benchmarks Case 1 and Case 2, the evolution of kinetic, internal and artificial strain energies is plotted in **Figure 4.17**. It can be observed from **Figure 4.17**(a) that internal and artificial strain energies for both these cases are arguably the same. However, their kinetic energies greatly differ from each other. Also, there are sudden oscillations in kinetic energy of Case 2 with M.S. = $1\ x\ 10^7$ after half depth of the part. This dynamic effect leads to erroneous prediction of residual stresses and consequently incorrect part geometry as previously compared.

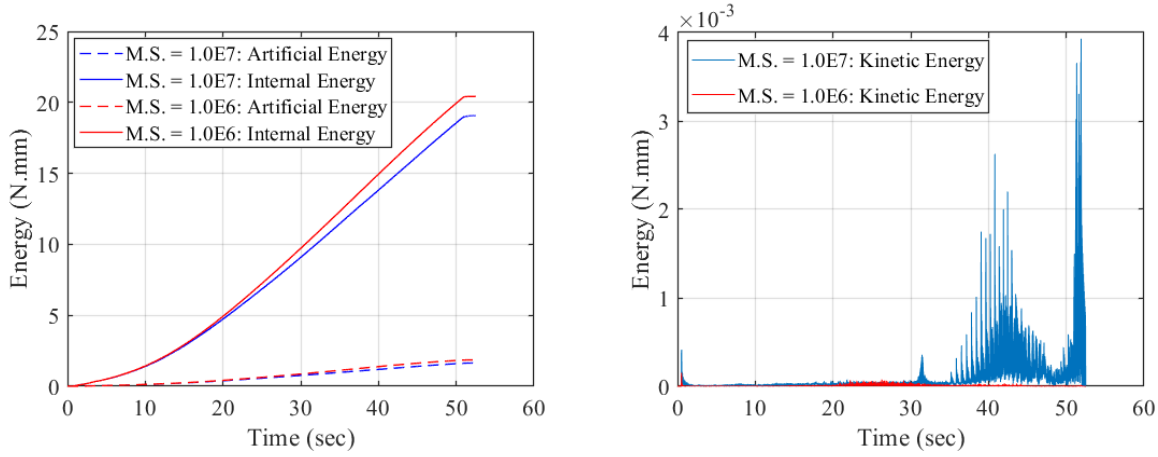

(a) Strain energy (b) Kinetic energy

Figure 4.17: Comparison of kinetic and strain (both internal and artificial) energy of the simulated cone 45° part with M.S. = $1\ x\ 10^6$ and M.S. = $1\ x\ 10^7$

4.5.2 Effect of element-type selection

Evaluating the effect of different element-type technologies in context of µSPIF process is of significant importance in terms of achieving acceptable prediction accuracy in conjunction with lowering computation costs. As previous mentioned, ISF process is known to have very high strain deformations, thousands of deformation steps and triaxial stress state which makes the computation expensive. Therefore, three different element formulations are examined in this sub-section as: (a) Solid element with reduced integration (Cases 1 and 2); (b) Shell element with reduced integration (Case 3); and (c) Solid element with reduced integration and enhanced hourglass control (Case 4).

In the literature, shell element formulation for the simulation of conventional metal forming process such as stamping and deep drawing has proven to produce results with sufficient accuracy. Its formulation is a bit different when compared to solid continuum elements with the assumption that blank's dimension in the thickness direction is substantially lower compared to the other two directions; thereby reducing the number of nodes through the thickness and resulting in much better computation time. Some researchers have even explored its implementation for SPIF process to successfully predict part geometry, sheet springback and thickness distribution ([63], [64]). Despite some success, Moser et al. [59] demonstrated that the prediction of stress triaxiality was relatively poor with shell elements and it was inadequate for the implementation of fracture prediction models. Case 3 simulation in this section is modeled with the shell element (S4R) to examine its effect of prediction accuracy and computation time in case of µSPIF process.

When picking up solid continuum elements for ISF simulations, there are a few more parameters that need to be considered during the modeling process to obtain good solution as: (a) first – order or second – order element type and (b) reduced or full integration scheme.

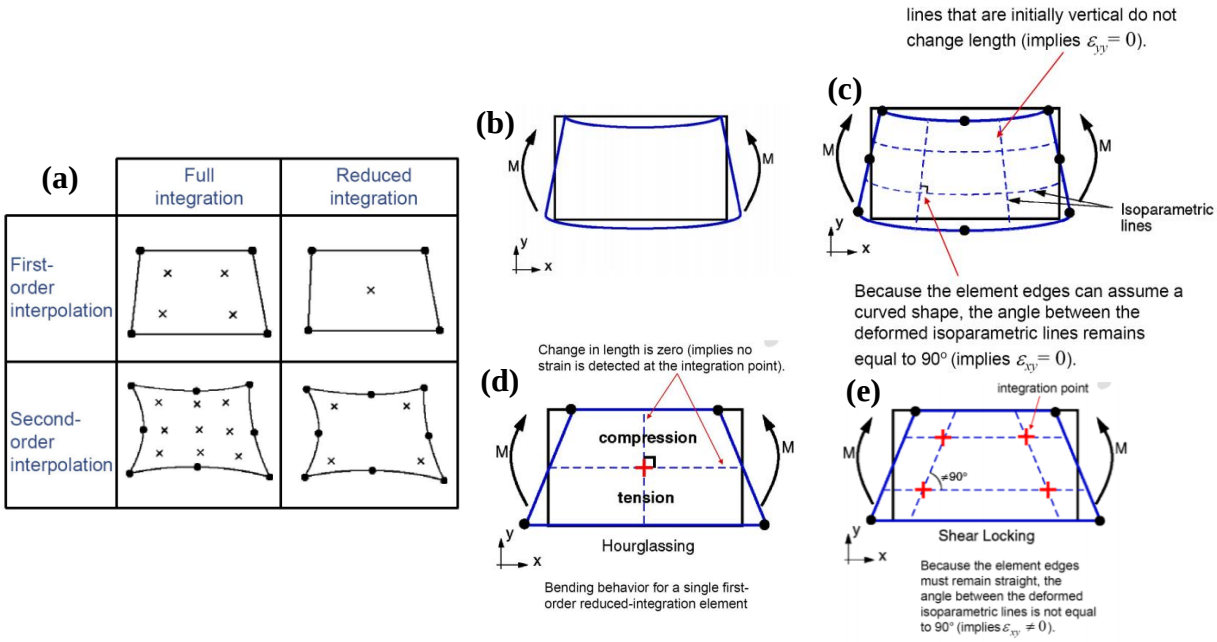

Figure 4.18: (a) Interpretation of full vs. reduced integration elements with First-order and second-order interpolations; (b) a single element subjected to a bending moment; (b) expected element shape after the bending moment is applied; (c) bending behavior recorded by first-order reduced integration element due to hourglassing; and (d) same effect recorded by first order full integration element due to shear locking.

Some of the major considerations while choosing these parameters are as follow:

<u>Element shape – function interpolation:</u>

- While using first – order element with full integration scheme, limited number of integration points are available to capture the intended element shape presented in **Figure 4.18**(c) that gives rise to parasitic shear strain. As seen in **Figure 4.18**(e), the edges are not perpendicular after deformation implying that a non-zero shear strain component exists ($\varepsilon_{xy} \neq 0$). This should not ideally exist in pure bending moment.
- In µSPIF process, blank material wraps around the tool inducing high bending forces in the through thickness direction. Therefore, to avoid aforementioned issue of spurious shear locking, multiple elements (around 5 to 7) are required in thickness to accurately capture any bending effects. Alternatively, second-order element is known to circumvent shear locking by using quadratic shape function and higher number of nodes. But it comes with an enormous

computation time in an already expensive ISF simulation space – generally making it less desirable.

Numerical integration scheme:

- A linear first-order element with reduced integration means that only a single integration point is available at the center to capture any strains – alleviating troubles with shear locking. However, it is possible for this kind of element to go through excessive distortion as shown in **Figure 4.18**(d) and still not record any tensile/compressive strains due to unchanged lengths pointed in the plot. This can lead to very high element distortion and result in spurious zero-energy deformation mode – commonly known as hourglassing effect.
- There are two ways to bypass this issue. Simplest way is to use fine enough mesh to have artificial strain or "hourglass" energy less than 10% of the internal strain energy. Alternatively, an artificial elastic stiffness can be applied to the elements to provide additional restraint to bending and mitigate hourglassing through stiffness hourglass control method. However, if not appropriately used, it could assume material to be much stiffer than intended and increase reactionary forming forces.

Based on the above arguments, reduced integration elements with linear interpolation are used in Cases 1 and 2. Whereas elements in Case 4 are supported with stiffness hourglass control method to analyze how it changes the nature and magnitude of reactionary forming forces. Deformed mesh of the blank for Cases 1 and 2 are shown in **Figure 4.19**. Simulation with shell elements tends to underpredict the equivalent strain distribution. But the best deformed mesh quality is obtained in Case 4 with stiffness control formulation where no sign of "hourglassing" or excessive element distortion can be observed. This can also be confirmed by comparing their kinetic energies as in **Figure 4.21**. Both Cases 3 and 4 have approximately 10 times lower kinetic

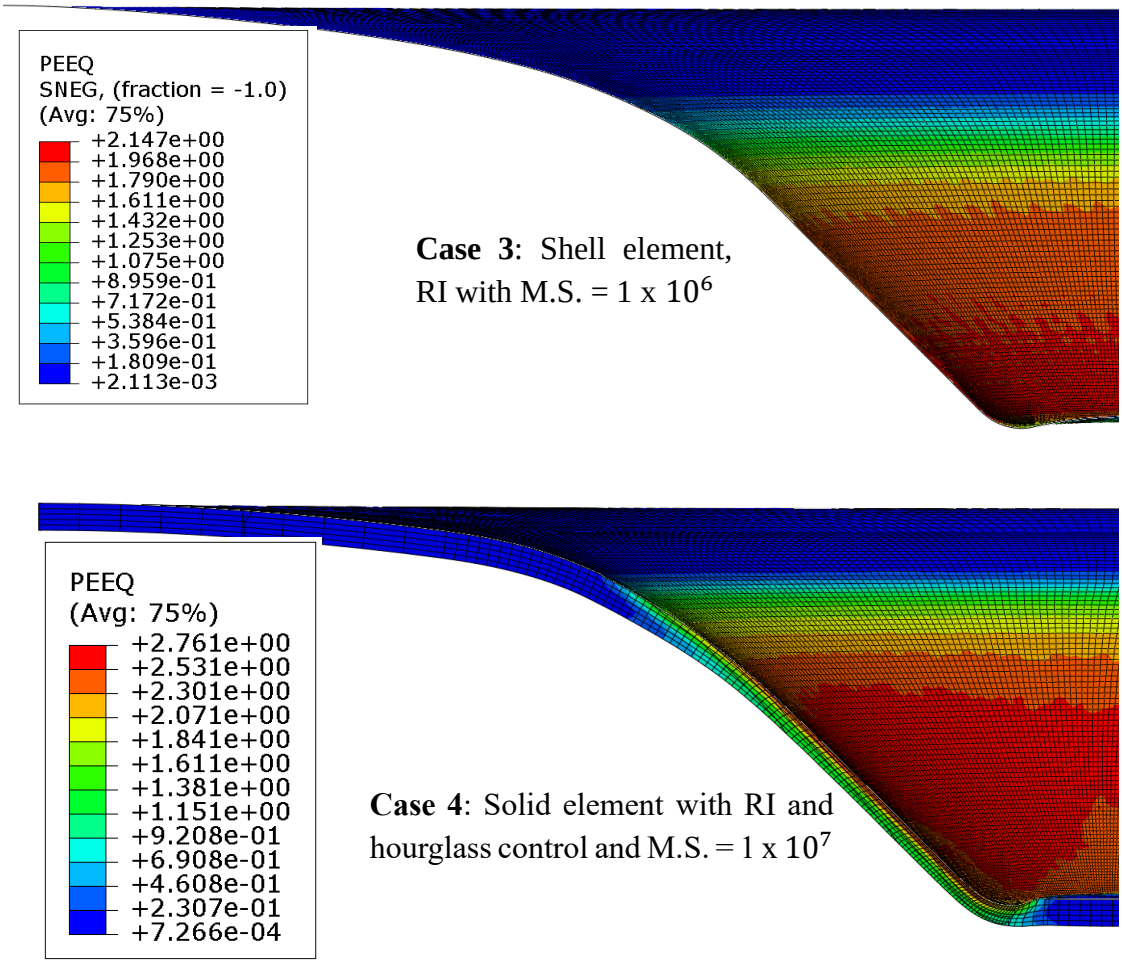

Figure 4.19: Comparison of deformed mesh in cone 45° simulation with different element-type selection

energy when compared with Cases 1 and 2. This demonstrates that elements with hourglass control keeps element deformation in check and does not allow dynamic effects to overtake simulation results. Furthermore, computation time in Case 4 is reduced to 29.6 hours compared to Case 1 time of 40.7 hours where all other parameters except hourglass control are kept same.

Although Case 4 has shown the best deformed mesh and computation efficiency, the force values predicted in this case are slightly higher compared to both Case 1 and the experimental results as shown in **Figure 4.16** and **Figure 4.20**, respectively. This over-prediction can be easily attributed to the hourglassing control formulation implemented that artificially increase the element stiffness and avoid hourglassing.

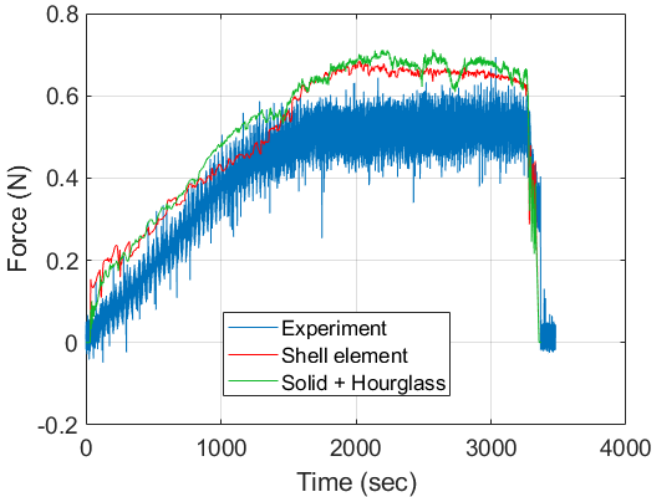

Figure 4.20: Effect of element-type on numerically predicted reactionary forming forces.

Based on all the above benchmarking with cone 45° geometry, it is clearly understood that best FE prediction results can be obtained with parameters used in Case 2 simulation. Forming forces are best predicted with Case 2 and also most numerical/artificial artifacts are successfully avoided from influencing the simulation results. Despite this, one could argue that the force values are still over-predicted when compared against the experimental results. This difference can be attributed to the material characteristics implemented with the assumption of isotropic hardening. It would over-estimate the yield strength in cyclic loading condition that is prominent in incremental forming and henceforth lead to higher force prediction results.

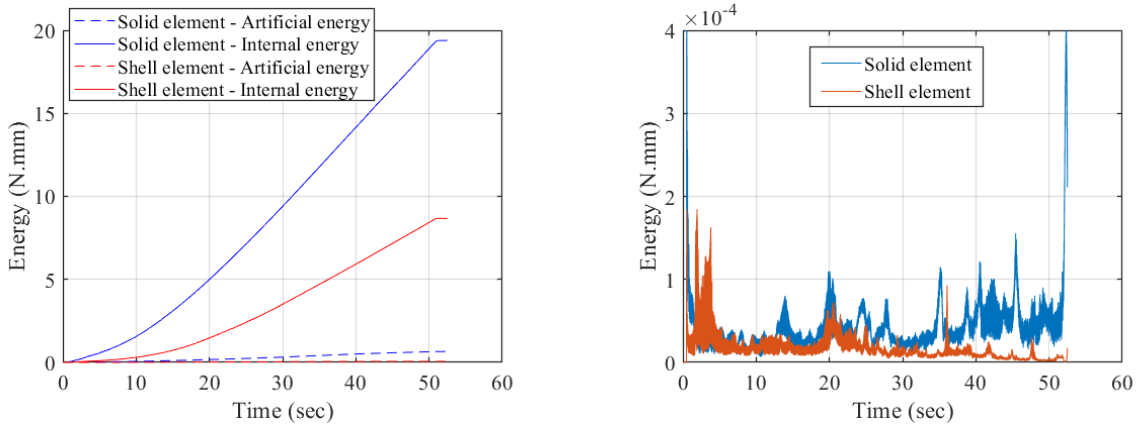

(a) Strain energy (b) Kinetic energy

Figure 4.21: Comparison of kinetic and strain (both internal and artificial) energy of the simulated cone 45° part with different element types

4.6 Implementation of FE Model for High Wall Angled Part

In the previous section, a cone 45° geometry is simulated with 7,500 deformation steps and 257 mm long toolpath. However, when a cone 60° geometry is simulated with same processing parameters, 12,600 deformation steps are required with 326 mm long toolpath. Hence, it is logical to assume that cone 60° simulation will require approximately 1.5 times higher computation time compared to the previous one. Therefore, it will be computationally expensive to simulation it with Case 2 numerical settings which already took 102 hours with the cone 45°.

To find a good trade-off between computation time and accuracy, an FE model for cone 60° geometry is developed and tested with M.S. = 1 x 10^7 similar to Case 1. Even here, it is expected to have some wrinkles on the geometry due to high mass scaling as shown in **Figure 4.22**. It took total computation time of 55 hours and 10 minutes for this FE model to converge on 108 CPUs available at University of Michigan – Ann Arbor computer cluster. Reducing mass scaling like in the previous section will require substantially higher computation time and hourglass control might induce artifacts making the results less reliable. Moser et al. [59] suggested that applying mass damping in combination with stiffness-based hourglass control to the blank material was a useful technique in avoiding the excessive element distortion when high mass scaling was used. Also, it helps eliminate any spurious oscillations observed in the predicted force values, which improves the simulation stability and robustness. Artificial damping in FE model is generally applied through Rayleigh damping technique:

$$\xi_i = \frac{\alpha_R}{2\omega_i} + \frac{\beta_R \omega_i}{2} \tag{4.9}$$

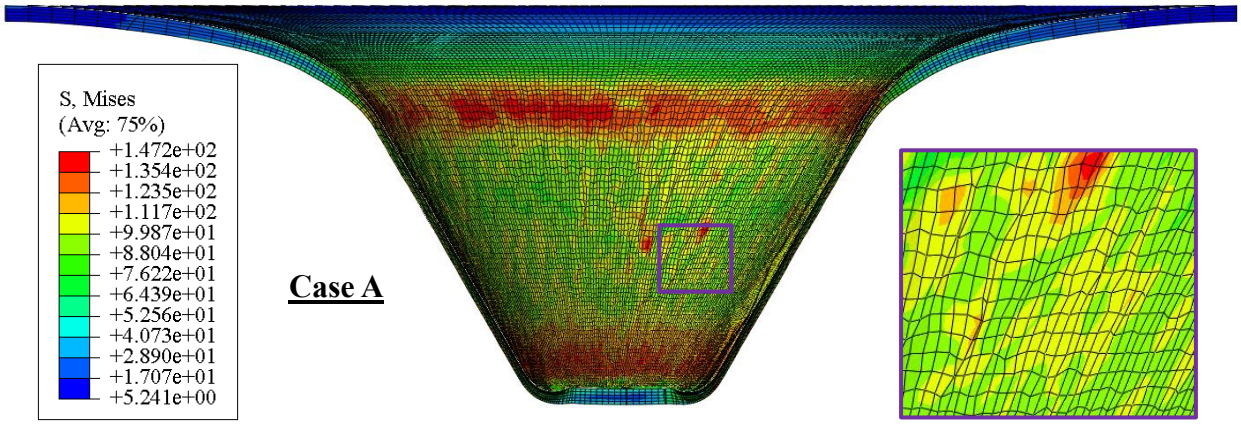

Figure 4.22: Simulated cone 60 geometry with reduced integration linear element and M. S. = $1x10^7$

where, α_R is the mass damping coefficient, β_R is the stiffness damping coefficient, ω_i is the natural frequency of the blank at i^{th} vibrational mode and ξ_i is the fraction of damping used in the simulation.

Stiffness damping is known to significantly increase the total computation time and therefore only mass damping is used in the simulations. Natural frequency of the modeled blank is calculated through Abaqus\Standard eigen value analysis. The first natural frequency is found to be approx. 27,848 Hz in its natural mass scale. As ISF simulations are run at M.S. = 1 x 10^7, this natural frequency is adjusted to the scaled material density using Equation (4.10) to 8.8 Hz.

$$\omega_i \propto \frac{1}{\sqrt{\rho\ (\text{density})}} \tag{4.10}$$

For a low fraction of damping at 12%, the Rayleigh mass damping coefficient is then calculated as:

$$\alpha_R = \xi_i(2\omega_i) = 0.12 * (2 * 2 * \pi * 8.8) = 13.2 \tag{4.11}$$

Two FE simulations for cone 60° geometry are run using this Rayleigh mass damping coefficient – one with stiffness-based hourglass control and the other without it. In total, three

simulations run for this geometry with their numerical parameters are listing in **Table 4.4**. It can be observed from the table that Rayleigh damping increases the total computation time by 18.5%.

Table 4.4: Comparison of element type and corresponding computation time taken for cone 60° simulations

		Case A	Case B	Case C
Targeted part shape		Truncated cone shape with **60º wall angle** ABAQUS\Explicit		
Material model	Hardening Law	Holloman type, isotropic	Holloman type, isotropic	Holloman type, isotropic
	Yield locus	von Mises	von Mises	von Mises
Element type		C3D8R	C3D8R + Rayleigh mass damping	C3D8R + Rayleigh mass damping + hourglass control
Mass scaling factor		1.0E7	1.0E7	1.0E7
Friction condition		Penalty, 0.1	Penalty, 0.1	Penalty, 0.1
Total # of elements		209,450 (5 in t_0)	209,450 (5 in t_0)	209,450 (5 in t_0)
Number of CPUs		108	108	108
CPU time HH:MM:SS		**55:10:12**	**65:32:21**	**51:20:41**

When the deformed mesh for both Cases A and B are compared, only a marginal difference in final mesh quality is observed. But, due to the nature of mass damping that is analogous to forming the part submerged in a high viscous fluid, blank material starts to accumulate ahead of the tool and a bulge at the part bottom is developed as seen in **Figure 4.23**(a). This is clearly a numerical artifact induced by Rayleigh's mass damping technique and not observed in any of the experimental geometries. Predicted axial force values from all the three listed FE models and their corresponding experimental results are compared in **Figure 4.24**. It can be seen that material accumulation increases the predicted reactionary forces on the tool and therefore it starts to significantly deviate from the experimental values.

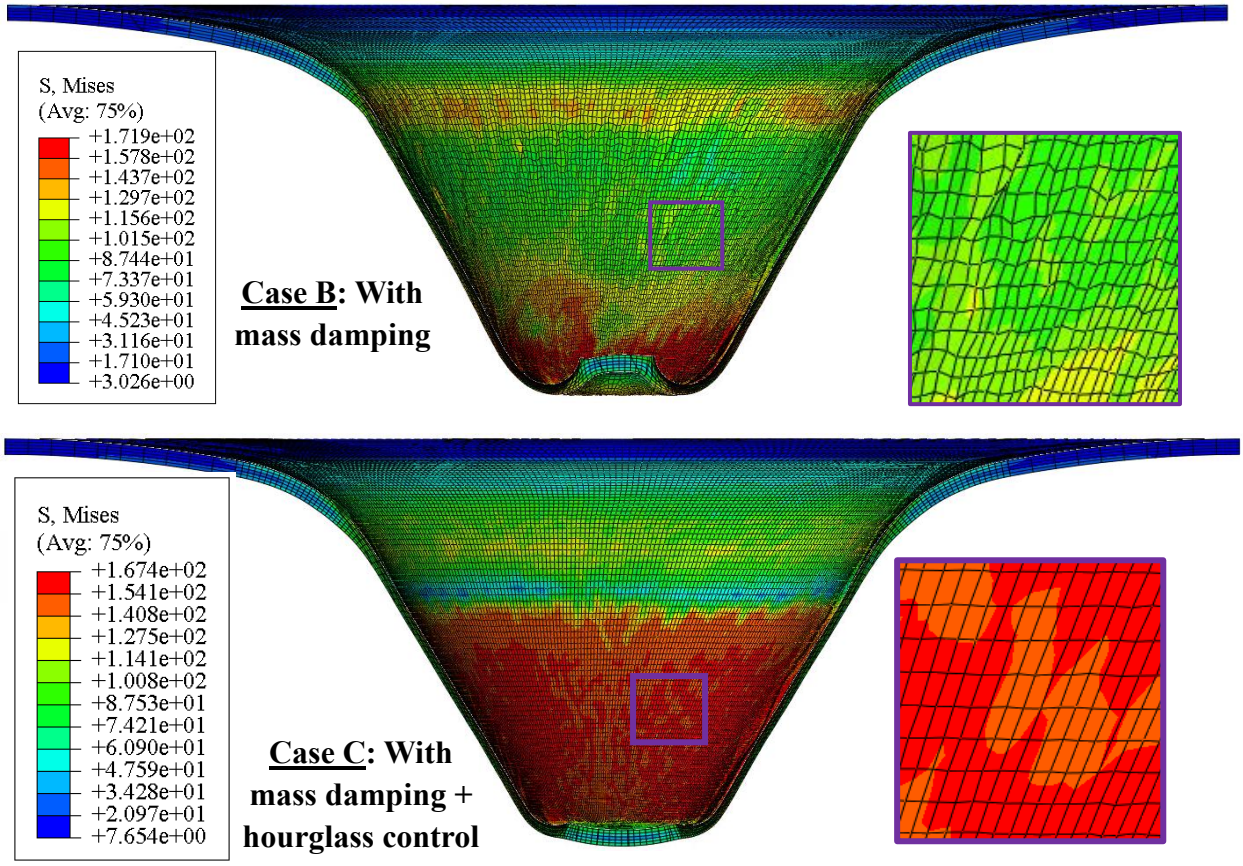

Figure 4.23: Comparison of simulated cone 60° geometry with only mass damping applied and with both mass damping and hourglass control

In Case C, the geometry is simulated with both mass damping and hourglass control with least amount of computation time. Also, similar to cone 45°, this case has the best mesh quality and smooth stress distribution. However, it also has an unexpected downward bulge at the part bottom as seen in **Figure 4.23**(b) that cannot be explained by a physics-based mechanical model. In force comparison, Case C predicted the axial force value around 40 – 50% higher compared to the experimental results and therefore is clearly not a good numerical modeling strategy despite having better computational efficiency. Case A, without any mass damping and hourglass control, does have some hourglassing issues but also provides the best force prediction results with comparable computation time to the cases in cone 45° geometry.

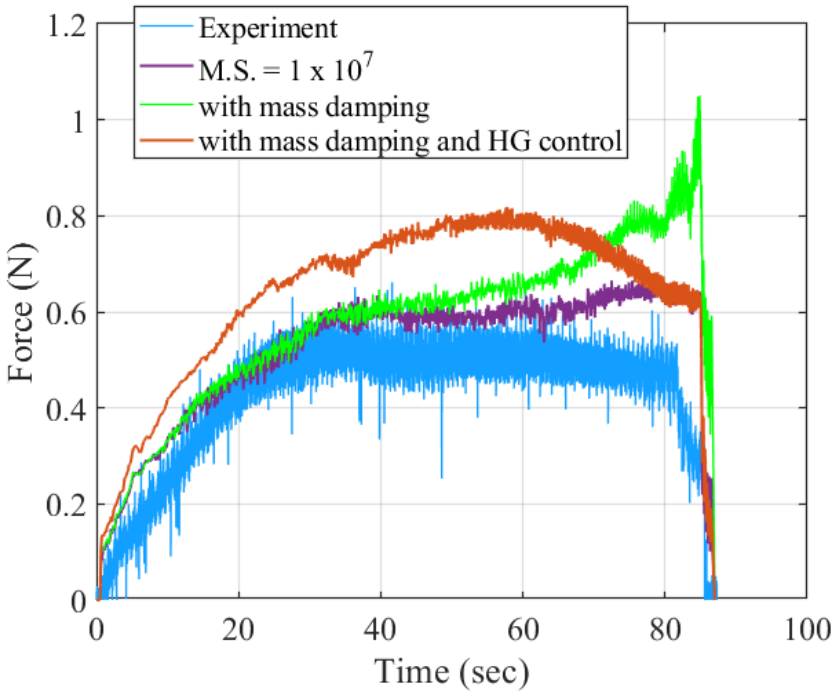

Figure 4.24: Comparison of forming forces in axial direction predicted using all the three FE models for cone 60° geometry and its experimental results.

4.7 Summary and Conclusions

The main objective of this chapter was to develop a finite element prediction model for µISF process that does not require months of computation time and can still be very helpful in understanding the underlying process mechanics. After optimizing input parameters for the model and characterizing behavior AL 1100 under large strain deformation, some of the major take-away from this chapter are as follow:

- Constitutive material model with Holloman's strain hardening law and isotropic-hardening provides much more realistic distribution of effective plastic strain compared to that obtained with Voce law.
- While benchmarking with cone 45° geometry, it is shown that the FE model with M.S. = 1 x 10^6 converges best prediction results with "good enough" mesh quality. Increasing the mass scaling leads to wrinkles in the geometry due to increase in system kinetic energy and stiffness based hourglass control provides over-predicted force values.
- Multiple mass scaling factors and element types are tested in FE simulation of the above-mentioned case. Most optimum results are obtained with: (a) solid continuum element with reduced integration and (b) M.S. = 1 x 10^6.
- For a high wall angled part of cone 60°, other suggested techniques such as Rayleigh mass damping in combination with hourglass control is tested to suppress any spurious force oscillations and mesh deformation. But best results are still obtained with aforementioned model. Rayleigh mass damping led to material accumulation at the part bottom making it less desirable whereas, hourglass control gave an unexpected upside-down bulge with very high axial force prediction when compared with experimental results.

Chapter 5
Summary and Future Work

5.1 Summary and Conclusions

With the increasing demand for rapid manufacturing of personalized sheet metal parts in medical, automotive and aerospace industries, incremental sheet forming (ISF) provides a unique solution to meet these demands with great time and cost efficiency. However, there are some unique challenges in ISF that needs to be addressed before getting adopted in manufacturing industry. Furthermore, this process has capability to produce parts at both macro-scale for automotive/aerospace industries and micro-scale for medical/micro-electronics industries.

In this disseration, a few major challenges in both micro and macro-scale ISF are identified based on an extensive literature survey such as: (a) inferior part accuracy; (b) unconventional part formability; (c) limited guidelines to develop numerical prediction models; and (d) lack of understanding in deformation mechanics. These challenges are later addressed through comprehensive experimental and numerical investigations in Chapter #2, #3 and #4. Some of the major contributions and conclusions from these three chapters are listed below:

Chapter #2: In this chapter, μISF process performance is quantified in various aspects such as required forming forces, part's geometric accuracy and material formability by experimentally fabricating truncated cone geometry on AL1100 and AL5052 materials. Some of the major takeaway from this part of research are as follow:

- An experimental setup is developed in-house to perform µSPIF experiments and obtain repeatable and reliable results. It is integrated with a force sensor and a LabVIEW software interface to mimic a table-top CNC milling machine to synchronously move the tool head in x, y and z directions.
- A parametric analysis of different processing parameters reveals that forming forces significantly increase in both axial and radial directions with higher step size and only moderately increase with higher tool-tip diameter.
- Cross – sectional profiles of experimentally produced cone shaped parts are compared with their designed geometries to quantify the extent of geometric accuracy obtained through µSPIF process. In general, a deviation of 80 to 120 µm is obtained in most cases that can be attributed to the combination of machine compliance, tool deflection and sheet springback.
- Material formability of AL 5052-H19 material is quantified in terms of the maximum wall angled part that can be successfully formed using µSPIF process. As it is difficult to visually confirm the crack initiation, it is monitored through any sudden drop in forming forces.
- The parametric analysis shows that decrease in step size results in high strain hardening leading to fracture at low strain values. On the other hand, large tool size helps suppress any dynamic bending of the sheet and induce uniform deformation along neighboring grains leading to better part formability.
- Finally, it is demonstrated that optimizing toolpath for step size and tool diameter in combination with offline machine compliance correction can significantly improve part accuracy and material formability in µSPIF process.

Chapter #3: In this chapter, an experimental investigation of TPIF process is conducted specifically for the fabrication of automotive and aerospace application parts using AL 7075 alloy.

Firstly, an experimental setup is custom – built on a horizontal CNC machine with a backup die and a spindle mounted force sensor for continuous feedback. Three major research gaps are identified through literature survey as: (a) Geometric accuracy of the parts formed by TPIF process is inferior to that of hydroforming process; (b) Toolpath generation in TPIF or DSIF is an iterative process to optimize material squeeze factor. It is required to avoid "degenerative SPIF" forming and maintain uniform contact between the support die/tool and the blank material; and (c) Research articles report the value of this parameter as programmed in the toolpath. However, effective squeeze factor obtained in experiments could be considerably different than its programmed value due to machine compliances and tool deflection. This effect must be considered while developing FE model to get accurate predictions. Therefore, solutions for the above three research gaps are proposed in this chapter and some of the conclusions drawn from this study is listed below:

- A mathematical formulation is proposed to relate programmed and effective squeeze factors based on forming forces and pre-determined machine compliance. It is experimentally validated for three different geometries, including cone 45°, cone 67° and heart shape part.
- When cone 67° parts are produced with 40% programmed squeeze factor, an effective squeeze of only 2.3% is obtained in the experiments. FE model for the same shows that no result can be obtained when it is simulated with $SF_p = 40\%$ due to severe element distortion. However, the accurate prediction of forming forces is achieved when the same model is run with $SF_p = 2.3\%$ demonstrating its importance for FE modeling in TPIF and DSIF processes.
- Geometric accuracy of the TPIFed parts such as truncated cones and heart shape geometry are significantly influenced by the material squeeze factor used in the toolpath. Higher squeeze factor helps reduce sheet springback and improves geometric accuracy in the wall region.

However, it also accumulates material ahead of the tool and creates an unwanted bulge in the bottom region.

- To reduce the bulging and improve part accuracy, a multi-stage TPIF strategy is proposed for heart shape part. In stage 1, material is formed with $SF_p = 0\%$ in out-to-in direction without accumulating much material. Then in stage 2, the same part is re-formed in in-to-out direction with $SF_p = 15\%$ to flatten any asperities and redistribute the surface material.
- This strategy is shown to have much better geometric accuracy when compared to single stage TPIF and similar to hydroformed part. If the base region is neglected, multi-stage TPIF yields geometric accuracy even better than that is seen in hydroformed part.
- The formability analysis of AL 7075 alloy in TPIF shows that positive effective squeeze factor induces higher compressive stress state and helps suppress any crack growth. Therefore, better material formability is achieved with high squeeze factor in case of cone 67°. Parts consistently developed fracture along circumferential direction when formed with $SF_p = 0\%$ whereas it was successfully formed with $SF_p = 40\%$.
- In the case of heart shape, part formability is observed to be much more dependent on bulge formation by smaller step size or higher squeeze. Here, as the bulge size grew, it induced an additional tensile force along the circumferential direction on the corner rib and led to an interesting mode of failure that was previously not observed in ISF process.
- A fuel cover part is produced in the end that has intricate features using TPIF and a novel multi-frame SPIF process to demonstrate the robustness and capabilities of ISF.

Chapter #4: The main objective of this chapter is to develop a finite element model for incremental micro-forming process that can provide prediction results with acceptable accuracy and computation time. It is important to develop a cost-efficient and accurate prediction model to

understand the underlying process mechanics, avoid part failure and enhance its performance. Various FE modeling techniques are available in literature for conventional deep drawing and hydroforming processes. However, these models do not meet the required accuracy standards due to the complex stress states and non-linear strain paths involved in µISF. Only a handful of studies are available in literature for FE modeling of µISF with concrete guidelines on choosing constitutive material model and numerical parameters such as element-type formulations, numerical integration schemes, enforcing tool-sheet contact condition and implicit vs. explicit solver. Some of the major contributions of this chapter are as follow:

- A finite element model for µISF process is developed using truncated cone geometry with 45° wall angle and aluminum 1100 material properties.
- Tensile tests are performed on 50 µm thick aluminum foil in rolling, transverse and diagonal directions at a quasi-static strain rate of $1 * 10^{-3}$ per second. Stress-strain curves along all three directions are found to be approximately same and therefore the material is assumed isotropic in nature.
- Further loading – unloading cycles are performed in tensile tests at strain values of 2.5% and 5% to obtain better estimate of elastic modulus and avoid effects of initial slack in the sample.
- FE results show that constitute material model with Holloman's strain hardening law and isotropic-hardening of yield locus provides much more realistic distribution of plastic strain on the specimen compared to Voce hardening law.
- Techniques of mass/velocity scaling are successfully utilized to artificially accelerate the simulation convergence without compromising on prediction accuracy. For cone 45°, multiple mass scaling factors are tested, and the best force prediction is achieved with M.S. = 1 x 10^6.

Mass scaling higher than this led to sudden jumps in the force values and “wrinkles” on the part geometry due to increased kinetic energy.

- Though FE model with M.S. = 1 x 10^7 and addition of stiffness-based hourglass control provided “best quality” deformed mesh and least computation time, it applied artificial elastic stiffness to the elements to reduce hourglassing that led to over-prediction of forming forces.
- Based on the analysis, it is recommended that FE model for µISF should be developed with solid continuum element with reduced integration and without any hourglass control. A simple material model with Holloman hardening curve, von-Mises yield criterion and isotropic hardening can provide force prediction results with acceptable accuracy when compared with experimental results.

For higher wall angle geometries that go through large strain deformation, some other techniques are also suggested in literature such as Rayleigh mass damping in combination with hourglass control to suppress any oscillations in forming forces and reducing hourglassing effect. When these techniques are tested for cone 60° geometry, some of the observations are as follow:

- Firstly, modal analysis is performed to obtain fundamental vibrational frequency of the specimen that is needed to implement Rayleigh mass damping. When included in the model, it led to high material accumulation and a big bulge at the bottom of the part.
- Similarly, an unconventional upside-down bulge is developed on the part bottom when the same mass damping is applied in combination with stiffness-based hourglass control.
- Both the above phenomena are labeled to be numerical artifacts as no such bulge is observed during experimental fabrication of cone 60° part.

- Therefore, it is recommended to use the same model as of cone 45° for high wall angle part too, perhaps with finer mesh if needed, to achieve good prediction results and avoid any numerical artifacts over-powering the final results.

5.2 Future Work

In the final section, some future work is proposed to improve the understanding and applicability of incremental forming process at both micro and macro scales. The proposed work is divided into three classes: (a) Experimental work; (b) improvement of FE modeling; and (c) the development of analytical prediction models. Details for all three classes are presented below:

5.2.1 Experimental analysis

Comprehensive experimental analysis of micro-scale part production through μSPIF process is presented in Chapter #2. It is concluded in Section 2.5.1 that most of the geometric inaccuracy in any part is contributed by machine compliance and tool deflection that is directly dependent on reactionary forces. So, if these forces are known priori, predesigned toolpath can be corrected for all these errors and the part accuracy can be significantly improved. Also, the effect of grain size to feature size must be further explored to quantify the strength of final part.

In Chapter #3, the importance of achieving positive material squeeze is studied and shown how it can differ in experiments from its value programmed in the toolpath. The value of effective material squeeze can be successfully determined based on its corresponding forming forces. Therefore, developing a real-time toolpath correction system based on in-situ force measurement will help determine the state of material squeeze. If no squeeze is achieved, an open architecture CNC machine can allow to perform toolpath correction by modifying the reference position command through an empirical model and fabricate part with much better geometric accuracy. In

addition, a novel multi-stage TPIF toolpath strategy is proposed to reduce bulge and improve accuracy. However, further toolpath optimization for process parameters such as step size, tool diameter and squeeze factor is needed to reap the full benefits on this technique.

5.2.2 Improvement of FE modeling

While developing the finite element model in Chapter #4, certain assumptions related to material properties are made to simplify the model and still achieve acceptable prediction accuracy. However, some of the assumptions come at a cost of reduced accuracy. Following are some of those issues and a path for further improvement:

- To improve the constitutive material model:
    - Reduction of yield stress in reverse loading due to Bauschinger effect is ignored while using isotropic-hardening in constitutive material modeling. This leads to over-prediction of yield stress and therefore forming forces too.
    - A mixed kinematic-isotropic hardening law needs to be trained through further material testing and implemented in FE model of incremental forming for better predictions.
- Creating a robust FE model for any geometry:
    - Arbitrary Lagrangian-Eulerian (ALE) adaptive meshing could help mitigate the element distortion. However, in Abaqus/Explicit, ALE is currently not available for multi-core analysis that needs to be implemented by future modelers.
    - Most studies including this one use either shell or solid continuum elements for FE simulations of ISF. However, usage of continuum shell elements is still very sparse. It can help reduce the computation time if appropriate formulation is implemented.

5.2.3 Development of analytical prediction model

A robust analytical modeling of any metal forming process provides a path to fabricate complex shaped parts as per the required standards in minimum iterations. It helps better understand the process mechanics, avoid part failures and improve process performance. However, most existing analytical models for incremental forming are applicable to only macro-scale SPIF. In literature, some regression models are available to predict forming forces, thickness distribution and sheet springback that are either not accurate enough or work in a narrow window of process parameters and material properties. They need to be further expanded for micro-scale parts and for TPIF process. Analytical models tend to be much less accurate compared to finite element models. But they can still provide important process specific information in negligible computation time. Also, these models can be directly used for both offline and real-time feedback control systems to make ISF process much more desirable and acceptable in industries for rapid manufacturing.

Bibliography

[1] J. C. Carr, W. Richard Fright, and R. K. Beatson, "Surface interpolation with radial basis functions for medical imaging," *IEEE Trans. Med. Imaging*, vol. 16, no. 1, pp. 96–107, 1997.

[2] K. M. Schebesch, J. Höhne, H. G. Gassner, and A. Brawanski, "Preformed titanium cranioplasty after resection of skull base meningiomas – A technical note," *J. Cranio-Maxillofacial Surg.*, vol. 41, no. 8, pp. 803–807, Dec. 2013.

[3] G. Ambrogio *et al.*, "Experimental investigation of the mechanical performances of titanium cranial prostheses manufactured by super plastic forming and single-point incremental forming," *Int. J. Adv. Manuf. Technol. 2018 985*, vol. 98, no. 5, pp. 1489–1503, Jun. 2018.

[4] J. Cao, Y. Huang, N. Reddy, R. Malhotra, and Y. Wang, "Incremental sheet metal forming: advances and challenges," *Int. Conf. …*, vol. 3, no. c, pp. 1–16, 2008.

[5] N. V. Reddy, R. Lingam, and J. Cao, "Incremental Metal Forming Process in Manufacturing," pp. 411–449, 2015.

[6] N. V Reddy and R. Lingam, "Double Sided Incremental Forming: Capabilities and Challenges," *J. Phys. Conf. Ser.*, vol. 1063, no. 1, p. 012170, Jul. 2018.

[7] X. M. Lai, M. W. Fu, and L. F. Peng, "Sheet Metal Meso- and Microforming and Their Industrial Applications," *Sheet Met. Meso- Microforming Their Ind. Appl.*, Aug. 2018.

[8] T. Obikawa, S. Satou, and T. Hakutani, "Dieless incremental micro-forming of miniature

shell objects of aluminum foils," *Int. J. Mach. Tools Manuf.*, vol. 49, no. 12–13, pp. 906–915, Oct. 2009.

[9] T. OBIKAWA, T. HAKUTANI, T. SEKINE, S. NUMAJIRI, T. Matsumura, and M. Yoshino, "Single-point incremental micro-forming of thin shell products utilizing high formability," *J. Adv. Mech. Des. Syst. Manuf.*, vol. 4, no. 6, pp. 1145–1156, 2010.

[10] D. Y. Seong, M. Z. Haque, J. B. Kim, T. B. Stoughton, and J. W. Yoon, "Suppression of necking in incremental sheet forming," *Int. J. Solids Struct.*, vol. 51, no. 15–16, pp. 2840–2849, Aug. 2014.

[11] E. Leszak, "Apparatus and Process for Incremental Dieless Forming, Published September 19, 1967," Aug. 1967.

[12] J. Jeswiet, "Asymmetric Incremental Sheet Forming," *Adv. Mater. Res.*, vol. 6–8, pp. 35–58, 2005.

[13] J. Asghar, R. Lingam, E. Shibin, and N. V. Reddy, "Tool path design for enhancement of accuracy in single-point incremental forming," *Proc. Inst. Mech. Eng. Part B J. Eng. Manuf.*, vol. 228, no. 9, pp. 1027–1035, 2014.

[14] M. S. Shim and J. J. Park, "The formability of aluminum sheet in incremental forming," *J. Mater. Process. Technol.*, vol. 113, no. 1–3, pp. 654–658, 2001.

[15] Y. Saotome and T. Okamoto, "An in-situ incremental microforming system for three-dimensional shell structures of foil materials," *J. Mater. Process. Technol.*, vol. 113, no. 1–3, pp. 636–640, 2001.

[16] T. Obikawa and M. Hayashi, "Ultrasonic-assisted incremental microforming of thin shell pyramids of metallic foil," *Micromachines*, vol. 8, no. 5, p. 142, May 2017.

[17] M. Beltran, R. Malhotra, A. J. Nelson, A. Bhattacharya, N. V. Reddy, and J. Cao,

"Experimental Study of Failure Modes and Scaling Effects in Micro-Incremental Forming," *J. Micro Nano-Manufacturing*, vol. 1, no. 3, p. 031005, 2013.

[18] J. R. Duflou, H. Vanhove, J. Verbert, J. Gu, I. Vasilakos, and P. Eyckens, "Twist revisited: Twist phenomena in single point incremental forming," *CIRP Ann. - Manuf. Technol.*, vol. 59, no. 1, pp. 307–310, 2010.

[19] M. Skjoedt, M. H. Hancock, and N. Bay, "Creating Helical Tool Paths for Single Point Incremental Forming," *Key Eng. Mater.*, vol. 344, pp. 583–590, Jul. 2007.

[20] S. Kobayashi, I. K. Hall, and E. G. Thomsen, "A theory of shear spinning of cones," *J. Manuf. Sci. Eng. Trans. ASME*, vol. 83, no. 4, pp. 485–494, 1961.

[21] D. Young and J. Jeswiet, "Wall thickness variations in single-point incremental forming," *Proc. Inst. Mech. Eng. Part B J. Eng. Manuf.*, vol. 218, no. 11, pp. 1453–1459, 2004.

[22] R. Ben Hmida, S. Thibaud, A. Gilbin, and F. Richard, "Influence of the initial grain size in single point incremental forming process for thin sheets metal and microparts: Experimental investigations," *Mater. Des.*, vol. 45, pp. 155–165, Mar. 2013.

[23] G. Ambrogio, V. Cozza, L. Filice, and F. Micari, "An analytical model for improving precision in single point incremental forming," *J. Mater. Process. Technol.*, vol. 191, no. 1–3, pp. 92–95, 2007.

[24] G. Ambrogio, I. Costantino, L. De Napoli, L. Filice, L. Fratini, and M. Muzzupappa, "Influence of some relevant process parameters on the dimensional accuracy in incremental forming: A numerical and experimental investigation," *J. Mater. Process. Technol.*, vol. 153–154, no. 1–3, pp. 501–507, 2004.

[25] R. Aerens, P. Eyckens, A. Van Bael, and J. R. Duflou, "Force prediction for single point incremental forming deduced from experimental and FEM observations," *Int. J. Adv.*

Manuf. Technol., vol. 46, no. 9–12, pp. 969–982, Feb. 2010.

[26] A. Bansal, R. Lingam, S. K. Yadav, and N. Venkata Reddy, "Prediction of forming forces in single point incremental forming," *J. Manuf. Process.*, vol. 28, pp. 486–493, Aug. 2017.

[27] M. B. Silva, P. S. Nielsen, N. Bay, and P. A. F. Martins, "Failure mechanisms in single-point incremental forming of metals," *Int. J. Adv. Manuf. Technol.*, vol. 56, no. 9–12, pp. 893–903, 2011.

[28] J. Jeswiet, F. Micari, G. Hirt, A. Bramley, J. Duflou, and J. Allwood, "Asymmetric Single Point Incremental Forming of Sheet Metal," *CIRP Ann. - Manuf. Technol.*, vol. 54, no. 2, pp. 88–114, 2005.

[29] J. R. Duflou, H. Vanhove, J. Verbert, J. Gu, I. Vasilakos, and P. Eyckens, "Twist revisited: Twist phenomena in single point incremental forming," *CIRP Ann. - Manuf. Technol.*, vol. 59, no. 1, pp. 307–310, 2010.

[30] J. M. Allwood, O. Music, A. Raithathna, and S. R. Duncan, "Closed-loop feedback control of product properties in flexible metal forming processes with mobile tools," *CIRP Ann. - Manuf. Technol.*, vol. 58, no. 1, pp. 287–290, 2009.

[31] J. Verbert, R. Aerens, H. Vanhove, E. Aertbeliën, and J. R. Duflou, "Obtainable Accuracies and Compensation Strategies for Robot Supported SPIF," *Key Eng. Mater.*, vol. 410–411, pp. 679–687, 2009.

[32] A. K. Behera, J. Verbert, B. Lauwers, and J. R. Duflou, "Tool path compensation strategies for single point incremental sheet forming using multivariate adaptive regression splines," *CAD Comput. Aided Des.*, vol. 45, no. 3, pp. 575–590, 2013.

[33] A. Fiorentino, G. C. Feriti, C. Giardini, and E. Ceretti, "Part precision improvement in incremental sheet forming of not axisymmetric parts using an artificial cognitive system,"

J. Manuf. Syst., vol. 35, pp. 215–222, Apr. 2015.

[34] J. Shin, A. Bansal, R. Chang, A. Taub, and M. Banu, "Process planning for precision incremental forming of complex parts," in *AIP Conference Proceedings*, 2019, vol. 2113.

[35] A. Attanasio, E. Ceretti, and C. Giardini, "Optimization of tool path in two points incremental forming," *J. Mater. Process. Technol.*, vol. 177, no. 1–3, pp. 409–412, 2006.

[36] A. Attanasio, E. Ceretti, C. Giardini, and L. Mazzoni, "Asymmetric two points incremental forming: Improving surface quality and geometric accuracy by tool path optimization," *J. Mater. Process. Technol.*, vol. 197, no. 1–3, pp. 59–67, Feb. 2008.

[37] A. Göttmann, M. Korinth, V. Schäfer, B. T. Araghi, M. Bambach, and G. Hirt, "Manufacturing of Individualized Cranial Implants Using Two Point Incremental Sheet Metal Forming," in *Future Trends in Production Engineering*, Springer Berlin Heidelberg, 2013, pp. 287–295.

[38] H. Lu, M. Kearney, C. Wang, S. Liu, and P. A. Meehan, "Part accuracy improvement in two point incremental forming with a partial die using a model predictive control algorithm," *Precis. Eng.*, vol. 49, pp. 179–188, 2017.

[39] L. Filice, L. Fratini, and F. Micari, "Analysis of material formability in incremental forming," *CIRP Annals - Manufacturing Technology*, vol. 51, no. 1. Hallwag Publishing Ltd, pp. 199–202, 01-Jan-2002.

[40] A. Bhattacharya, K. Maneesh, N. Venkata Reddy, and J. Cao, "Formability and Surface Finish Studies in Single Point Incremental Forming," *J. Manuf. Sci. Eng.*, vol. 133, no. 6, p. 061020, 2011.

[41] W. C. Emmens and A. H. van den Boogaard, "An overview of stabilizing deformation mechanisms in incremental sheet forming," *J. Mater. Process. Technol.*, vol. 209, no. 8, pp.

3688–3695, Apr. 2009.

[42] K. Jackson and J. Allwood, “The mechanics of incremental sheet forming,” *J. Mater. Process. Technol.*, vol. 209, no. 3, pp. 1158–1174, 2009.

[43] J. Smith, R. Malhotra, W. K. Liu, and J. Cao, “Deformation mechanics in single-point and accumulative double-sided incremental forming,” *Int. J. Adv. Manuf. Technol.*, vol. 69, no. 5–8, pp. 1185–1201, 2013.

[44] M. B. Silva, M. Skjoedt, A. G. Atkins, N. Bay, and P. A. F. Martins, “Single-point incremental forming and formability—failure diagrams,” *J. Strain Anal. Eng. Des.*, vol. 43, no. 1, pp. 15–35, Jan. 2008.

[45] M. B. Silva, M. Skjoedt, P. A. F. Martins, and N. Bay, “Revisiting the fundamentals of single point incremental forming by means of membrane analysis,” *Int. J. Mach. Tools Manuf.*, vol. 48, no. 1, pp. 73–83, 2008.

[46] M. B. Silva and P. A. F. Martins, “Two-point incremental forming with partial die: Theory and experimentation,” *J. Mater. Eng. Perform.*, vol. 22, no. 4, pp. 1018–1027, Apr. 2013.

[47] R. Malhotra, J. Cao, F. Ren, V. Kiridena, Z. Cedric Xia, and N. V. Reddy, “Improvement of Geometric Accuracy in Incremental Forming by Using a Squeezing Toolpath Strategy With Two Forming Tools,” *J. Manuf. Sci. Eng.*, vol. 133, no. 6, p. 061019, 2011.

[48] J. Shin *et al.*, “Prediction of Negative Bulge in Two Point Incremental Forming of an Asymmetric Shape Part,” in *Journal of Physics: Conference Series*, 2018, vol. 1063, no. 1.

[49] M. Nath, J. Shin, A. Bansal, M. Banu, and A. Taub, “Comparison of texture and surface finish evolution during single point incremental forming and formability testing of AA 7075,” in *Minerals, Metals and Materials Series*, vol. Part F4, Springer, Cham, 2018, pp. 225–232.

[50] R. Esmaeilpour *et al.*, “Experimental validation of the simulation of single-point incremental forming of AA7075 sheet with Yld2004-18P yield function calibrated with crystal plasticity model,” *Int. J. Adv. Manuf. Technol.*, pp. 1–17, Feb. 2021.

[51] L. Peng, X. Lai, H. J. Lee, J. H. Song, and J. Ni, “Analysis of micro/mesoscale sheet forming process with uniform size dependent material constitutive model,” *Mater. Sci. Eng. A*, vol. 526, no. 1–2, pp. 93–99, 2009.

[52] H. Wielage, Z. Hu, and F. Vollertsen, “Fracture behavior of thin foils,” *J. Mater. Process. Technol.*, vol. 212, no. 3, pp. 685–688, Mar. 2012.

[53] L. F. Peng, Z. T. Xu, M. W. Fu, and X. M. Lai, “Forming limit of sheet metals in meso-scale plastic forming by using different failure criteria,” *Int. J. Mech. Sci.*, vol. 120, pp. 190–203, Jan. 2017.

[54] A. K. Behera, R. A. de Sousa, G. Ingarao, and V. Oleksik, “Single point incremental forming: An assessment of the progress and technology trends from 2005 to 2015,” *J. Manuf. Process.*, vol. 27, pp. 37–62, Jun. 2017.

[55] S. He *et al.*, “Finite Element Modeling of Incremental Forming of Aluminum Sheets,” *Adv. Mater. Res.*, vol. 6–8, pp. 525–532, 2005.

[56] Y. Li, W. J. T. Daniel, and P. A. Meehan, “Deformation analysis in single-point incremental forming through finite element simulation,” *Int. J. Adv. Manuf. Technol.*, vol. 88, no. 1–4, pp. 255–267, 2017.

[57] M. Bambach, “Performance Assessment of Element Formulations and Constitutive Laws for the Simulation of Incremental Sheet Forming (ISF),” 2005.

[58] R. Esmaeilpour *et al.*, “Calibration of Barlat Yld2004-18P yield function using CPFEM and 3D RVE for the simulation of single point incremental forming (SPIF) of 7075-O aluminum

sheet," *Int. J. Mech. Sci.*, vol. 145, pp. 24–41, 2018.

[59] N. Moser, D. Leem, K. Ehmann, and J. Cao, "A high-fidelity simulation of double-sided incremental forming : Improving the accuracy by incorporating the effects of machine compliance," *J. Mater. Process. Tech.*, vol. 295, no. November 2020, p. 117152, 2021.

[60] I. Hayashi, M. Sato, and M. Kuroda, "Strain hardening in bent copper foils," *J. Mech. Phys. Solids*, vol. 59, no. 9, pp. 1731–1751, Sep. 2011.

[61] H. Kim, T. Park, R. Esmaeilpour, and F. Pourboghrat, "Numerical Study of Incremental Sheet Forming Processes," *J. Phys. Conf. Ser.*, vol. 1063, no. 1, 2018.

[62] "Quasi-Static Analyses Lecture 5," 2005.

[63] C. Henrard *et al.*, "Comparison of FEM Simulations for the Incremental Forming Process," *Adv. Mater. Res.*, vol. 6–8, pp. 533–542, 2005.

[64] P. Eyckens *et al.*, "Strain evolution in the single point incremental forming process: digital image correlation measurement and finite element prediction," *Int. J. Mater. Form. 2010 41*, vol. 4, no. 1, pp. 55–71, Aug. 2010.